Effects of near-surface thawing on elastic properties and signatures of seismic surface waves

Thesis for the degree
Master of Science in Geophysics

Julie Svendsmark

Department of Earth Science
University of Bergen

September, 2023

Abstract

The ongoing temperature rise in the Arctic may have severe effects on large areas of today's permanently frozen ground. Therefore, it is important to establish robust systems that can monitor permafrost changes with time. Surface wave methods are useful for mapping seismic structures in permafrost because they do not require abrupt velocity contrasts or normal velocity gradients (i.e., increasing velocity with depth). Rock physics models can be used to calculate how the stiffness and density of permafrost change with the degree of freezing, and they can be helpful when interpreting real seismic data from repeated acquisitions. I have tested several rock physics models and parameters of layered subsurface models to investigate their effects on elastic properties and surface wave propagation in permafrost. Changes in the dispersion characteristic of Rayleigh waves can be seen in the frequency-velocity spectra of the waves and depend on the distribution of the layer velocities and thicknesses. The seismic velocities depend on the ice saturation and the geometrical ice distribution in the pore space. However, other factors such as pore saturation, porosity, and sand properties also affect the seismic velocities and must be considered in analyses.

Acknowledgements

This thesis is a part of my master's degree in Geophysics at the Department of Earth Science, University of Bergen, and was only possible due to many contributors.

Firstly, I would like to thank my supervisor, Professor Tor Arne Johansen, for his help and guidance throughout this thesis. I would also like to give a big thanks to my co-supervisor, post-doctor Helene Meling Stemland, for her guidance and feedback and for always being available to answer my questions. Further, I would like to thank my co-supervisor, senior engineer Bent Ole Ruud, for giving me access to OASES and Geogiga software and for helping me with the use of these programs.

A big thanks to all my fellow students I had throughout my study who made student life a good experience. With that, I would like to give a special thanks to Elise, Fabian, and Ary, with whom I have spent much study time and spare time together. You have motivated me to start and complete my master's degree.

Finally, I would like to thank my friends and family, who always support me through thick and thin.

Contents

List of Figures

List of Tables

Chapter 1

Introduction

1.1 Motivation

The increasing temperature in the Arctic may cause extensive thawing of today's permanently frozen ground. Permafrost is a subsurface phenomenon that defines ground that stays at or below 0°C for at least two consecutive years (Dobinski, 2011). Today, it covers about a quarter of the land surface in the Northern Hemisphere, as shown in Figure 1.1. However, permafrost areas are expected to degrade in the future (e.g., Smith et al., 2022).

Permafrost thawing has several consequences. Frozen ground that thaws loses its mechanical strength and becomes unstable, and water may be released into the ground. That especially affects permafrost in mountain areas because slope instability causes hazards like landslides in steep slopes and mountain sides (e.g., Haeberli, 1997; Isaksen, 2018; Lindner et al., 2021). Destabilizing of the ground also affects level ground and may lead to subsidence and cause thermokarst, which is a terrain with very irregular surface (Nelson et al., 2001). In addition to the geomorphic consequences, permafrost stores large amounts of climate gases like carbon dioxide and methane, which may be released into the atmosphere and potentially accelerate climate changes (Schuur et al., 2015; Koven et al., 2015). The cost and methods used for infrastructure development are also highly affected because of unstable ground, which appears due to thawing (Melnikov et al., 2022). Climatic warming caused by increased climate gases in the atmosphere is predicted to be more significant in the Arctic than elsewhere (Zhang et al., 1997; Overland et al., 2014). How much impact thawing of the Arctic ground has on global warming is currently uncer-

tain and leads to the importance of establishing robust systems that can map and monitor permafrost changes with time.

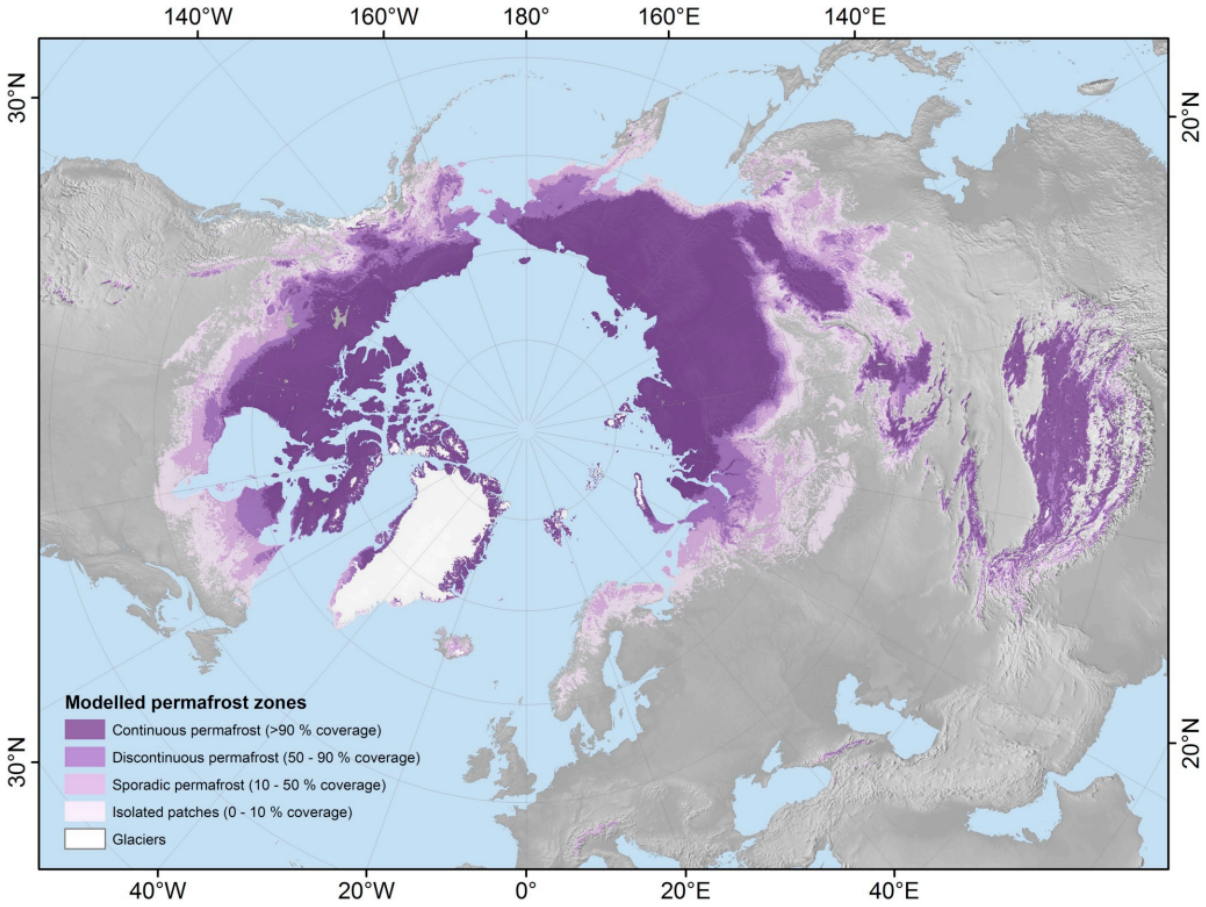

Figure 1.1: Map of modeled permafrost zones on the Northern Hemisphere based on temperature models for the 2000 – 2016 period (Obu et al., 2019).

Permafrost occurs when the extent of ground freezing during winter exceeds the ground thawing during summer (Dobinski, 2011). The surface layer thaws seasonally and is called an active layer (see Figure 1.2 for illustration). The active layer typically has a thickness of a few centimeters to several meters, which depends mainly on the length of the thaw season and the summer air temperature (Zhang et al., 1997; Isaksen, 2014). Studies on permafrost in Alaska show a trend of thinner active layers along the coast where the thaw season is short and cool compared to the inland (Zhang et al., 1997). However, the active layer's thickness is changing due to warmer temperatures. Several borehole measurements distributed in the Nordic area, from 1980 to 2010, show a general trend of a thicker active layer in the latest decades (Christiansen et al., 2010). Permafrost thickness varies from less than one meter in the southern sporadic zone to about 1500 m in parts of Siberia

(Isaksen, 2014). Typically, the thickness is between 100 – 800 m in the continuous zones, 25 – 100 m in the discontinuous zones, and 10 – 50 m in the sporadic zones (Anisimov and Reneva, 2006).

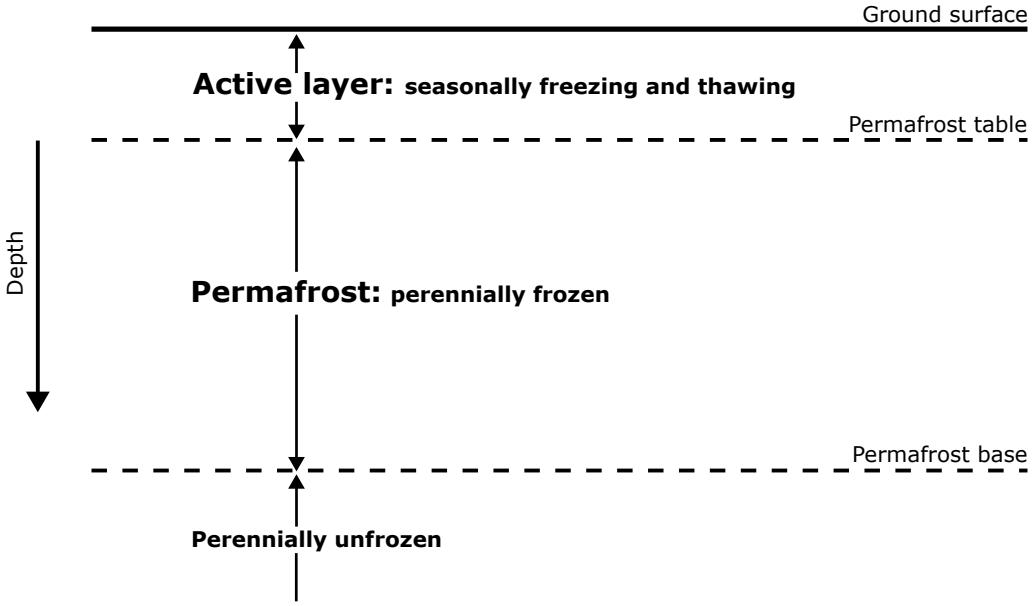

Figure 1.2: Schematic illustration of permafrost. The upper meters of permafrost, which thaw and refreeze seasonally, define the active layer. Below the active layer, it is perennially frozen ground.

Usually, near-surface structures are mainly controlled by lithology, which results in increasing seismic velocity with depth. In permafrost, the structure (including its ice and water content) may as well be controlled by thermal, chemical, and hydrological conditions (Dou and Ajo-Franklin, 2014). Temperatures of near-surface permafrost are susceptible to climate changes since they depend on air temperatures, precipitation, and snow depth (Isaksen et al., 2007). The temperature of a rock does not always represent a linear relation to ice saturation, which defines the percentage of ice in the rock's pore space. The freezing temperature largely depends on the salinity of the rock and the pore fluid (Dou et al., 2016). Nonsaline permafrost is generally stable unless its temperature approaches 0°C. However, saline permafrost is more temperature sensitive and very responsive to temperature changes well below 0°C (Dou et al., 2017). Permafrost can therefore contain water that is frozen, unfrozen, and partly frozen (Dobinski, 2011). Variations in salinity with depth may cause irregular ice and water distribution in the subsurface. Examples of unfrozen permafrost are the seabeds of the continental shelf of the Arctic Sea in northern Alaska and Siberia because of the salinity of the seawater (Dobinski, 2011). Saline

permafrost can also be found in uplifted ground previously located under the marine limit, such as the Adventdalen valley on Svalbard (Stemland et al., 2020a). Under thick glaciers, unfrozen permafrost can exist due to the overlaying pressure of the ice. The pressure prevents water from freezing. Partly frozen permafrost can also exist due to surface effects from fine-grained materials, such as clay, where only small amounts of water freeze at 0°C (Dobinski, 2011; Dou et al., 2016). This latter phenomenon will not be further investigated in this thesis.

Further, seismic waves are very sensitive to the stiffness of sediments. Thus, as frozen sediments thaw, their seismic properties change significantly. If seismic properties of near-surface sediments can be monitored over time, that may be used to predict the heat flux into the terrestrial Arctic (Stemland et al., 2020b).

Boreholes have been established in several places in the Arctic, and they are beneficial for the investigation of permafrost (e.g., Isaksen et al., 2007; Christiansen et al., 2010), but it is difficult to extract information about lateral variations from them (Stemland and Johansen, 2021). Geophysical techniques may be used to overcome this issue. These techniques indirectly enable detection, monitoring, and visualization of subsurface permafrost, where the obtained information may relate to shallow conditions such as the active layer (Hauck, 2013).

Ordinary refraction methods do not detect low-velocity layers below higher-velocity layers. That makes this method unsuitable for permafrost, where the distribution of frozen and unfrozen layers may cause irregular velocity gradients with depth. Electric methods can distinguish between frozen and unfrozen layers, but they are complicated to use in partly frozen sediments with highly conductive salt in their pore space (Wu et al., 2017).

However, surface waves are useful for mapping seismic structures in permafrost because the surface wave methods do not require abrupt velocity contrast or normal velocity gradients (Dou and Ajo-Franklin, 2014). Several surface wave analysis methods have been developed for mapping near-surfaces and may potentially be used on permafrost (e.g., Park et al., 2007; Tsuji et al., 2012; Dou and Ajo-Franklin, 2014; Foti et al., 2018)). While surface waves may be used to map and monitor the upper part of the permafrost, well-established reflection seismic can be used to find the thickness of the permafrost and variations in the deeper parts and to see lateral transitions from unfrozen to frozen ground as modeled in Johansen et al. (2003).

For mapping and monitoring permafrost, it is important to look into the effective rock properties of the sediments. The effective rock properties determine the seismic velocities, which can be linked to geophysical observations with rock physics modeling. Several rock physics models have been developed to describe the effective elastic properties of a rock (e.g., Zimmerman and King, 1986; Dvorkin et al., 1999; Johansen et al., 2003; Dou et al., 2017; Stemland et al., 2020b). Although most rock physics models were originally developed to describe the properties of deeper reservoir rocks, some of these models can also be used to analyze how a warmer climate may impact the seismic properties and the stability of permafrost. They may be helpful when interpreting real seismic data from repeated acquisitions to estimate the degree of freezing.

1.2 Objective

The objective of this master thesis is to study the effect of temperature variations on the elastic properties and seismic surface wave propagation in permafrost. To achieve this, I perform both rock physics modeling and seismic modeling. When the temperature changes, the ice saturation in the pore volume in unconsolidated sediments varies, and the sediments' stiffness and rigidity are largely affected. The rock physics modeling aims to investigate how variations in ice saturation impact sediments' stiffness and rigidity, assuming two different models for ice formation in the pore space. The seismic modeling aims to investigate how frozen, partly frozen, and unfrozen layers in the subsurface affect the dispersion of surface waves, which can be detected with surface wave analysis.

1.3 Outline

To study the objective of this thesis, I first make several models of possible freezing and thawing processes of sand saturated by a mixture of water and ice. Thereafter, based on these models, I use rock physics methods to compute elastic moduli and seismic velocities of frozen and unfrozen sand. Parameters such as porosity and sand properties may affect the velocity, and various parameter values are therefore tested in combination with ice saturation to study their effects.

Further, I do seismic modeling for several synthetic subsurface models. These subsurface models represent a near-surface consisting of frozen, partly frozen, and unfrozen layers. The thickness and velocity of the layers vary, as well as the number of layers. The velocities I use in the subsurface models are based on rock physics modeling. Finally, dispersion images are computed from the seismic gathers to study the dispersion characteristics for the various subsurface scenarios.

This master thesis is structured in seven chapters. The first chapter, **Chapter 1**, introduces the topic and objective of this thesis. **Chapter 2** and **Chapter 3** provide the theoretical background. They give a basic understanding of seismic waves and rock physics and describe the connection between the physical rock properties and the elastic properties. **Chapter 4** describes the generation of synthetic velocity models based on rock physics modeling, including how seismic modeling is used in surface wave analysis. **Chapter 5** presents the results of rock physics and seismic modeling, while **Chapter 6** discusses the results concerning the theory and the objective of this thesis. Suggestions for further investigations are also provided. Finally, **Chapter 7** summarizes the main conclusions of this thesis.

Chapter 2

Background - seismic waves

Seismic waves propagate through the Earth away from seismic sources. Their motions can be detected by receivers along the Earth's surface and contain information about the underlying subsurface. Several types of seismic waves exist. However, some elementary concepts need to be considered to understand how they propagate in unfrozen and frozen ground and are introduced in this chapter.

2.1 Characterization of elastic media

When seismic waves propagate through the Earth, the subsurface deforms elastically. Elasticity refers to strain, also denoted as deformation, that vanishes entirely upon removal of stresses that cause deformations (Barber, 2002). Thus, stress and strain are essential quantities within elasticity theory.

Stress, σ, is defined as force, F, per unit area, A, i.e., $\sigma = \frac{F}{A}$, and is a measure of the capacity of a material to carry loads (Reddy, 2013). The units for stress are Pascal (Pa) or Newton per square meter (N/m^2). When a material is subjected to stress, its shape and/or size will deform. The mechanical effects of the deformation are confined to the stretch, characterized by a dimensionless strain measure (Kennett and Bunge, 2008). Strain, ϵ, relates the change in length, Δl, of the material to its initial length, l, i.e., $\epsilon = \frac{\Delta l}{l}$.

Within elasticity theory, deformations are assumed to be both reversible and proportional to stress. Hooke's law expresses the relationship between stress and strain in a relatively simple equation,

$$M = \frac{\sigma}{\epsilon}, \tag{2.1}$$

where M is an elastic modulus measured in Pascal (Guéguen and Palciauskas, 1994).

A typical stress-strain curve for a solid material is shown in Figure 2.1. Hooke's law is valid for small deformations with a linear relationship between stress and strain. In the linear domain, the material behaves elastically. Beyond the yield point, the material is inelastic, and the deformations are ductile and irreversible. Fracturing happens when further stress is applied. In most near-surface studies, inelasticity can safely be neglected (Everett, 2013).

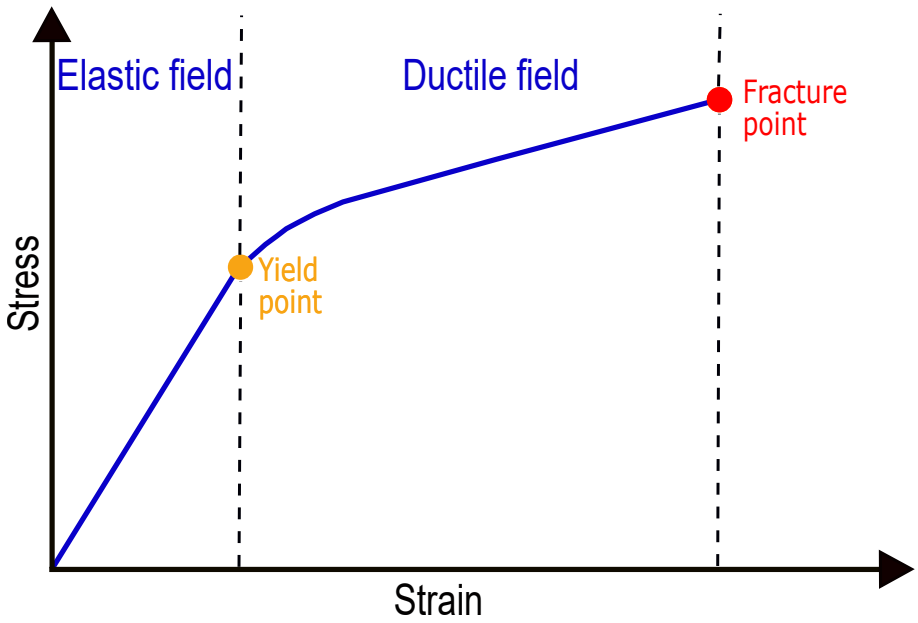

Figure 2.1: Stress-strain relation. The yield point defines a material's transition from elastic to ductile behavior. When further stress is applied to the medium, it fractures. Modified from Kearey et al. (2002).

A material is characterized by its elastic moduli, and each elastic modulus expresses the ratio of a specific type of stress to the resultant strain (Kearey et al., 2002).

When a rod is stretched, **Young's modulus**, E, expresses the ratio of the longitudinal stress to the longitudinal strain (Kearey et al., 2002). Young's modulus measures the

material's resistance to change its length when it is under lengthwise tension or compression. The higher the modulus, the more resistant the material. The equation for Young's modulus is

$$E = \frac{\frac{F}{A}}{\frac{\Delta l}{l}}, \tag{2.2}$$

where F is the force, A is the initial cross-sectional area, l is the initial length, and Δl is the change in length. An illustration of the parameters is given in Figure 2.2.

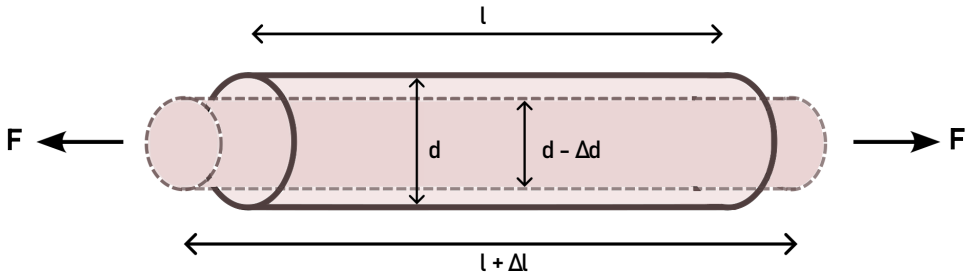

Figure 2.2: Elongated rod illustrates the parameters of Young's modulus and Poisson's ratio.

When the rod is stretched, the elongated rod's width reduces. The change in width makes a transverse strain equal to the change in width divided by the original width. **Poisson's ratio**, ν, is a dimensionless measure of the transverse strain divided by the longitudinal strain (Everett, 2013), and can be expressed as

$$\nu = \frac{\frac{\Delta d}{d}}{\frac{\Delta l}{l}}, \tag{2.3}$$

where d is the original diameter and Δd is the change in diameter. Typical values of the Poisson's ratio are between 0 and 0.5, where 0.5 represents a liquid. Poisson's ratio of 0.25 is a common assumption for the Earth's upper continental crust (Zandt and Ammon, 1995). Values less than 0 are seldom, if ever, observed (Mavko et al., 2009).

Bulk modulus, K, measures a material's resistance to being compressed (Kearey et al., 2002). It defines the ratio of the volumetric stress, P, to the volumetric strain, $\frac{\Delta V}{V}$. The

equation for bulk modulus can be expressed as

$$K = \frac{P}{\frac{\Delta V}{V}}, \tag{2.4}$$

and the parameters are illustrated in Figure 2.3 (a).

Shear modulus, μ, measures a material's resistance to shear deformation. Liquids and gases cannot resist shear deformation and have thus zero shear moduli. Shear modulus expresses the ratio of the shear stress, τ, to the shear strain, $tan\theta$, within a medium (Kearey et al., 2002). The equation is given by

$$\mu = \frac{\tau}{tan\theta}, \tag{2.5}$$

and the parameters are illustrated in Figure 2.3 (b).

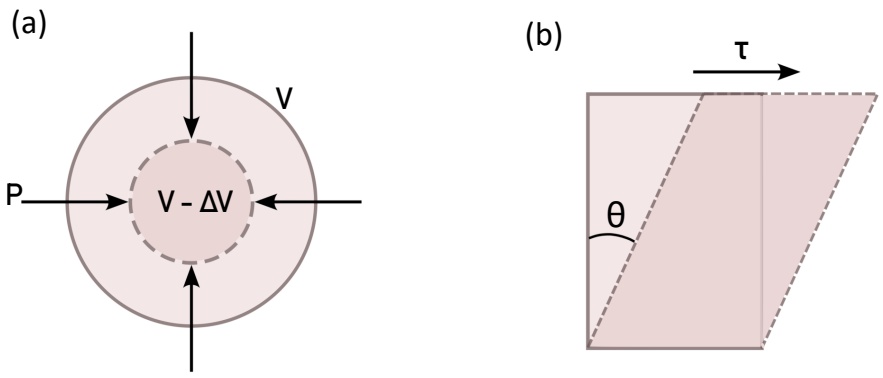

Figure 2.3: (a) Compressed sphere illustrating the parameters of bulk modulus. (b) Shear-deformed box illustrating the parameters of shear modulus.

Within seismic, bulk and shear moduli of a rock are often used together with the density of the rock to characterize the material the waves travel through. P- and S-wave velocities are essential velocities that may be derived from the elastic moduli and are explained in the following section.

2.2 Various types of seismic waves

Seismic waves can be divided into body waves and surface waves. Body waves propagate through the internal volume of an elastic solid, and they are further divided into compressional waves and shear waves. The compressional waves, also known as P-waves, propagate in the direction of the particle motion. They travel through all types of material with a particle motion consisting of alternating compression and dilation (Kearey et al., 2002).

Shear waves, also called S-waves, propagate in the direction perpendicular to the particle motion, where the particle motion consists of transverse motions (Kearey et al., 2002). S-waves travel through solids but not through liquids or gases, which have zero shear moduli. If all the particle oscillations are confined to a plane, the S-waves are plane-polarized (Kearey et al., 2002). S-waves may be horizontally polarized with motions in a horizontal plane (SH-waves) or vertically polarized with motions in a vertical plane (SV-waves).

The elastic moduli of the layers, which the wave excites, determine the seismic wave velocities (Everett, 2013). The P- and S-wave velocities, V_P and V_S, in a homogeneous isotropic elastic medium are given by

$$V_P = \sqrt{\frac{K + \frac{4}{3}\mu}{\rho}}, \tag{2.6}$$

$$V_S = \sqrt{\frac{\mu}{\rho}}, \tag{2.7}$$

where ρ is the density of the medium measured in kg/m^3 (Kearey et al., 2002). Studies by Johansen et al. (2003) indicate that the P- and S-wave velocities increase with 80 – 90% when fully, or almost fully, water saturated unconsolidated sediments freeze.

Surface waves travel along a "free" surface, such as the earth-air or the earth-water interface. They travel slower, have longer wavelengths, and have a wider frequency range than body waves. Their amplitudes of particle motion, which are larger than for body waves, generally decrease with depth (Krebes, 2019). Surface waves may be divided into several types, two of which are Rayleigh waves and Love waves. They can occur along the earth-air interface.

Rayleigh waves are the most fundamental of the surface waves resulting from interfering P- and SV-waves (Mi et al., 2018). These waves have an elliptical particle motion in a vertical plane with respect to the surface. The Rayleigh wave velocity is typically 0.88-0.95 times the S-wave velocity, depending on the Poisson's ratio (Mi et al., 2018). The Rayleigh wave equation can be expressed as

$$\left(2 - \frac{V_R^2}{V_S^2}\right)^2 - 4\left(1 - \frac{V_R^2}{V_P^2}\right)^{\frac{1}{2}}\left(1 - \frac{V_R^2}{V_S^2}\right)^{\frac{1}{2}} = 0,$$

where V_R is the Rayleigh wave velocity, and the equation is valid when the medium it travels along is an isotropic homogeneous elastic solid (Nkemzi, 1997).

Love waves are generated from constructive interference of multiple reflections of SH-waves at the free surface. They only occur at the surface when the S-wave velocity increases with depth, and they cannot exist in a homogeneous half-space (Mi et al., 2018). These waves have a particle motion perpendicular to the wave propagation but parallel to the surface (Kearey et al., 2002).

Surface waves are generated in all seismic surveys, and they are often considered noise in seismic profiles (Park et al., 2007). This thesis emphasizes their advantages and discusses how to use them for mapping near-surface.

2.3 Seismic wave propagation

A seismic pulse propagates outwards from a seismic source. In a homogeneous medium, the pulse travels at constant velocity in all directions, and the wavefront, representing a constant travel time curve, is a sphere. A ray represents the direction of the energy. In an isotropic medium, where the physical properties are the same regardless of direction, seismic rays are perpendicular to a given wavefront (Kearey et al., 2002). That is illustrated in Figure 2.4.

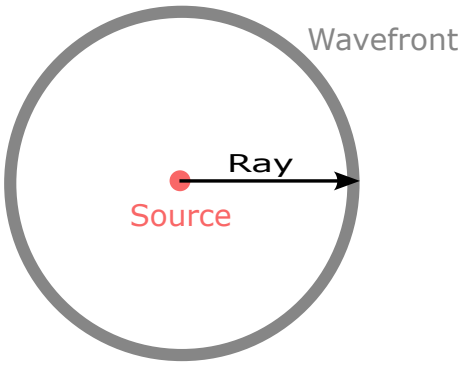

Figure 2.4: Representation of the relationship between rays and wavefront in an isotropic medium.

The propagation velocity and direction of the waves change at geological boundaries within the subsurface depending on the physical properties of the layers in the earth. At such interfaces, the energy within an incident seismic pulse is partitioned into transmitted and reflected pulses of P- and S-waves. Figure 2.5 illustrates an energy partitioning of an incident P-wave.

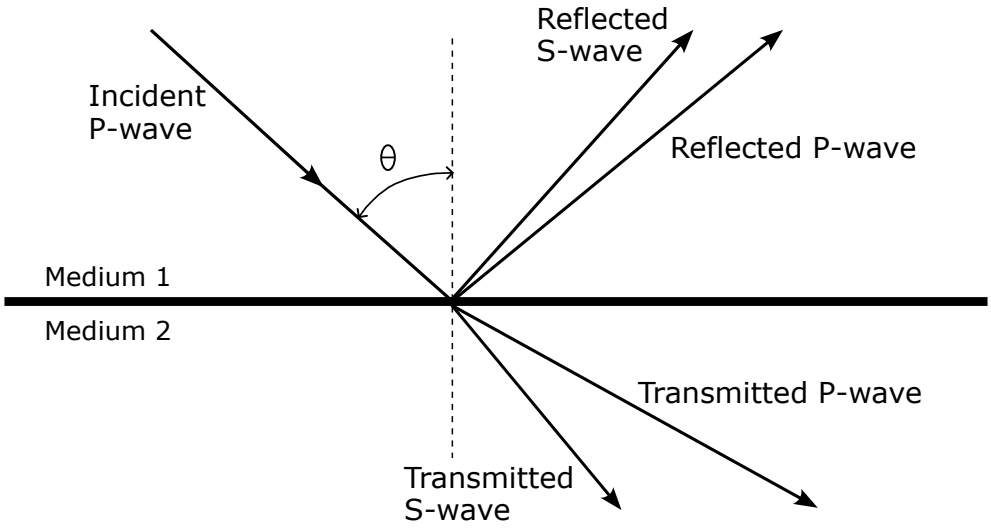

Figure 2.5: Reflected and transmitted P- and S-wave rays generated by an incident P-wave on an interface. Medium 2 has higher seismic velocity than medium 1.

The distribution of the reflected and transmitted energy depends on the contrast of acoustic impedance of the medium above and below the interface. Acoustic impedance, often denoted as Z, is the product of velocity, V, and density, ρ, i.e., $Z = V\rho$. At normal

incidence, the reflection and transmission coefficients, R and T, are given as

$$R = \frac{Z_2 - Z_1}{Z_2 + Z_1}, \tag{2.8}$$

$$T = 1 - R, \tag{2.9}$$

where subscripts 1 and 2 represent the medium above and below the interface, respectively (Castagna and Backus, 1993). For incident waves that are not normal to the interface, the more complex Zoeppritz equations are developed to compute the reflection and transmission coefficients (Castagna and Backus, 1993).

However, the angles for the reflected and transmitted rays can, in any case, be calculated from Snell's law,

$$p = \frac{sin\theta_1}{V_1} = \frac{sin\theta_2}{V_2}, \tag{2.10}$$

where p defines the ray parameter, which remains constant along one ray (Kearey et al., 2002). θ is the angle, and V is the velocity.

When the velocity of the underlying layer is higher than the layer above, it is a particular angle of incidence, critical angle θ_c, that provides a refracted wave ray that travels along the interface at the higher velocity (Kearey et al., 2002). The motions of waves that return to the surface after refraction or reflection at geological boundaries may be detected as traveltimes and amplitudes by receivers along the surface. These traveltimes can be converted into depth values to get an image of the ground. In permafrost, the underlying layer sometimes has a lower velocity than the layer above, and the seismic methods using refracted waves are therefore not the best in such areas.

2.4 Frequency-dependent waves

If the medium is heterogeneous, with spatially varying elastic moduli, the Rayleigh wave packet is dispersive (Everett, 2013). That means that the packet can be decomposed into its individual frequency components, and each frequency component travels at its own characteristic phase velocity, which is different from the group velocity. The phase velocities are the velocities of any given wave phase, and the group velocity is the velocity

of the entire wave packet envelope (Krebes, 2019). The group velocity is typically slower than the phase velocity, and both velocities are illustrated in Figure 2.6.

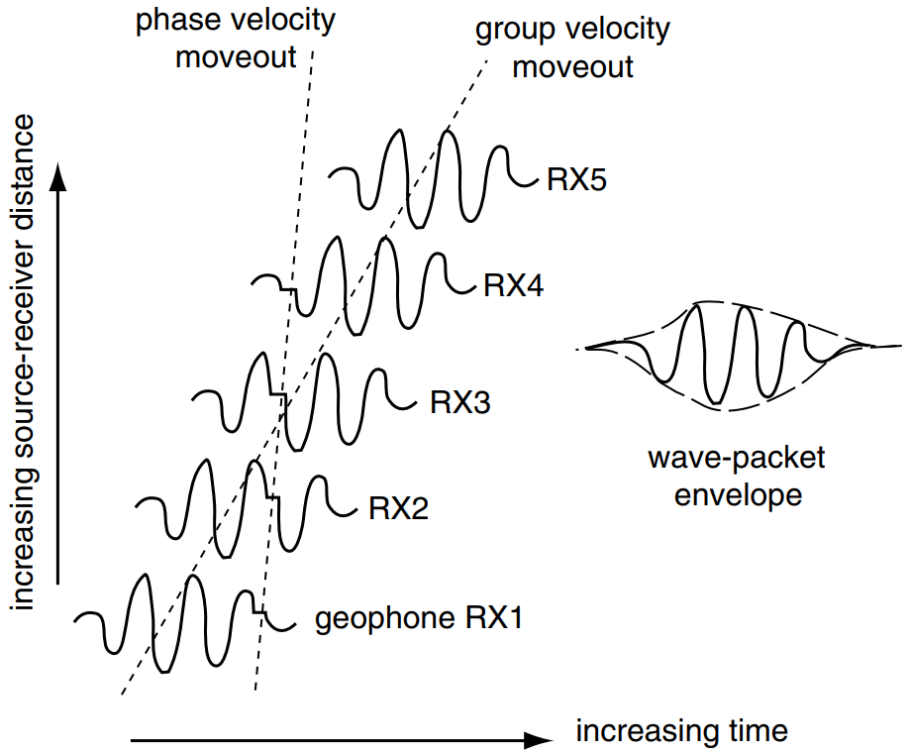

Figure 2.6: Comparison of phase and group velocities within a dispersive wave packet (Everett, 2013).

If there is no dispersion, the group velocity equals the phase velocity, and the pulse shape stays the same. Rayleigh waves traveling in a homogeneous elastic medium are not dispersive (Everett, 2013).

When dispersion occurs, the shape of the pulse changes as it propagates (Everett, 2013). The shape of the phase velocity versus frequency curve can be called the dispersion characteristic and is described further in Chapter 4.2.3. Both Rayleigh waves and Love waves can be dispersive (Mi et al., 2018). Their propagation depth depends on their wavelength. Waves with short wavelengths (high frequencies) propagate in top layers, and the upper layers' properties influence the velocities (Socco and Strobbia, 2004). Waves with long wavelengths (low frequencies) propagate deeper than the high frequencies, and their velocities therefore depend on the properties of more layers. The dispersion associated with the geometric distribution of the sediment properties is called geometrical dispersion (Socco and Strobbia, 2004).

Rayleigh waves are not inherently dispersive. Thus, any observed dispersion has to be generated because of variation in the elastic properties of the layers (Stemland et al., 2020a). Some seismic methods try to utilize these dispersion properties of the waves when mapping the shallow subsurface (e.g., Park et al., 2007; Foti et al., 2018), while Stemland et al. (2020a) has investigated the use of the methods in the near-surface Arctic. The seismic velocity gradient is often irregular in permafrost, and therefore seismic data from these areas show highly dispersive surface waves (Dou and Ajo-Franklin, 2014; Stemland, 2020).

2.5 Seismic waves in frozen and unfrozen sediments

The freezing and thawing of permafrost result in varying ice saturation distribution in the active layer. Ice has higher bulk and shear moduli than water, meaning ice is stiffer and more rigid. The stiffer the material, the higher the seismic wave velocity. Consequently, as a medium freezes, the seismic wave velocities increase. Several rock physics models are used to model the velocity changes as a function of ice saturation, and these are discussed in Chapter 3.

Figure 2.7 shows an example from Stemland et al. (2020a) of real seismic data acquired in Adventdalen, Svalbard. In this area, the active layer is approximately 1.2 m, and the permafrost thickness is about 100 m. Seismic acquisition was performed in October 2013, January 2014, and August 2014 at the same location. Seismic gathers and dispersion images are shown for all three cases. The ice saturation in the ground was presumed to be highest in January and lowest in August, and it is assumed to be most laterally heterogeneous in October. The figure shows clearly that freezing and thawing affect real seismic data since it is possible to see changes in the seismic gathers and the dispersion images. The data from January show significant differences from the two other months. Frozen, stiff near-surface sediments in January result in strong amplitude events at increasing phase velocities with increasing frequency. These amplitude events may be signs of higher surface wave modes, as described in Chapter 4.2.3. Chapter 5.2 provides several synthetic examples of such phenomena.

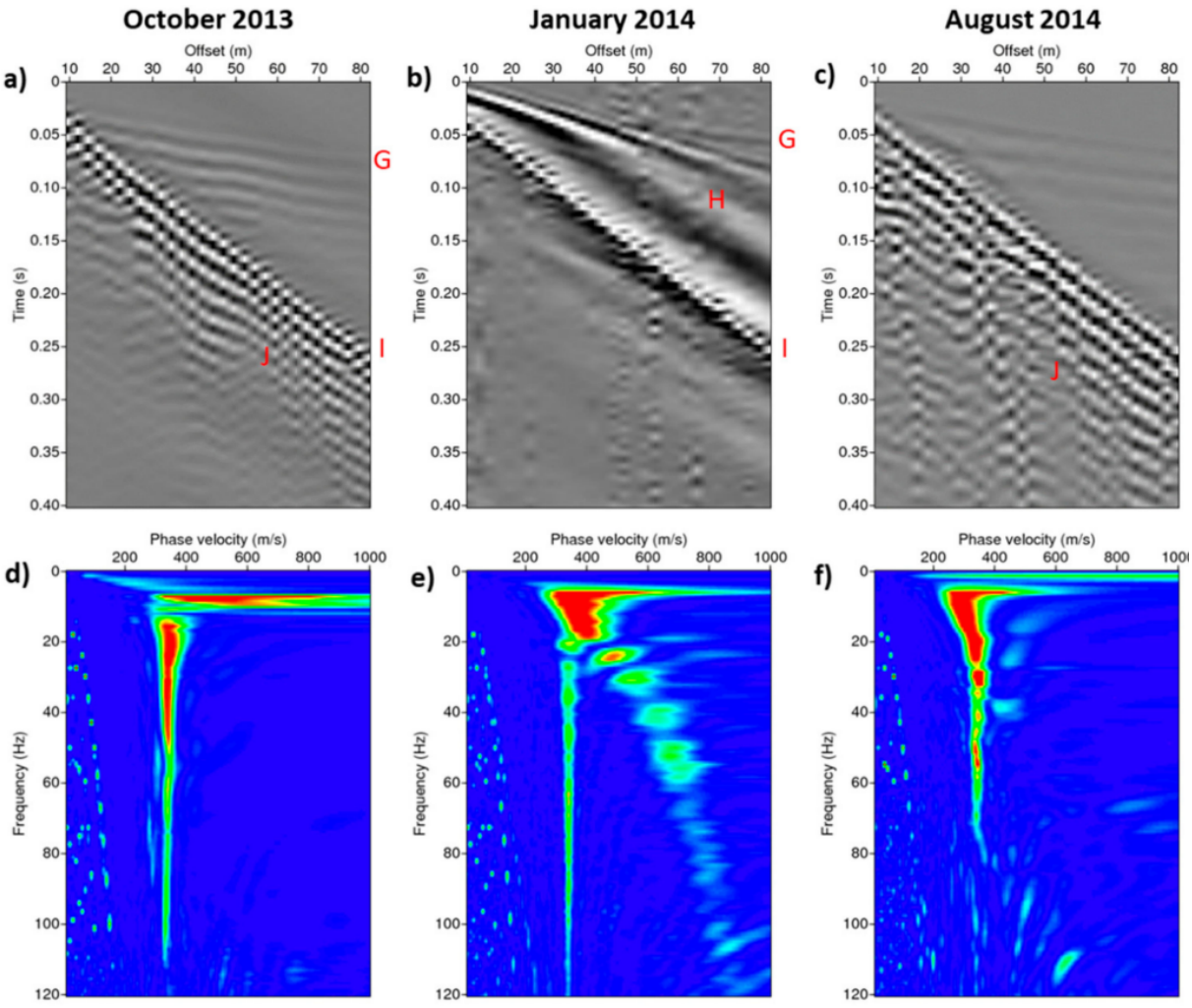

Figure 2.7: Seismic data acquired by Stemland et al. (2020a) in Adventdalen, Svalbard. Top row: seismic gathers for (a) October 2013, (b) January 2014, and (c) August 2014. Bottom row: corresponding dispersion images for (d) October 2013, (e) January 2014, and (f) August 2014. The capital letters G – J identify different wave modes described in Stemland et al. (2020a).

Chapter 3

Background - rock physics

Rock physics describes the relationship between geophysical observations and the underlying physical properties of rocks (Mavko et al., 2009). The geophysical observations, such as P- and S-wave velocities, are directly related to the effective elastic moduli as seen in Chapter 2.2. The elastic moduli of a rock are again affected by its physical properties, as will be shown in this chapter. Several rock physics models can be used to describe these relations, and the following sections describe the background and general use of the models.

3.1 Physical rock properties

Several physical rock properties are important parameters used in rock physics modeling, some of which are discussed in this section.

The **density**, ρ, of a rock defines its mass, M, divided by its volume, V, i.e., $\rho = \frac{M}{V}$. Considering a mixed material consisting of N constituents, the effective density can be estimated exactly with a weighted sum of the densities of all constituents,

$$\rho = \sum_{i=1}^{N} f_i \rho_i, \tag{3.1}$$

where f_i denote the volume fraction and ρ_i is the density of the ith constituent (Mavko et al., 2009).

Porosity defines the fraction of a rock volume that is not occupied by solid matter, and **permeability** indicates how easily fluids can flow through this pore space (Guéguen and Palciauskas, 1994). The porosity equals the pore volume divided by the total volume of the rock, and it gives no information concerning pore sizes, their distribution, and the degree of connectivity (Guéguen and Palciauskas, 1994). Therefore, two rocks may have different physical properties, such as varying permeability, even though they have identical porosities. Open porosity, ϕ_{open}, constitutes the connected pore space, while closed porosity, ϕ_{closed}, constitutes the isolated pore space. Only the open porosity, also called the effective porosity, impacts the rock's permeability. The sum of the various porosities makes the total porosity, $\phi = \phi_{open} + \phi_{closed}$. Effective porosity is an essential variable concerning seismic properties and density. Several rock physics models depend on the critical porosity, ϕ_0, which defines the maximum porosity possible when the grains are still in contact.

The **coordination number** defines the average number of contacts per grain. The relationship between coordination number and porosity can be approximated by the empirical equation,

$$n = 20 - 34\phi + 14\phi^2, \tag{3.2}$$

where n is the coordination number (Avseth et al., 2005).

3.2 Effective elastic media: upper and lower bounds

Some properties must be considered to predict the effective elastic moduli of a mix of grains and pores. The volume fractions and the elastic moduli of the various materials should be specified in addition to the geometric details of the materials (Mavko et al., 2009). The upper and lower bounds are possible to predict when only having the volume fractions and the elastic moduli. The effective elastic moduli fall in between the bounds. Stiffer shapes will have higher values within the range, and softer shapes will have lower values. Several bounds can be used, some of which are discussed in this section.

3.2.1 Voigt and Reuss bounds

The Voigt and Reuss bounds are the simplest bounds to use on a mixture of several phases. This method presupposes that each constituent is isotropic, linear, and elastic (Mavko et al., 2009).

The equation for the Voigt upper bound, M_V, is given by

$$M_V = \sum_{i=1}^{N} f_i M_i, \tag{3.3}$$

where N defines the number of phases, f_i is the volume fraction and M_i is the elastic modulus for each phase i. The Voigt upper bound gives the ratio of the average stress to the average strain when all phases are assumed to have the same strain. Considering a medium of two isotropic phases distributed in parallel layers, the phases have the same strain when the stress is applied parallel to the layers (Figure 3.1 (a)).

The Reuss lower bound, M_R, is given by

$$\frac{1}{M_R} = \sum_{i=1}^{N} \frac{f_i}{M_i}, \tag{3.4}$$

and gives the ratio of the average stress to the average strain when all phases are assumed to have the same stress. That is the case when stress is applied perpendicular to the layers of the medium of two isotropic phases (Figure 3.1 (b)).

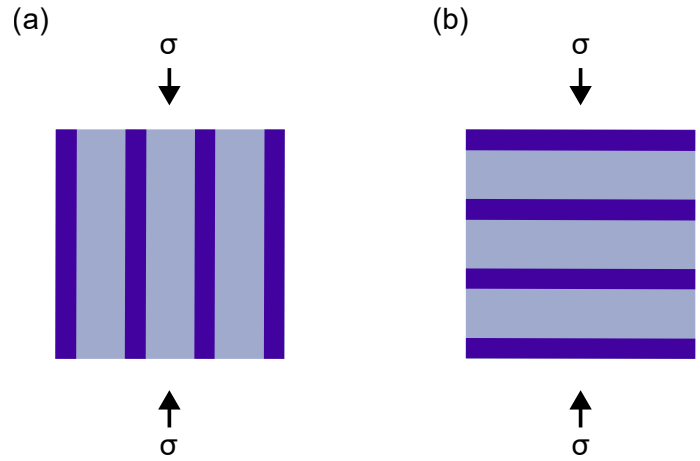

Figure 3.1: Physical interpretation of the Voigt-Reuss bounds for a two-phase material. (a) Stress is applied perpendicular to layers, and the two phases have the same strain (upper bound). (b) Stress is applied parallel to layers, and the two phases have the same stress (lower bound).

When an estimate of the elastic modulus is needed, the Voigt-Reuss-Hill (VRH) average can be useful (Mavko et al., 2009). The arithmetic average, M_{VRH}, also known as Hill average (Hill, 1963), gives an estimate of the modulus of Voigt upper bound and Reuss lower bound,

$$M_{VRH} = \frac{M_V + M_R}{2}. \tag{3.5}$$

3.2.2 Hashin-Shtrikman bounds

The Hashin-Shtrikman (HS) bounds (Hashin and Shtrikman, 1963) give the narrowest possible range without specifying anything about the geometries of the various phases. This method presupposes that each of the individual constituents and the whole rock is isotropic, linear, and elastic (Mavko et al., 2009).

The upper HS bound (HS+) is the stiffest combination of the mixture, and the lower HS bound (HS-) is the softest mixture. When the medium consists of two phases, the upper and lower bounds for the bulk and shear moduli, $K_{HS\pm}$ and $\mu_{HS\pm}$, are given by

$$K_{HS\pm} = K_1 + \frac{f_2}{(K_2 - K_1)^{-1} + f_1(K_1 + \frac{4}{3}\mu_1)^{-1}}, \tag{3.6}$$

$$\mu_{HS\pm} = \mu_1 + \frac{f_2}{(\mu_2 - \mu_1)^{-1} + 2f_1\left(\frac{K_1+2\mu_1}{5\mu_1(K_1+\frac{4}{3}\mu_1)}\right)}, \tag{3.7}$$

where f is the volume fraction of the individual phases (Mavko et al., 2009). When the softest material is subscripted 1, the equations yield the lower bounds, and when the stiffest material is subscripted 1, the equations yield the upper bound. These expressions assume that the material with the larger bulk modulus also has the larger shear modulus.

A generalized form of the HS bounds, called the Hashin-Shtrikman-Walpole (HSW) bounds, $K_{HSW\pm}$ and $\mu_{HSW\pm}$, can be written as

$$K_{HSW\pm} = K_1 + \frac{f_2}{(K_2 - K_1)^{-1} + f_1(K_1 + \frac{4}{3}\mu_m)^{-1}}, \tag{3.8}$$

$$\mu_{HSW\pm} = \mu_1 + \frac{f_2}{(\mu_2 - \mu_1)^{-1} + f_1\left[\mu_1 + \frac{\mu_m}{6}\left(\frac{9K_m + 8\mu_m}{K_m + 2\mu_m}\right)\right]^{-1}}, \tag{3.9}$$

where K_m and μ_m represent the individual constituents' maximum bulk and shear moduli, respectively, when calculating the upper bounds (Mavko et al., 2009). When calculating the lower bounds, they represent the minimum bulk and shear moduli, respectively.

If one of the media in the mixture has zero shear modulus (i.e., it is a liquid or a gas), the Hashin-Shtrikman lower bound gives the same values as the Reuss lower bound (Mavko et al., 2009).

A schematic illustration of the HS bounds is shown in Figure 3.2. The illustration shows how one phase is surrounded by the other. The upper bound is realized when the stiffest material forms the shell, and the lower bound is realized when the stiffest material is in the core.

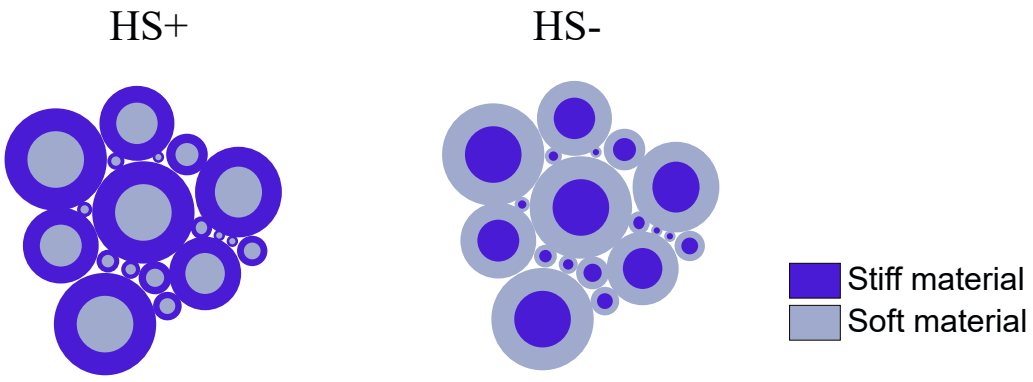

Figure 3.2: Physical interpretation of the Hashin-Shtrikman bounds for a two-phase material.

If a medium has properties between the upper and lower bounds, the arithmetic average

(Hill average) of the two HS bounds can be used to estimate the effective properties. The equations are

$$K_{HSH} = \frac{K_{HS+} + K_{HS-}}{2}, \tag{3.10}$$

$$\mu_{HSH} = \frac{\mu_{HS+} + \mu_{HS-}}{2}, \tag{3.11}$$

where K_{HSH} and μ_{HSH} are the Hashin-Shtrikman-Hill bulk and shear moduli, respectively.

In this thesis, I use the HS bounds as a two-end-member mixing approach with ice saturated rock as the stiff end-member and water saturated rock as the soft end-member, as in Dou et al. (2017) and Stemland et al. (2020b). The workflow of this method is represented in Chapter 4.1.1.

3.3 Effective elastic media: the impact of physical and structural rock properties

The upper and lower bounds of the effective elastic moduli are simple models. However, more complex models are often needed to understand the effect of structural variations and to give a more accurate estimate of the effective elastic properties. This chapter describes some of the more complex models that consider both the physical and structural properties of a rock.

3.3.1 Elastic properties in dry unconsolidated rocks

When considering a dry, random pack of identical spherical grains, the Hertz-Mindlin contact theory (CT) from Mindlin (1949) can be used to find the effective bulk and shear moduli, K_{CT} and μ_{CT}. "Dry rock" denotes a rock with only vacuum in its pore space. The equations are given by

$$K_{CT} = \left[\frac{n^2(1-\phi_0)^2\mu_G^2}{18\pi^2(1-\nu_G)^2}P\right]^{\frac{1}{3}}, \tag{3.12}$$

$$\mu_{CT} = \frac{5-4\nu_G}{5(2-\nu_G)}\left[\frac{3n^2(1-\phi_0)^2\mu_G^2}{2\pi^2(1-\nu_G)^2}P\right]^{\frac{1}{3}}, \tag{3.13}$$

where n is the coordination number, P is the effective pressure, and ν_G is the Poisson's ratio of the grain (Avseth et al., 2005). μ_G is the shear modulus of the grain, and ϕ_0 is the critical porosity.

The results of these equations are often referred to as the elastic properties of the solid frame of the rock, which are not consolidated. Hertz-Mindlin contact theory cannot be used if the rock is consolidated, but other inclusion models like self-consistent approximation may then be used.

3.3.2 Inclusion models

Several inclusion models are developed, and the self-consistent approximation (SCA) is one of them. The SCA is a method to estimate the effective properties of a composite material. As for the other upper and lower bounds, information about each phase's volume fraction and elastic moduli is needed. Besides that, specific inclusion shapes are assumed for the SCA (Mavko et al., 2009).

The SCA method assumes that the grains and the pore-filling medium are inclusions in another background medium with initially unknown elastic properties. In practice, the elastic properties of the background medium are adjusted iteratively until the net scattering from all inclusions, caused by an incident wave, vanishes. The general equations for the SCA are

$$\sum_{i=1}^{N} S_i(K_i - K_{SCA})P_i = 0, \tag{3.14}$$

$$\sum_{i=1}^{N} S_i(\mu_i - \mu_{SCA})Q_i = 0, \tag{3.15}$$

where S_i is the volume fraction of each inclusion type i, and K_{SCA} and μ_{SCA} are the medium's effective bulk and shear moduli, respectively (Berryman, 1995). P_i and Q_i are shape-dependent factors from Berryman (1995).

In the case of spherical inclusions, the equations for P_i and Q_i are

$$P_i = \frac{K_m + \frac{4}{3}\mu_m}{K_i + \frac{4}{3}\mu_m}, \tag{3.16}$$

$$Q_i = \frac{\mu_m + \zeta_m}{\mu_i + \zeta_m}, \tag{3.17}$$

where

$$\zeta = \frac{\mu}{6}\left(\frac{9K + 8\mu}{K + 2\mu}\right). \tag{3.18}$$

The subscripts m and i refer to the matrix and inclusion phases, respectively. When penny-shape inclusions are assumed, the equations for P_i and Q_i are

$$P_i = \frac{K_m + \frac{4}{3}\mu_i}{K_i + \frac{4}{3}\mu_i + \pi\alpha\beta_m}, \tag{3.19}$$

$$Q_i = \frac{1}{5}\left[1 + \frac{8\mu_m}{4\mu_i + \pi\alpha(\mu_m + 2\beta_m)} + 2\frac{K_i + \frac{2}{3}(\mu_i + \mu_m)}{K_i + \frac{4}{3}\mu_i + \pi\alpha\beta_m}\right], \tag{3.20}$$

where

$$\beta = \mu\left(\frac{3K + \mu}{3K + 4\mu}\right), \tag{3.21}$$

and α is the aspect ratio of the inclusions.

3.3.3 The effect of fluid

The effective properties of a dry rock change when a fluid saturates its pore space. One pore fluid may, in some cases, replace another fluid, referred to as fluid substitution. When a fluid fully saturates the pore space in a rock, Gassmann's equations (Gassmann, 1951) can be used to find the effective elastic moduli of the rock. The effective bulk modulus, K_{sat}, can be expressed as

$$K_{sat} = K_G\frac{\phi_0 K_{CT} - (1 + \phi_0)K_F K_{CT}/K_G + K_F}{(1 - \phi_0)K_F + \phi_0 K_G - K_F K_{CT}/K_G}, \tag{3.22}$$

where K_{CT} denotes the dry rock bulk modulus found by CT in Chapter 3.3.1. K_G is the bulk modulus of the grain, and K_F is the bulk modulus of the fluid. The effective shear

modulus of a saturated rock, μ_{sat}, is unaffected by the presence of a nonviscous fluid and can therefore be expressed as

$$\mu_{sat} = \mu_{CT}. \tag{3.23}$$

Gassmann's equations assume that the rock is homogeneous and isotropic (Smith et al., 2003). If there are several fluids in the pore space, Reuss lower bound may be used to estimate the effective fluid bulk modulus for a homogeneous mixture of these fluids. If the medium consists of several types of grains, the effective grain bulk modulus may be estimated using the Voigt-Reuss-Hill average, representing a patchy mixing of several grains. Gassmann's equations also assume that the pore space is fully fluid-saturated and completely connected (i.e., open porosity = effective porosity). The equations are only valid for frequencies lower than $\sim 10^4$ Hz (Mavko et al., 2009).

3.3.4 The effect of ice

When the pore water freezes, the rock consists of ice fragments in its pore space. Ice is a stiffer material than water, acting as a solid, with both bulk and shear moduli above zero. Therefore, it is not possible to use Gassmann's equations to find the effective properties of the ice saturated rock. This chapter discusses some freezing processes, including a method to calculate the effective elastic moduli of an ice saturated rock.

Freezing and thawing processes

If a rock is saturated by water and the temperature decreases, the water starts to freeze at a specific temperature. For pure water, the freezing point is 0°C, but saline water has a decreased freezing point depending on the salt-to-water ratio, salinity (Ming et al., 2020). The freezing point depression is limited by a critical temperature at approximately −21°C for brine, called the eutectic point (Dou et al., 2017). Below the eutectic point, all salts become solid crystals. The relation between temperature, salinity, and ice saturation can be calculated from equations in Potter et al. (1978).

Progressive salination of the residual pore water is another effect of the dissolved salt (Dou et al., 2017). The various freezing points of saline water and the progressive salination of

the residual cause gradual freezing of water with temperature. The residual pore water becomes more saline because salts are excluded from ice. That will further lower the freezing point and slow down the freezing process. Saline permafrost therefore usually consists of partially frozen slush (Dou et al., 2017).

A rock consisting of grains and pores fully saturated by water may start to freeze when the temperature decreases. Several models describe how water may freeze in the pore space, and some examples are illustrated in Figure 3.3. Water is assumed to freeze in a patchy way in the model used in Stemland et al. (2020b). Patchy freezing means that ice fragments are distributed spatially nonuniformly (Guéguen and Palciauskas, 1994). Another way of freezing can be that the water starts to freeze in the middle of the pore space, and the water closest to the grains freezes the last. The water in the pore space may also start to freeze homogeneously, which means it freezes everywhere in the pore space simultaneously. Another assumption can be that a water saturated rock starts to freeze at the contact points between the grains before the rest of the pore-filling water freezes, as it is assumed in the paper by Johansen et al. (2003), or it starts to freeze all around the grains.

Whichever freezing processes are assumed in a model impacts how the rock's effective properties change with ice saturation since the effective elastic properties depend on the geometrical distribution of the ice as well as the ice saturation (Dou et al., 2016).

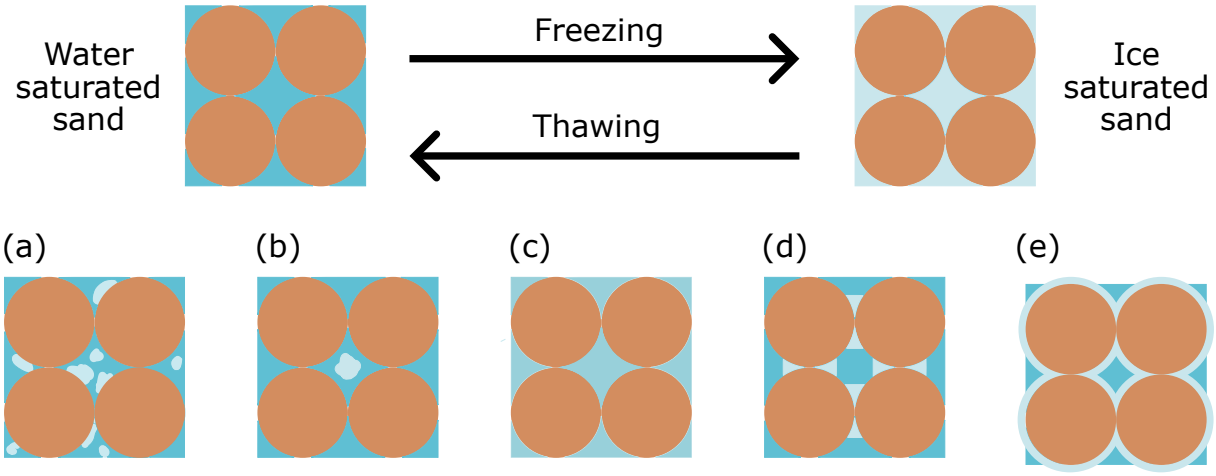

Figure 3.3: Schematic representation of ice distribution in an early stage of a freezing process. Grains are surrounded by water and/or ice. (a) Freezing with a patchy ice distribution. (b) Freezing in the middle of the pores and not at grain contacts. (c) Homogeneous freezing. (d) The water freezes at contact points and (e) around the grains and acts as cement.

Cementation effects

If the water starts to freeze at the grain contacts or all around the grains (Figure 3.3 (d) and (e), respectively), the ice may act as cement.

To calculate the effective elastic moduli of dry rocks when cement deposits at grain contacts, contact cementation theory (CCT) can be applied. This model assumes loose sandstone with direct grain contacts (Dvorkin and Nur, 1996). The contact cement reinforces the grain contacts and increases the stiffness of the rock. The initial cementation effect will cause a considerable velocity increase with only a small porosity decrease (Avseth et al., 2005). The effective bulk and shear moduli of a cemented rock, K_{CCT} and μ_{CCT}, can be expressed as

$$K_{CCT} = \frac{1}{6} n(1-\phi_0) M_C S_n, \tag{3.24}$$

$$\mu_{CCT} = \frac{3}{5} K_{CCT} + \frac{3}{20} n(1-\phi_0) \mu_C S_\tau, \tag{3.25}$$

where $M_C = K_C + \frac{4}{3}\mu_C$ (Dvorkin and Nur, 1996). K_C and μ_C are the bulk and shear moduli of the cement, respectively, and S_n and S_τ are parameters that are proportional to the normal and shear stiffnesses, respectively. The parameters S_n and S_τ depend on the amount of contact cement and the properties of the cement and grains. Equations describing the parameters are given in Appendix A.1.

The amount of contact cement can be expressed by the ratio, α, by

$$\alpha = \frac{a}{R}, \tag{3.26}$$

where a is the radius of the cement layer, and R is the grain radius.

The ratio, α, can be expressed with more complex equations depending on how the cement is deposited on the grains (Mavko et al., 2009). If all the cement is deposited at grain contacts, as in Figure 3.3 (d), the equation is

$$\alpha = 2\left[\frac{\phi_0 - \phi}{3n(1-\phi_0)}\right]^{\frac{1}{4}} = 2\left[\frac{S\phi_0}{3n(1-\phi_0)}\right]^{\frac{1}{4}}, \tag{3.27}$$

and if the cement is evenly deposited on the grain surfaces, as in Figure 3.3 (e), the

equation is

$$\alpha = \left[\frac{2(\phi_0 - \phi)}{3(1-\phi_0)}\right]^{\frac{1}{2}} = \left[\frac{2S\phi_0}{3(1-\phi_0)}\right]^{\frac{1}{2}}. \tag{3.28}$$

Here, S denotes the cement saturation of the pore space. The CCT restricts to small concentrations of cementation, i.e., S <15% (Johansen et al., 2003).

Chapter 4

Modeling

The physical properties of a rock determine its effective elastic moduli, which directly affect the seismic velocities of waves traveling through the rock. Rock physics modeling is used to investigate the connections between the physical rock properties and the seismic observations. I have used a forward rock physics modeling approach to compute effective elastic and seismic properties from known/chosen physical rock properties using MATLAB. Rock physics modeling may also be used for inversion modeling by estimating physical properties from seismic observations as in Johansen et al. (2013).

Several velocity models based on rock physics modeling are presented in this chapter and used for further investigation. I have conducted a series of seismic modeling experiments to investigate the effect of velocity variations due to freezing and thawing on the dispersion of surface waves, and the results of this are presented in Chapter 5. Usually, surface wave analysis aims at estimating the S-wave velocity profile by solving an inverse problem of model parameter identification based on experimental dispersion curve (Foti et al., 2018). In this thesis, I have produced synthetic seismic data from already known effective rock physics properties based on rock physics modeling (i.e., using a forward modeling approach). That is done to investigate how the dispersion curves change for numerous frozen and unfrozen layered shallow subsurface scenarios.

4.1 Rock physics modeling of frozen and unfrozen sediments

This thesis uses two main methods to calculate the effective elastic response of freezing and thawing sediments. One approach is based on a two-end-member mixing method using Hashin-Shtrikman bounds, and the other method is mainly based on the contact cementation theory and the self-consistent approximation. The bulk modulus and the shear modulus describe the freezing effects in the models.

The final P- and S-wave velocities are calculated with effective bulk and shear moduli found from the various models and the effective density. The effective density, ρ_{eff}, is defined as

$$\rho_{eff} = (1 - \phi_0)\rho_G + \phi_0 S_W \rho_W + \phi_0 S_I \rho_I, \tag{4.1}$$

where the subscripts G, W, and I represent grain, water, and ice, respectively, and S is the saturation.

4.1.1 Rock physics model 1: two-end-member mixing

The modeling used in Stemland et al. (2020b,a) is based on two-end-member mixing of fully frozen and unfrozen composites as presented in Dou et al. (2017). Figure 4.1 illustrates the workflow for the two-end-member mixing method. Member A is either a fully or patchy water saturated sand, and member B is either a fully or patchy ice saturated sand.

The first step in this modeling is to calculate the elastic moduli of a dry rock with the help of Hertz-Mindlin contact theory (Equations 3.12 and 3.13). The elastic moduli for quartz are, in many cases, used for the grain properties.

The second step is to calculate the bulk modulus of a fully water saturated rock using Gassmann's equations (Equations 3.22 and 3.23) with the results from Hertz-Mindlin contact theory as input. The elastic moduli for water are used for the fluid properties.

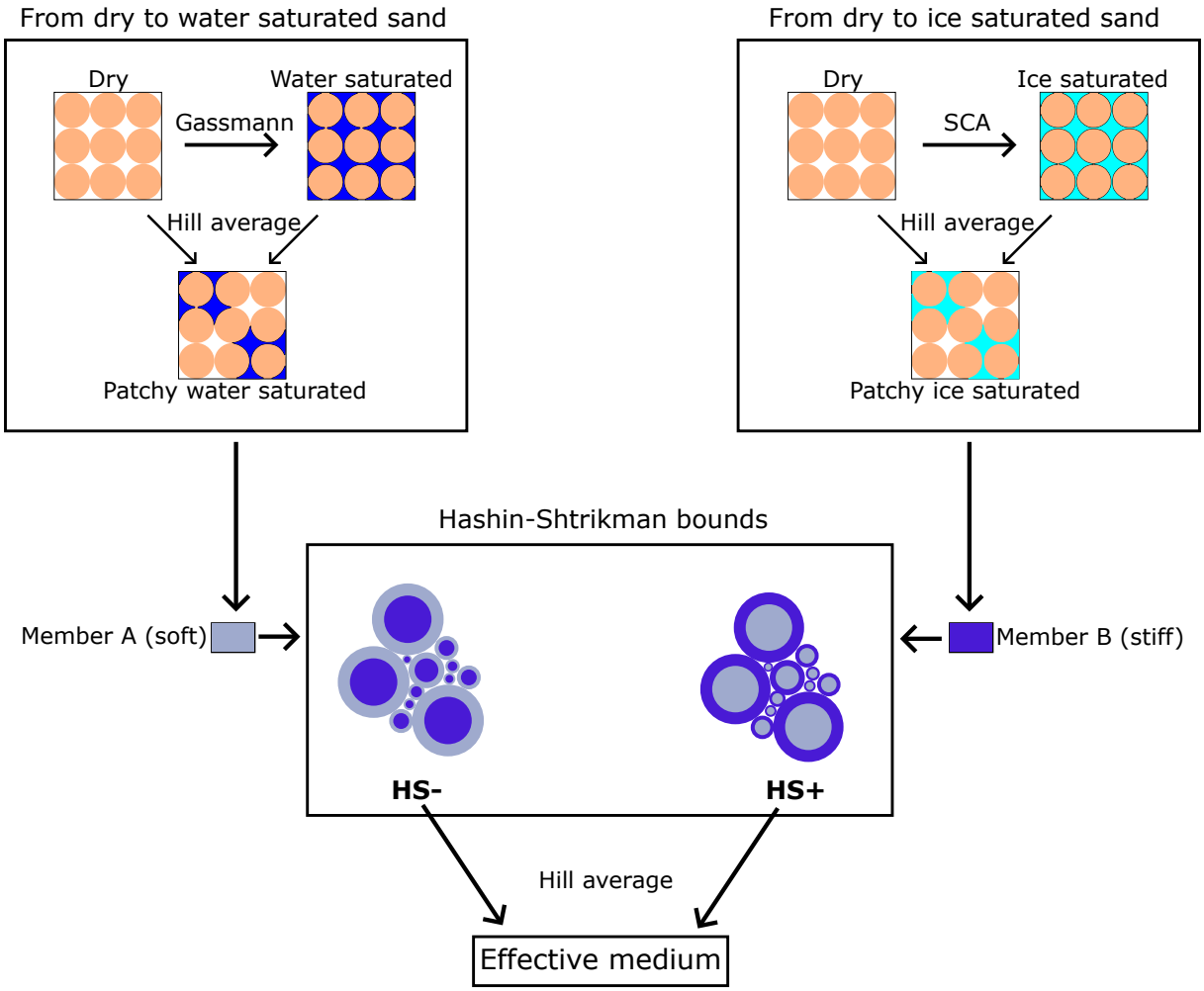

Figure 4.1: Schematic illustration of the two-end-member mixing approach. Member A represents either patchy or fully water saturated sand, and member B represents either patchy or fully ice saturated sand. HS bounds are found from the two end-members, and the Hill average is calculated from the upper and lower bounds to finally estimate the effective properties of the medium.

In the third step, the bulk modulus of a patchy water saturated rock is calculated. The arithmetic average of the dry rock modulus and fully water saturated modulus is calculated to estimate the patchy water saturated bulk modulus, K_{patchy_W}, by

$$K_{patchy_W} = \frac{1}{2}(K_{CT} + K_{sat}). \tag{4.2}$$

K_{CT} is the dry rock bulk modulus from Hertz-Mindlin contact theory, and K_{sat} is the fully water saturated bulk modulus from Gassmann's equations. The patchy water saturated shear modulus, μ_{patchy_W}, is independent of the fluid content inside the pores, i.e., $\mu_{patchy_W} = \mu_{sat} = \mu_{CT}$. For the case of Equation 4.2, the pore space is 50% water-saturated. Other concentrations of K_{CT} and K_{sat} are also calculated to investigate the

effect of pore saturation when the rock is not fully saturated.

The fourth step is to find the effective elastic moduli of a fully ice saturated rock. The fully ice saturated moduli are calculated using the SCA described in Chapter 3.3.2. For this case, I investigate two scenarios. Scenario 1 (K_1 and μ_1) assumes spherical or penny-shaped ice inclusions in an unknown background medium, and scenario 2 (K_2 and μ_2) assumes spherical grain inclusions in an unknown background medium. The two scenarios are written as

$$K_1 = S_I(K_I - K_{SCA})P_I, \tag{4.3}$$

$$\mu_1 = S_I(\mu_I - \mu_{SCA})Q_I, \tag{4.4}$$

$$K_2 = S_G(K_G - K_{SCA})P_G, \tag{4.5}$$

$$\mu_2 = S_G(\mu_G - \mu_{SCA})Q_G, \tag{4.6}$$

where the subscripts I and G denote ice and grain, respectively. These equations are solved iteratively for K_{SCA} and μ_{SCA}, where $K_1 + K_2 = 0$ and $\mu_1 + \mu_2 = 0$ is required. The results for K_{SCA} and μ_{SCA} are the fully ice saturated effective elastic moduli of the rock.

The arithmetic average of the dry rock moduli and the fully ice saturated moduli are derived to estimate the effective elastic moduli of a patchy ice saturated rock, K_{patchy_I} and μ_{patchy_I}. The equations used are

$$K_{patchy_I} = \frac{1}{2}(K_{CT} + K_{SCA}), \tag{4.7}$$

$$\mu_{patchy_I} = \frac{1}{2}(\mu_{CT} + \mu_{SCA}), \tag{4.8}$$

where K_{CT} and μ_{CT} are the dry rock moduli, and K_{SCA} and μ_{SCA} are the fully ice saturated moduli.

Subsequently, HS bounds (Chapter 3.2.2) are used to describe the transition from the unfrozen to the frozen state or vice versa. The water saturated rock is the soft end-member, and the ice saturated rock is the stiff end-member in the HS equations (Equation 3.6 and 3.7). The lower HS bound (HS^-) represents a rock when the frozen pore water occurs in local domains. The ice fragments are disconnected except when the rock is fully saturated and frozen. The upper HS bound (HS^+) describes how the ice gradually forms

as a connected aggregate in the rock's pore space (Stemland et al., 2020b).

The arithmetic average of the HS bounds is finally calculated using the Hill average. The seismic velocities used further from this rock physics modeling are based on the arithmetic average of the HS bounds.

4.1.2 Rock physics model 2: CCT and SCA

A rock physics model based on the paper by Johansen et al. (2003) is described in this section. The workflow of this method is illustrated in Figure 4.2.

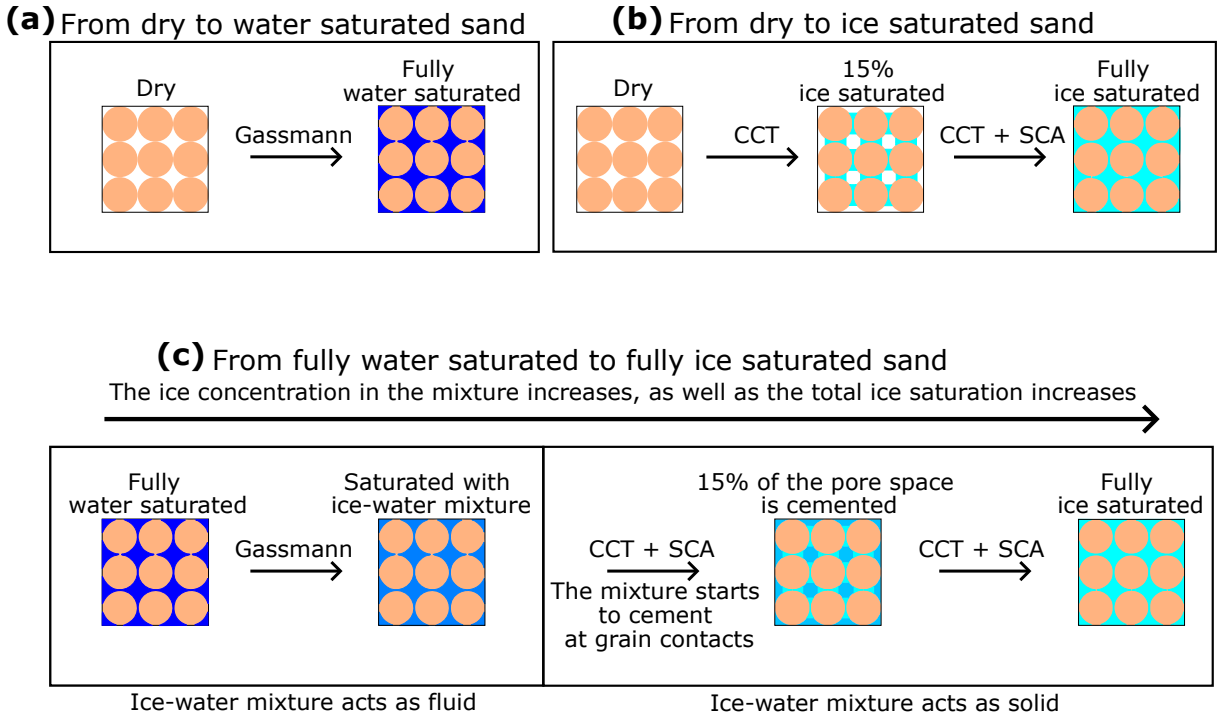

Figure 4.2: Schematic illustration of the ice cementing approach. (a) From dry to water saturated sand. (b) From dry to ice saturated sand. (c) From water saturated to ice saturated sand. The ice-water mixture that acts as cement is illustrated with another color than the surrounding pore space in this figure. However, it always contains the same ratio of ice and water as the surrounding ice-water mixture.

Firstly, the contact theory is used to estimate the elastic properties of unconsolidated grain composites when the voids are dry and uncemented (Equations 3.12 and 3.13).

Secondly, the elastic moduli of an ice-water mixture are calculated. The SCA is used to estimate how the elastic properties of water change when the water starts to freeze more and more, eventually becoming only ice. In this case, a mixture of only water and ice is

concerned. The SCA equations (Equations 3.14 and 3.15) are used for all scenarios from 0 to 100% ice in the ice-water mixture. Spherical inclusions are assumed for both water and ice. The elastic moduli for the ice-water mixture are illustrated in Figure 4.3. The figure shows a critical point at an ice saturation of 0.4. With ice saturation less than 0.4, the shear modulus is approximately zero, and the ice-water mixture acts as a fluid. When the ice saturation exceeds this critical point, the shear modulus is higher than zero, and the mixture acts as a solid. This ice-water mixture is further used as the pore fluid content in the sand.

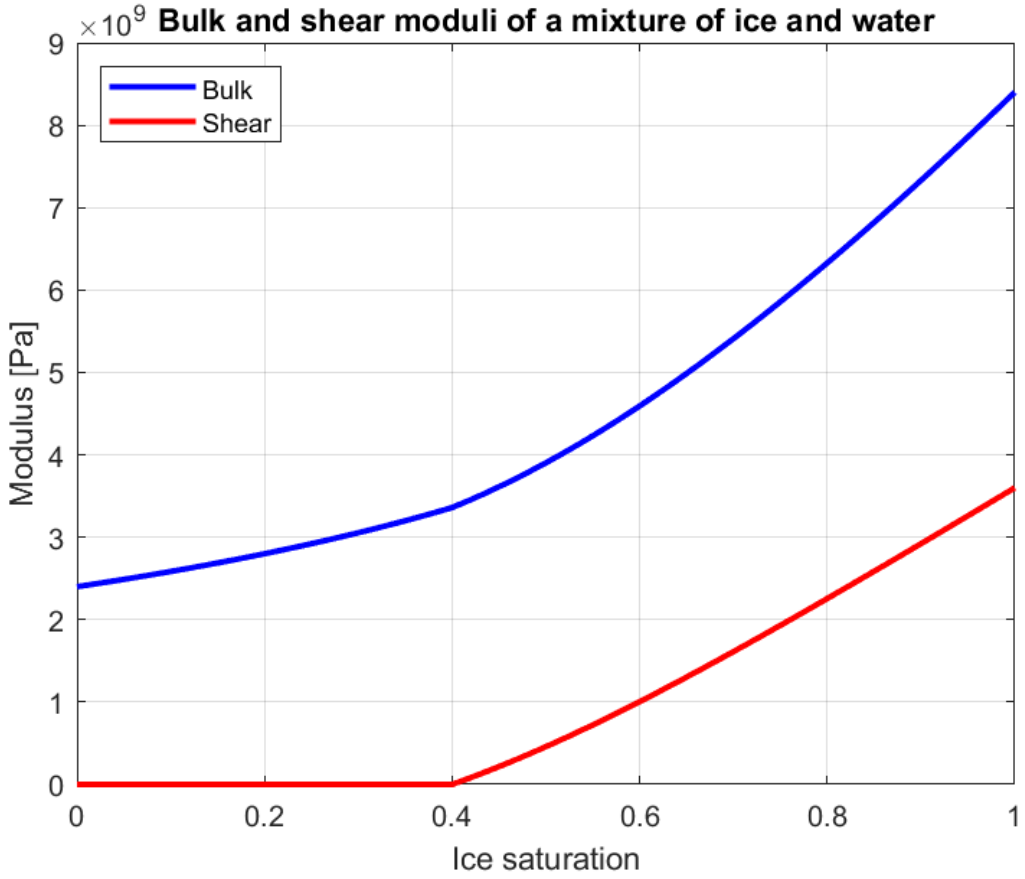

Figure 4.3: Elastic moduli of a mixture of ice and water as functions of ice saturation using the SCA with spherical inclusions assumption. For ice saturation equal to zero, the mixture only consists of water. When the ice saturation increases, the water saturation decreases as much.

Gassmann's equations (Equations 3.22 and 3.23) are used to find the effective properties of a rock when the pore space is fully saturated with the ice-water mixture when it acts as a fluid (i.e., 0 – 0.4 ice saturation).

When the ice-water mixture acts as a solid (i.e., ice saturation is more than 0.4), some of the ice-water mixture starts to act as cement between the contact points. For small concentrations of ice-water cement (1 – 15% cement concentration in the pore space), contact cementation theory is used to find the effective elastic properties of the medium, and the matrix consists of both the grains and the cemented ice-water mixture. The effective bulk and shear modulus, K_{CCT} and μ_{CCT}, are calculated (Equations 3.24 and 3.25). The cement properties are based on the ice-water mixture, and all cement is assumed to be deposited at grain contacts.

When 15% of the pore space is cemented, and the ice saturation continues to rise in the pore space, the SCA is used to calculate the effective elastic moduli of the rock. The method of combining CCT with SCA is based on the papers by Dvorkin et al. (1999) and Johansen et al. (2003).

After calculating K_{CCT} and μ_{CCT}, a continuous host material is defined with bulk and shear moduli, K_H and μ_H, respectively. The following set of equations are solved directly for the host properties,

$$\frac{1}{K_{CCT} + (4/3)\mu_{CCT}} = \frac{1-\phi}{K_H + (4/3)\mu_{CCT}} + \frac{\phi}{(4/3)\mu_{CCT}}, \tag{4.9}$$

$$\frac{1}{\mu_{CCT} + Z} = \frac{1-\phi}{\mu_H + Z} + \frac{\phi}{Z}, \tag{4.10}$$

where

$$Z = \frac{\mu_{CCT}(9K_{CCT} + 8\mu_{CCT})}{6(K_{CCT} + 2\mu_{CCT})}. \tag{4.11}$$

The final step in this rock physics model is to use the host properties in an SCA to estimate the effective elastic moduli when the ice saturation increases even more and finally ice fills the entire pore space. The same set of equations for solving the SCA system is used as in the two-end-member mixing approach (Equations 4.3,4.4, 4.5 and 4.6), but instead of the grain properties, the host properties are used. The resulting K_{SCA} and μ_{SCA} represent the effective elastic moduli of the sand for the varying ice saturation when the pore-filling ice-water mixture acts as a solid.

4.2 Seismic modeling of near-surfaces

Seismic modeling is an essential part of geophysical data processing. It is a technique for simulating wave propagation in the Earth that aims to predict a seismogram that a set of receivers record, given an assumed structure of the subsurface (Carcione et al., 2002). Seismic modeling may also be used to evaluate and design seismic surveys.

There are many approaches to seismic modeling. In this thesis, the seismic modeling is based on a full-wavenumber integration method called OASES (Schmidt and Jensen, 1985). The seismic modeling is done to generate synthetic seismic data corresponding to velocity models based on the rock physics modeling described in Chapter 4.1.

4.2.1 Workflow of surface wave analysis

Surface wave analysis aims to estimate near-surface S-wave velocity profile, and it is today widely adopted (Socco et al., 2010). S-wave velocity models are made by solving an inverse problem based on an experimental dispersion curve (Foti et al., 2018). Typically, the surface wave analysis is implemented in three steps regardless of which type of surface waves are investigated (Socco et al., 2010). The workflow is illustrated in Figure 4.4, where the three steps can all be attempted with several strategies. The first step is the acquisition of seismic data, which are represented in seismograms. In this thesis, OASES is used for that purpose (see Chapter 4.2.2 for details). The second step is to estimate the dispersion curves. Geogiga software is in this thesis used to look at the seismograms and to generate the dispersion images corresponding to the seismograms. The details of this step are described in Chapter 4.2.3. The third and final step is to do an inversion of the dispersion curves to obtain S-wave velocity profiles. Seismic inversion may be done by comparing synthetic data generated through forward modeling to observed data, then minimizing the error between them iteratively until a satisfactory match is reached (Socco and Strobbia, 2004). The last step is not performed in this thesis since the purpose is mainly to compare and analyze the possible variations of dispersion images for various subsurface scenarios. Also, inversion of dispersion curves containing strong higher modes, as is typical for data from permafrost environments, is not straightforward.

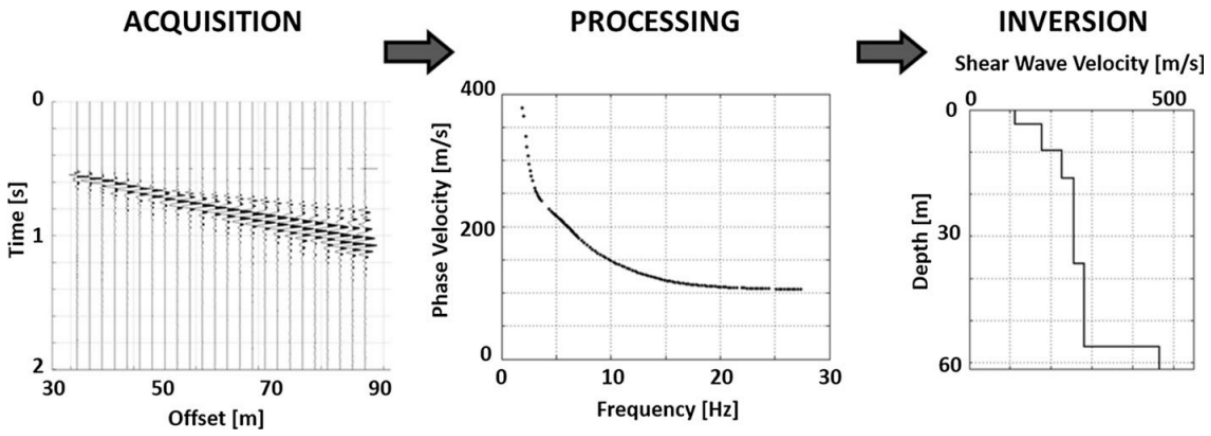

Figure 4.4: Main steps of the surface wave analysis workflow. The steps consist of generating seismic data, dispersion curve, and S-wave velocity profile (Foti et al., 2018).

4.2.2 Seismic survey and subsurface models

Acquisition of seismic data is performed with seismic receivers and either an active source or using ambient seismic sources (passive seismic). Seismic data can also be generated synthetically, as in the case of this thesis.

The multichannel analysis of surface waves (MASW) method has the most common acquisition layout, which consists of an array of evenly-spaced vertical geophones aligned with the seismic source (Foti et al., 2018). This layout is used for the synthetic data acquired in this thesis. The modeled receivers measure vertical motions, i.e., the effect of Rayleigh wave propagation is presented in the synthetic data.

The near-surface is modeled as vertical stacks of homogeneous and isotropic elastic layers. Each layer is characterized by its thickness, density, P- and S-wave velocities, and attenuation ratio. The velocities and densities used in these subsurface layered models are based on the rock physics velocity modeling described in Chapter 4.1. The attenuation ratio is set to 0.1, i.e., assuming constant attenuation. Several subsurface models are made with various distributions of frozen, unfrozen, and partly frozen layers (i.e., various distributions of low- and high-velocity layers). The purpose of testing that is to investigate which dispersion signatures the various models give. A variation in thickness and amount of layers are also tested to investigate how that influences the synthetic data.

For all cases, the source is defined as a point source at 0.01 m depth, and the receiver depths are set to 0.05 m depth. Various numbers of receivers and intervals between them are tested to investigate how that affects the results. Poor survey design can cause

aliasing. Aliasing is a form of distortion of the result, and it occurs when data are not sampled often enough in time or space (Steeples and Miller, 1998). Temporal aliasing happens at frequencies above the Nyquist frequency (Kearey et al., 2002). The Nyquist frequency, f_N, can be expressed as

$$f_N = \frac{1}{2\Delta t}, \tag{4.12}$$

where Δt is the sampling interval. Temporal aliasing occurs therefore when a wave is sampled with less than two points per time period for a signal (Haldorsen, 2021). Spatial aliasing issues may occur if the receiver distance is longer than half of the spatial wavelength of a propagating wavefield (Haldorsen, 2021).

4.2.3 Dispersion curves

The dispersion image is represented in a frequency-phase velocity spectrum. I use Geogiga to calculate the dispersion images corresponding to the seismic gathers generated with OASES. The peaks in the spectrum for the various models represent various solutions (combinations of frequencies and phase velocities) of the equation describing surface wave propagation. These solutions are called modes and define dispersion curves in the spectrum. The fundamental mode corresponds to the solution with the lowest phase velocity for a given frequency (Zhang et al., 2003; Stemland et al., 2020a). The phase velocity of each mode, V_{phase}, is expressed by

$$V_{phase} = \frac{2\pi f}{k}, \tag{4.13}$$

where f is the frequency (temporal frequency) and k is the wavenumber (spatial frequency) (Dou and Ajo-Franklin, 2014).

In a vertical heterogeneous media, numerous modes of propagation can exist at the same frequency and have various propagation velocities. The importance of the various modes depends on the stratigraphy and on the source, which can be problematic to interpret (Socco and Strobbia, 2004).

Each layer's thickness and S-wave velocity influence the dispersion curve the most, while P-wave velocity and density have a smaller impact (Foti et al., 2018). For further inversion

of the dispersion curves, the inverted parameters are therefore often reduced to thickness and S-wave velocity.

Chapter 5

Results

The following sections present the results of this thesis. Firstly, the results of the rock physics modeling are described in Chapter 5.1. The elastic moduli and seismic velocities are shown for various compositions of sediments. Thereafter, in Chapter 5.2, seismic gathers that are generated based on the rock physics models are provided along with their corresponding dispersion images. Several modeled scenarios are made of shallow layered subsurface, sometimes resulting in noticeable variations in the dispersion characteristics.

5.1 Rock physics models

This section shows how the subsurface's elastic properties and seismic velocities vary with changing ice saturation. Variations in the composition of sediments, pore fluid, and porosity are other examples that result in variations of the elastic properties. Numerous parameters are therefore tested to clarify which parameter variations that change the velocity model and how.

The following assumptions are made for all calculations unless anything else is stated:

- The critical porosity is 0.38 because, typically, unconsolidated quartz sand has a porosity between 0.36 and 0.4 (Nur et al., 1998).
- The coordination number is 9.1, corresponding to the porosity of 0.38 using Equation 3.2.
- The pressure is 24525 Pa, corresponding to a constant depth of 10 m, and an average

density of 2.5 g/cm^3.

- The pore space of the sediment is often assumed to be fully saturated by either water or ice, or a mixture of these two phases.
- The sand matrix only consists of quartz in most cases since this is a common mineral in permafrost (e.g., Gilbert et al., 2018).

The physical properties of constituents used for the modeling are given in Table 5.1.

Table 5.1: Physical properties. The values are taken from Mavko et al. (2009) and Johansen et al. (2003).

	Bulk modulus (GPa)	Shear modulus (GPa)	Density (g/cm^3)
Quartz	37.0	44.0	2.65
Feldspar	37.5	15.0	2.62
Clay (Kaolinite)	1.5	1.4	1.58
Water	2.4	0.0	1.0
Ice	8.4	3.6	0.92

5.1.1 Elastic and seismic properties as functions of ice and water saturation

The elastic moduli of a rock change with the amount of water in its pore space, as shown in Figure 5.1. In this figure, zero water saturation means that the rock's pore space is empty. The shear modulus is constant, as assumed from Gassmann's equations. However, the increasing bulk modulus with increasing water saturation indicates a stiffer medium when the amount of pore-filling water in an initially dry porous rock increases.

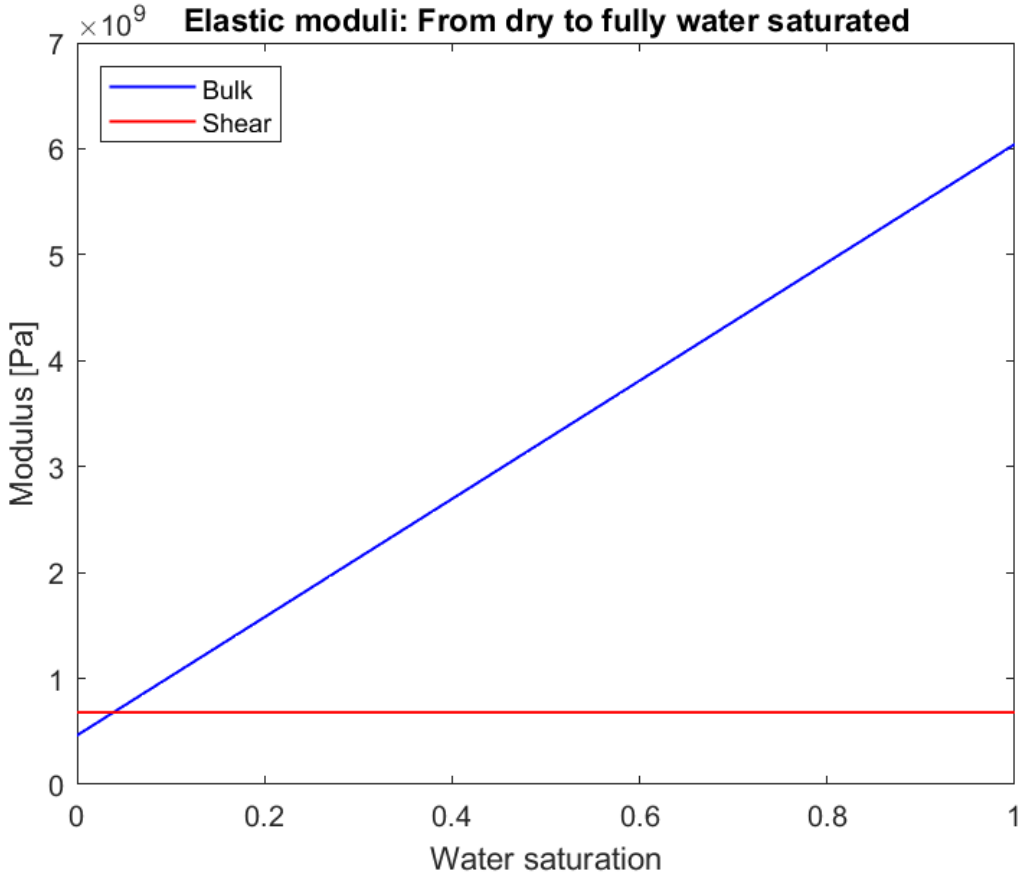

Figure 5.1: Effective elastic moduli of a porous rock as functions of water saturation. The pore space only consists of water and empty space. The values yield both rock physics model 1 and rock physics model 2.

Figure 5.2 shows how the elastic moduli of a porous rock change with the amount of ice in its pore space. The results are shown for the two different rock physics models described in section 4.1.1 and 4.1.2, respectively. The pore space is empty when the ice saturation is zero. The rock's resistance to both bulk and shear deformation increases with increasing ice saturation, indicating a stiffer medium. The elastic moduli are higher when ice is in the rock's pore space than when the same amount of water is in its pore space, corresponding to the higher moduli of ice. For rock physics model 2, the moduli increase rapidly when the ice saturation starts to increase from zero due to the cementation effect.

(a)

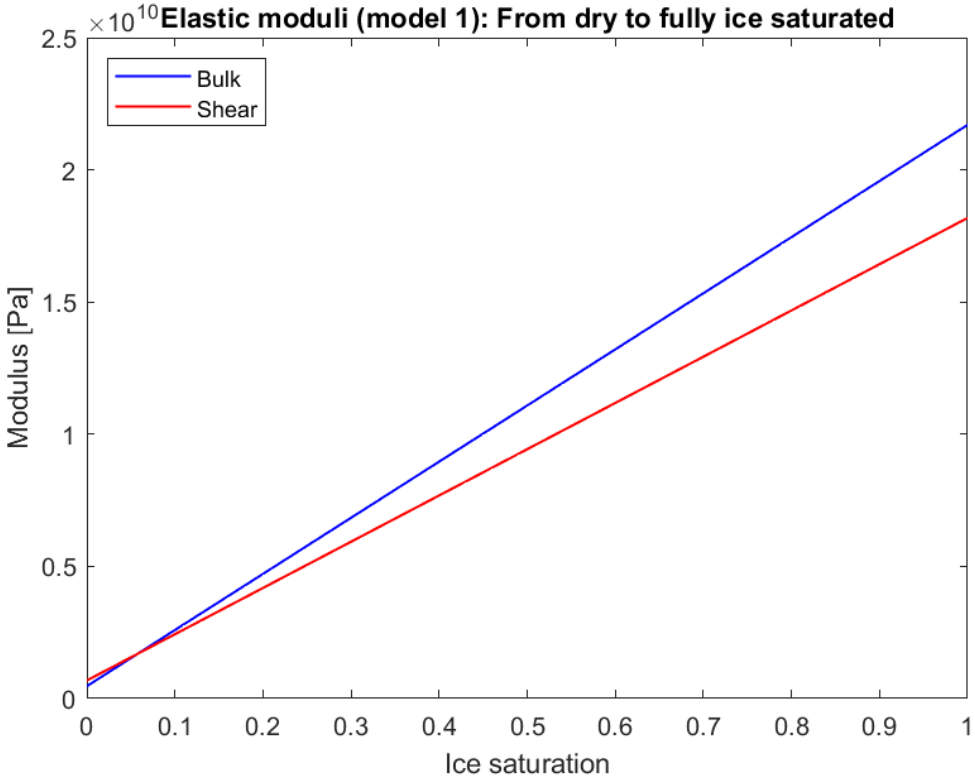

(b)

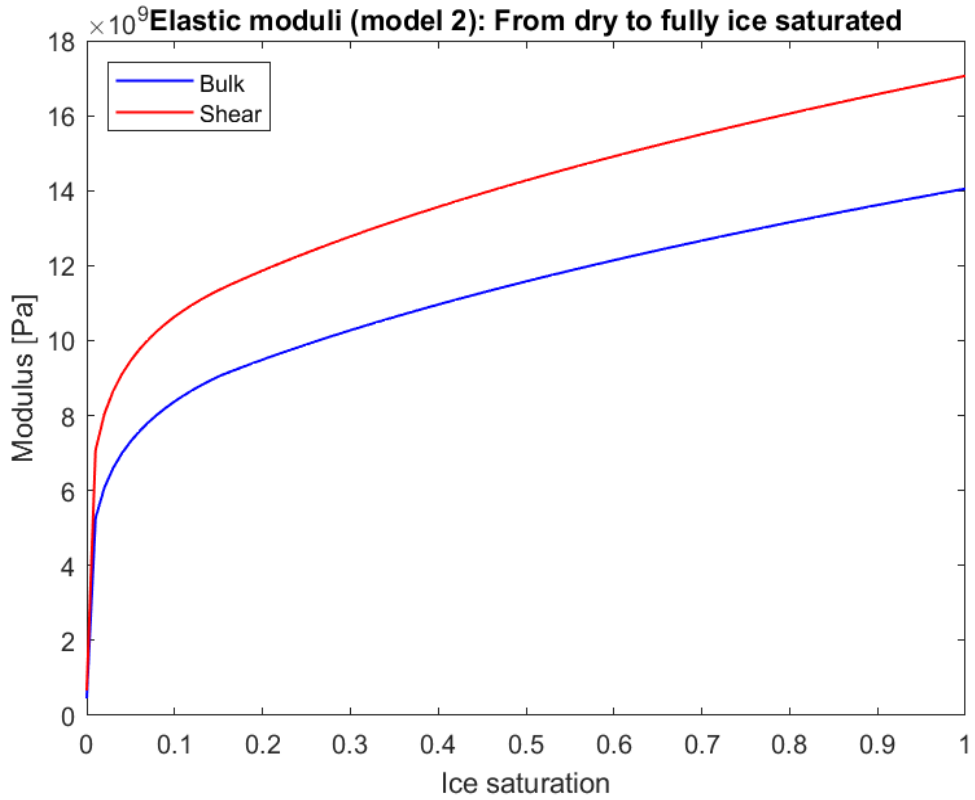

Figure 5.2: Effective elastic moduli of a porous rock as functions of ice saturation based on (a) rock physics model 1 and (b) rock physics model 2. The pore space only consists of ice and empty space.

Elastic moduli: rock physics model 1

The first rock physics model (rock physics model 1) assumes a porous sandstone consisting of quartz and is fully pore saturated with water and/or ice. Figure 5.3 shows the upper and lower Hashin-Shtrikman bounds and the arithmetic average of both shear and bulk moduli as functions of ice saturation. When the rock has zero ice saturation, the pore space is fully saturated by water. The model assumes spherical inclusion in SCA. When the ice saturation increases, the increase of elastic moduli indicates a stiffer and more rigid medium.

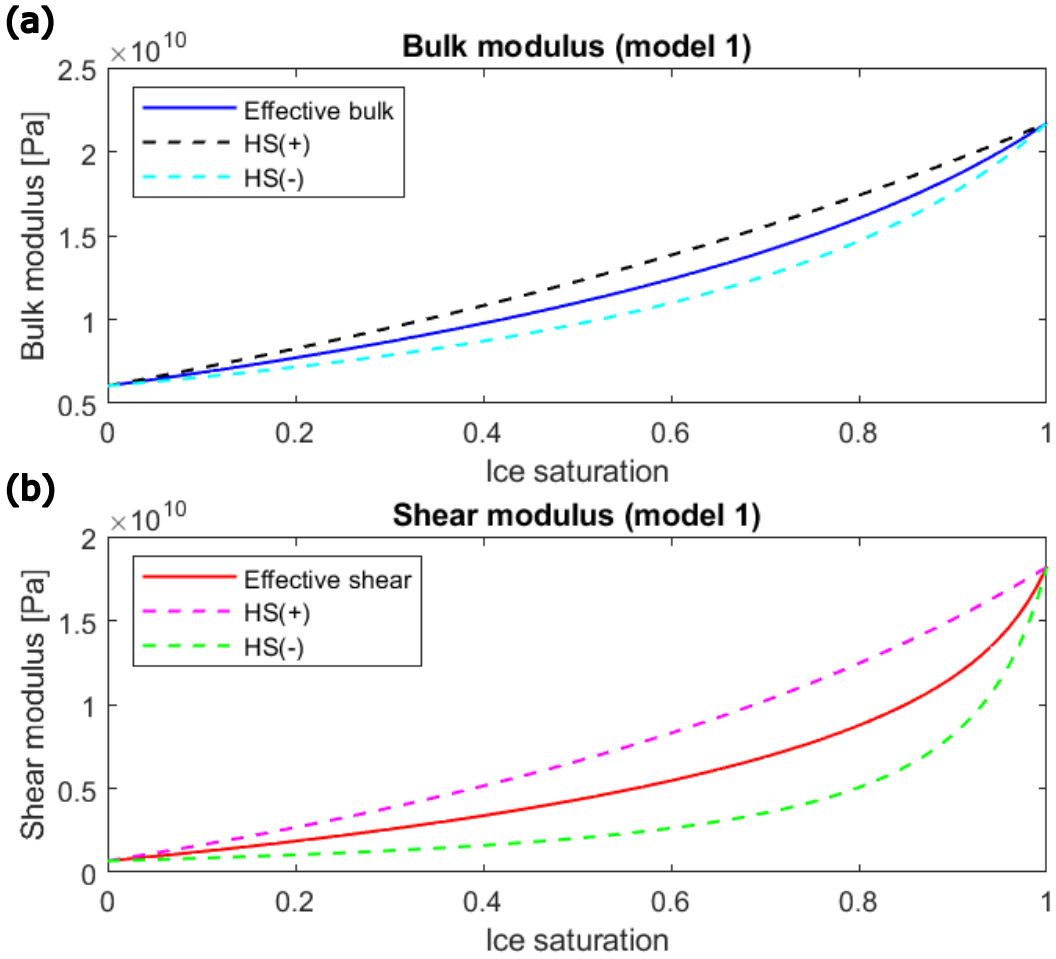

Figure 5.3: (a) Effective bulk and (b) shear moduli, and their HS bounds, of a fully water and/or ice saturated rock based on rock physics model 1.

Elastic moduli: rock physics model 2

The elastic moduli for the same fully saturated porous sandstone, but based on rock physics model 2, are shown in Figure 5.4. For the SCA, spherical inclusions are assumed for both grains and ice fragments. The constant shear modulus at ice saturation between

0 and 0.4 indicates that the ice-water mixture in the rock's pore space acts as a fluid in that interval. The "jump" from lower to higher moduli at 0.4 ice saturation indicates a transition from fluid to solid behavior of the ice-water mixture.

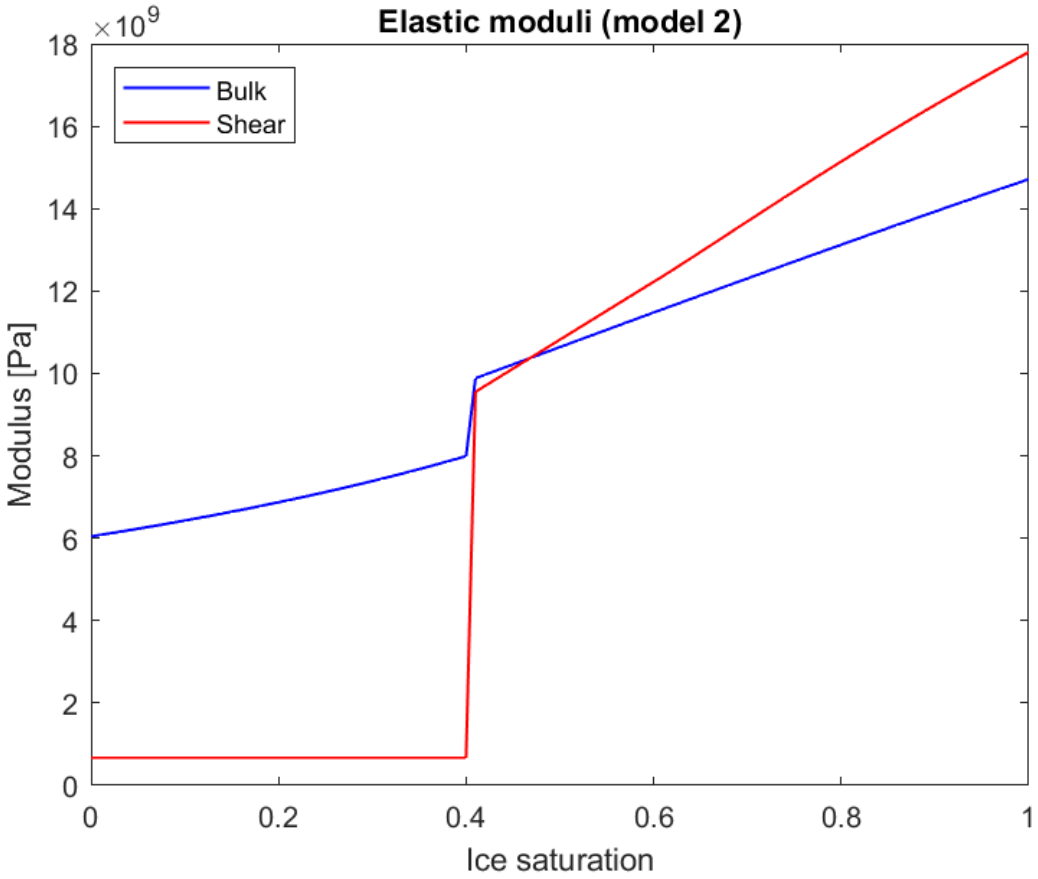

Figure 5.4: Effective elastic moduli of a fully water and/or ice saturated rock based on rock physics model 2.

Seismic velocities: rock physics model 1 and 2

The same curve effects as seen in the elastic moduli graphs for increasing ice saturation are shown for the seismic velocities. To compare the two rock physics models described in Chapter 4.1, equal model parameters of a porous rock are used for both models. Spherical inclusions are assumed for both the grains and ice fragments in the SCA. In Figure 5.5, both rock physics models show that the velocities increase with the degree of freezing (i.e., as the medium gets stiffer). However, the geometrical ice distribution differs, so the velocity curves are unequal for the two cases. That indicates that the velocities also depend on the distribution of the ice fragments and not only the amount of ice.

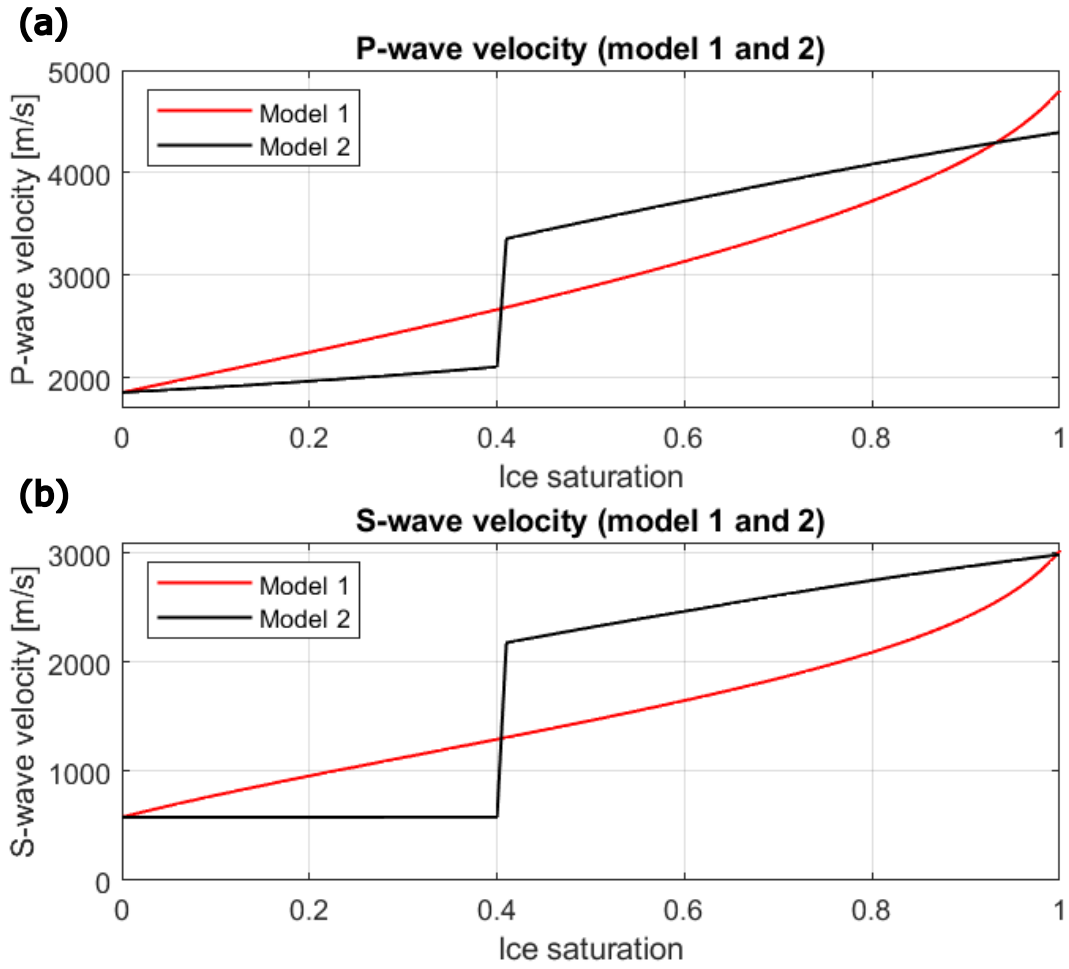

Figure 5.5: (a) P-wave and (b) S-wave velocities of a fully water and/or ice saturated rock based on rock physics model 1 and 2. Spherical inclusions are assumed for both the grains and ice fragments. Note that the two models use different methods to calculate the fully saturated rock, resulting in different velocities also at the endpoint.

5.1.2 Variation in the assumed shape of ice fragments

Various shapes of ice fragments are tested in the rock physics models to investigate how they affect the elastic moduli and seismic velocities of an ice saturated rock. Both spherical and penny-shaped inclusion assumptions are used for ice fragments in the stiff end-member in rock physics model 1. The resulting elastic moduli and seismic velocities as functions of ice saturation are shown in Figure 5.6. The spherical inclusion assumption gives higher bulk and shear moduli (i.e., stiffer medium) than the penny-shaped assumption. The penny-shaped ice inclusion model gives a similar P-wave velocity to rock physic model 2 for a fully ice saturated rock, but it gives a lower S-wave velocity for this endpoint.

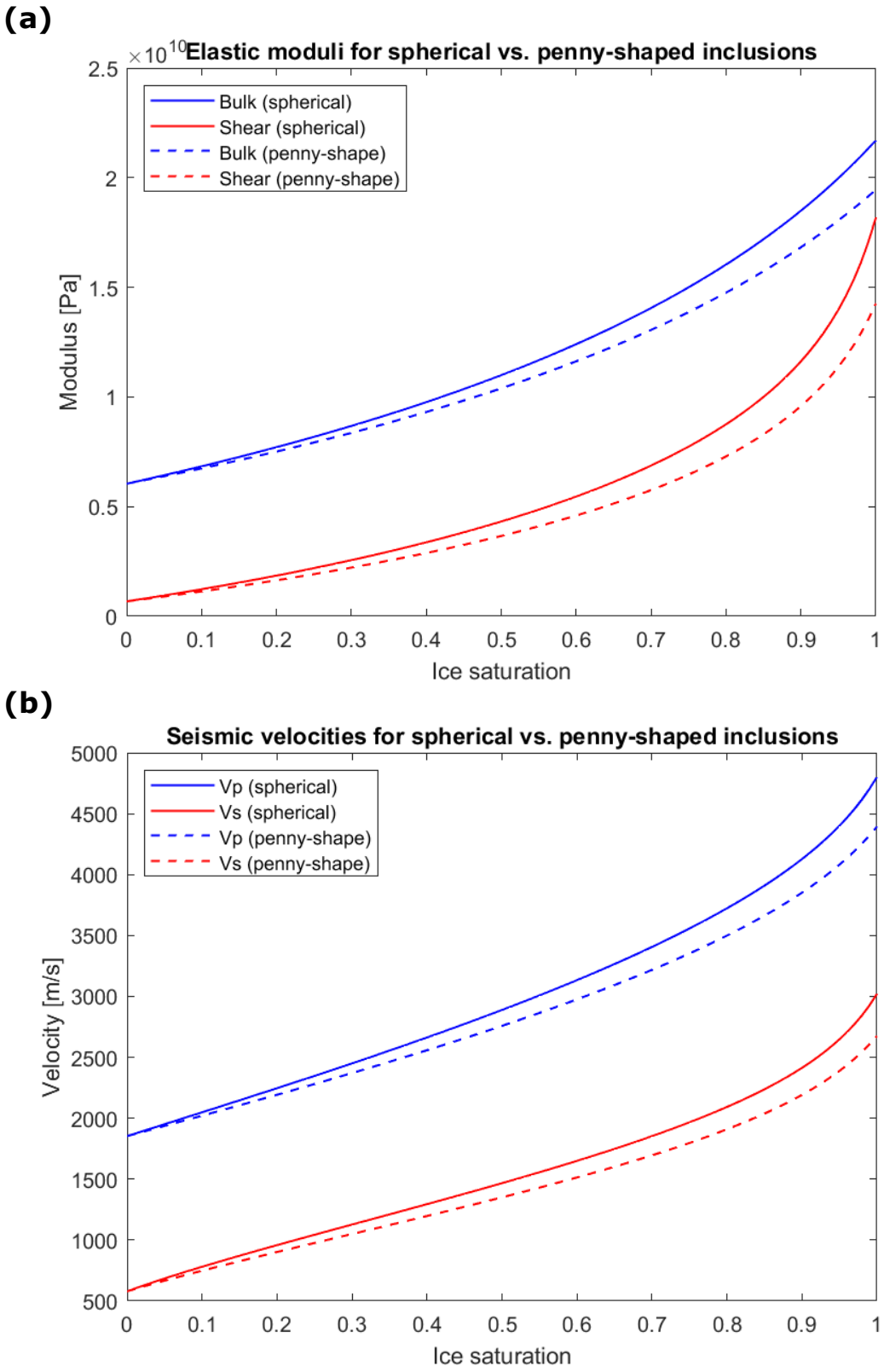

Figure 5.6: (a) Effective elastic moduli and (b) seismic velocities of a fully water and/or ice saturated rock based on rock physics model 1 with various ice fragment shapes. The results of both spherical and penny-shaped ice inclusion assumptions for the fully ice saturated end-member are shown.

5.1.3 Variation in porosity

The effective elastic moduli and seismic velocities are calculated for rocks with various porosities to investigate the porosity effect. Figure 5.7 shows the elastic moduli and seismic velocities when three different values of critical porosity are assumed for the same rock. The elastic moduli are higher for lower porosities, indicating a stiffer medium, and they have more considerable variations when the rock has more ice than water in its pore space. The elastic moduli increase more rapidly for higher concentrations of ice. The shear modulus for each porosity has almost the same values at zero ice saturation. The reason is that shear modulus is not affected by the presence of a nonviscous fluid in the pore space, which is water in this case, as described in Chapter 3.3.3. However, higher porosity in the rocks results in a slightly lower shear modulus. Since the variation in fluid does not affect the value when it is fully water saturated, the only reason for the variation in shear modulus is the effect of porosity variations. The variation in porosity has the same effects on the seismic velocities as for the elastic moduli (Figure 5.7 (b)).

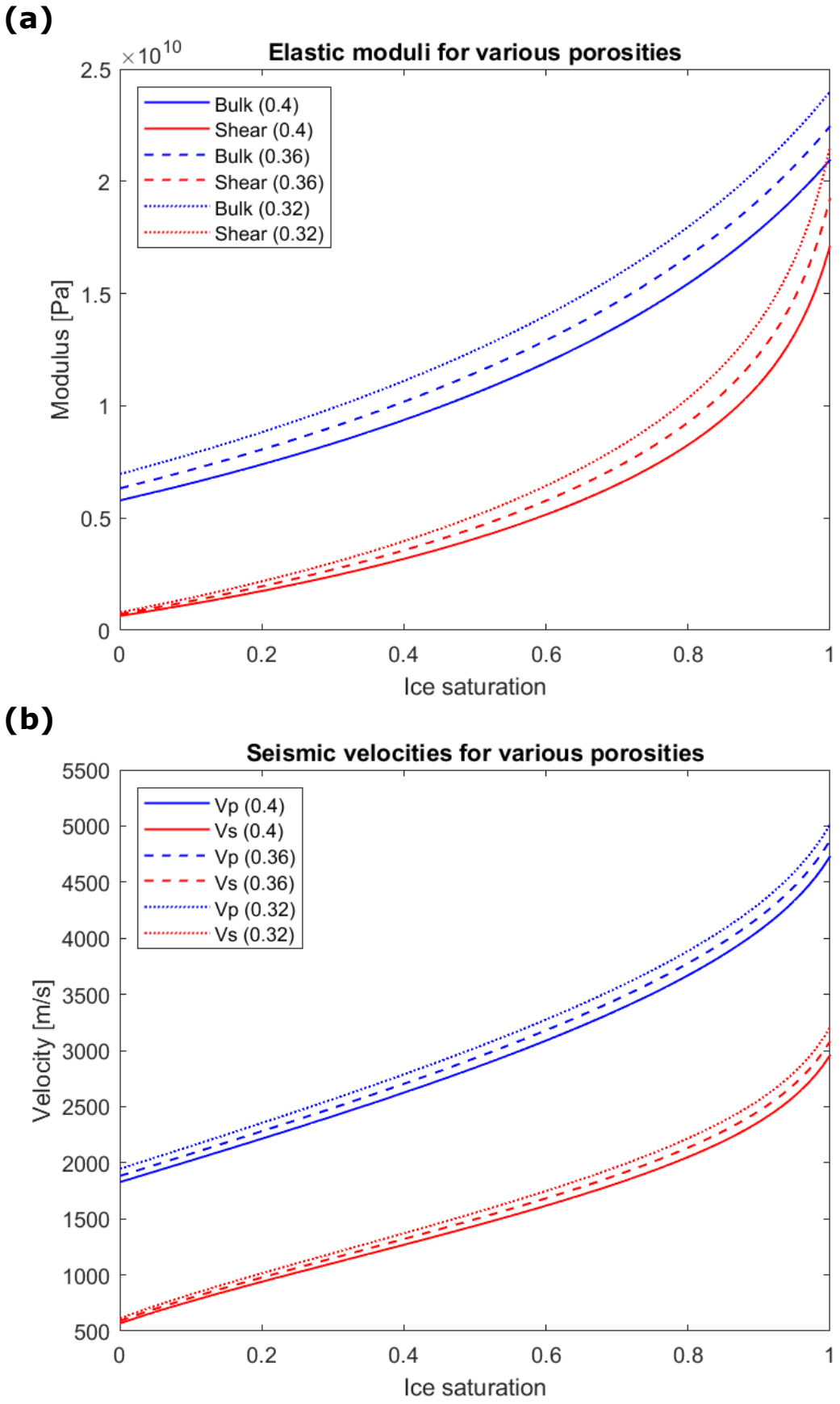

Figure 5.7: (a) Effective elastic moduli, and (b) seismic velocities of a fully water and/or ice saturated rock based on rock physics model 1 with varying porosity. Three different cases of critical porosity are shown with porosity equal to 0.4, 0.36, and 0.32. Spherical inclusions are assumed for both grains and ice fragments in the SCA.

5.1.4 Variation in pore saturation

Variations in pore saturation in a rock are tested based on rock physics model 1. Figure 5.8 shows the effective elastic moduli found from the arithmetic average of the HS bounds and presents the varying pore saturation: fully, 75%, 50%, and 25%. The elastic moduli are higher for increased pore saturation because ice has significantly higher elastic moduli than air (and water has a higher bulk modulus than air). At zero ice saturation, the shear modulus is equal for all cases due to the non-existent shear modulus in water. However, they increase significantly as soon as the water transfers to ice, and the increasing elastic moduli indicate that they are very sensitive to freezing.

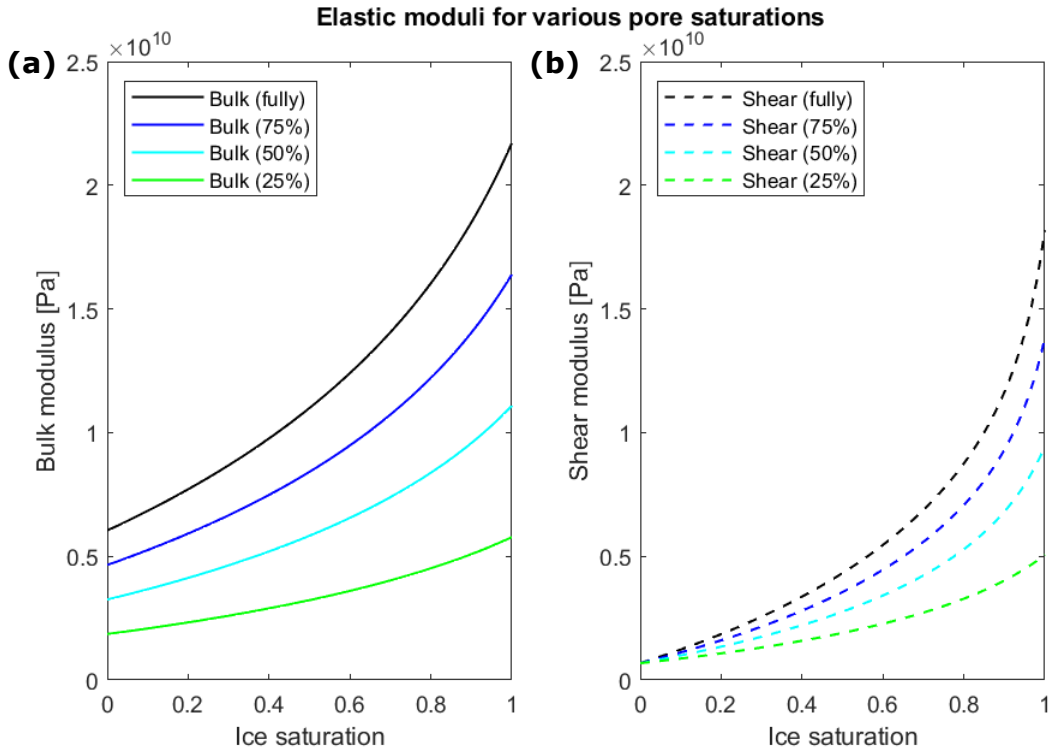

Figure 5.8: (a) Bulk modulus and (b) shear modulus of a water and/or ice saturated rock based on rock physics model 1 with varying pore saturation. Fully, 75%, 50%, and 25% pore saturation are shown. Spherical inclusions are assumed for both grains and ice fragments in the SCA.

Figure 5.9 shows the seismic velocities for the corresponding elastic moduli from Figure 5.8. The velocities are also higher for higher pore saturation due to the higher moduli of ice than air, except for S-wave velocity close to zero ice saturation since higher saturation increases density and reduces velocity.

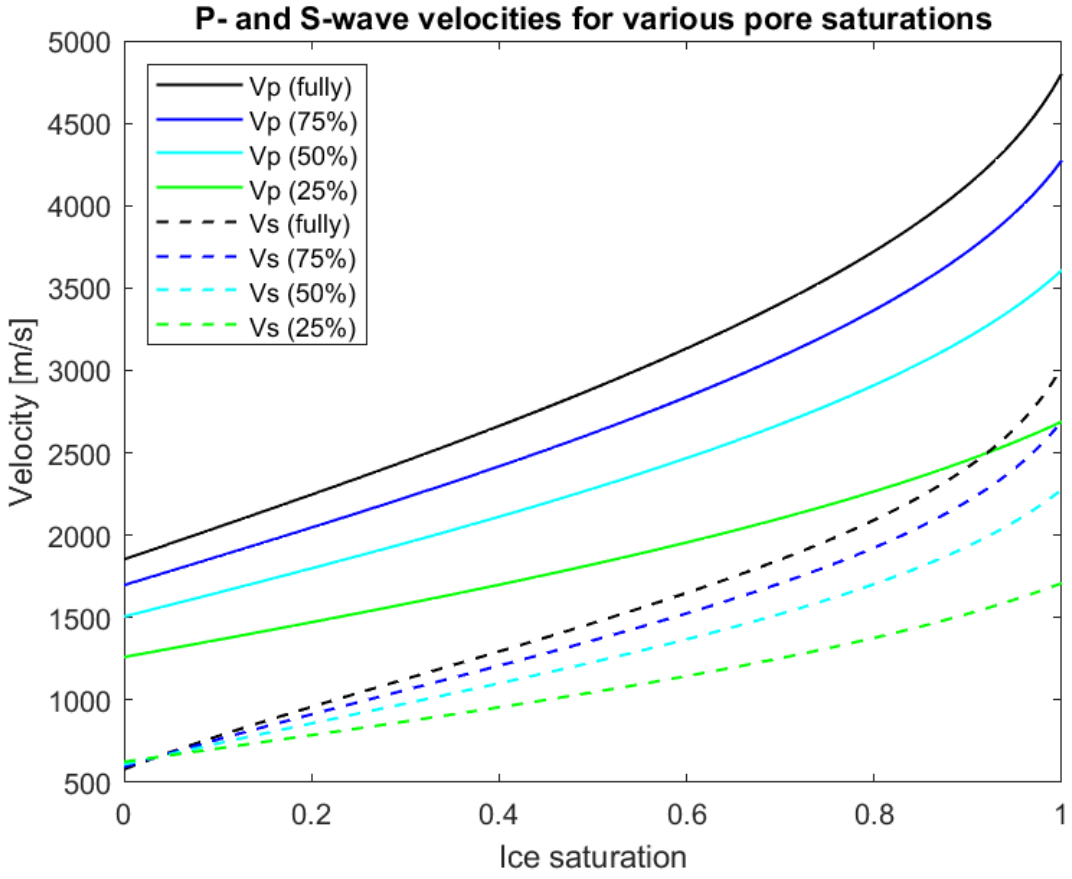

Figure 5.9: P- and S-wave velocities of a water and/or ice saturated rock based on rock physics model 1 with varying pore saturation. Fully, 75%, 50%, and 25% pore saturation are shown. Spherical inclusions are assumed for both grains and ice fragments in the SCA.

5.1.5 Variation in grain properties

The type of material varies in the Earth's subsurface, as do the properties of the various materials. The properties of quartz, feldspar, and clay, which are often found in permafrost (e.g., Gilbert et al., 2018), are used in models of fully water and/or ice saturated rocks. The velocity results based on rock physics model 2 are plotted in Figure 5.10. All other parameters are assumed to be equal. Lower velocities are present for softer grain properties (properties are shown in Table 5.1). The "jump" in velocities at 0.4 ice saturation indicates the transition from fluid to solid sediment behavior, and it is not as significant for the softer minerals as for the stiffer ones. The difference between fully water saturated and fully ice saturated is also less for the softer minerals. That indicates that the soft sediments are less sensitive to freezing than the stiffer sediments.

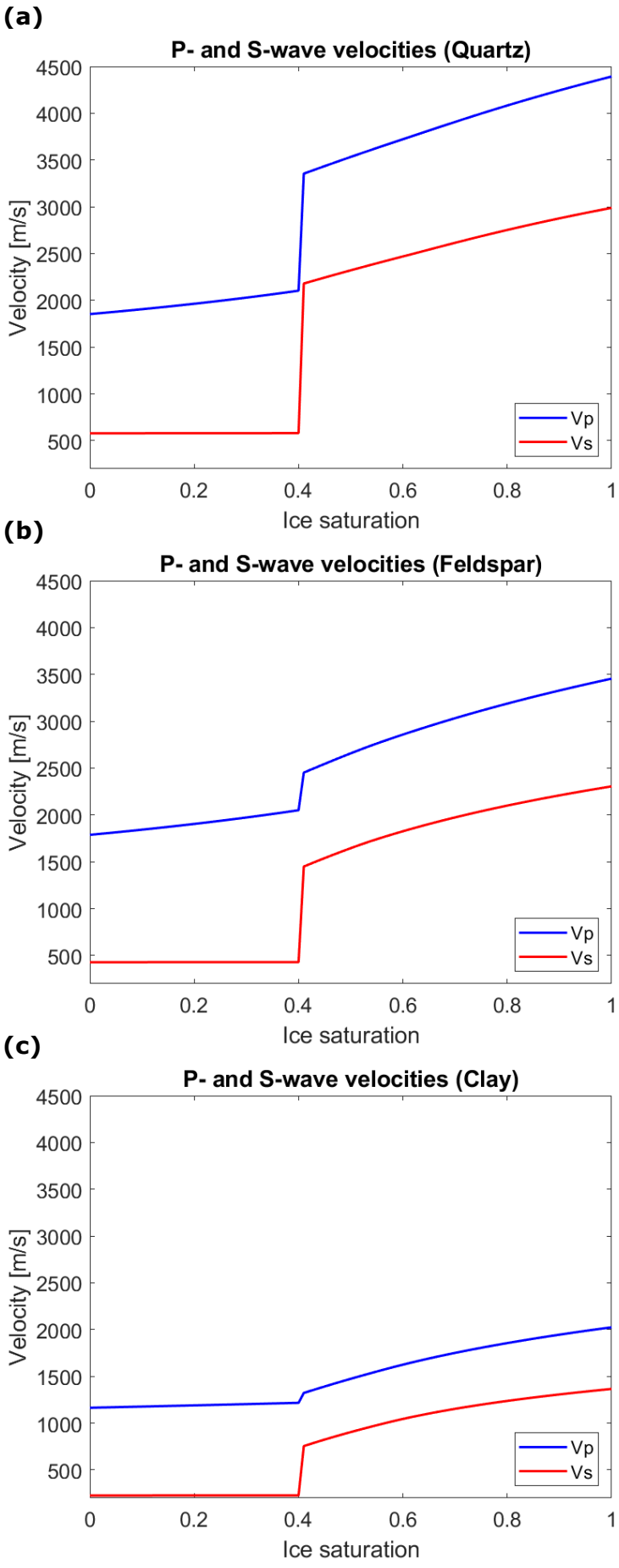

Figure 5.10: P- and S-wave velocities of a fully water and/or ice saturated rock based on rock physics model 2 with various grain materials: (a) quartz, (b) feldspar, and (c) clay.

5.2 Seismic data and dispersion curves

Some seismic modeling experiments are conducted for further investigation of freezing and thawing effects on the dispersion of surface waves, and are shown in this chapter. The first section shows results from models when the seismic velocities increase gradually with depth. That is often the case in unfrozen ground as well as in permafrost. Results from subsurface models with decreasing velocity with depth are shown in the second section. The last section shows results from more irregular velocity gradients, typical for saline permafrost.

The variation in elastic properties in the shallow subsurface changes the surface wave signatures represented in dispersion images. For all dispersion images, the highest amplitude is represented with red and the lowest amplitude with blue. However, the values in the amplitude scale are not equal for all figures, and therefore, the amplitude of two different images can not be compared. Also, note that all arrows in the figures are interpretations. The seismic gathers start from an offset at 50 m (often corresponding to trace number 50) due to noise in the traces close to zero offset.

5.2.1 Increasing ice saturation with depth

Typically, an upper active layer above permafrost is thawing and freezing seasonally, resulting in varying velocity during the year, and sometimes the ice saturation increases with depth. The first layer model, LM1, with properties from Table 5.2, represents near-surface where the upper 10 m has varying ice saturation. This model is a 5-layered 2D model without lateral variations. The seismic gather and its corresponding dispersion image for LM1, with seismic velocities based on rock physics model 1, are shown in Figures 5.11 (a) and (d). Figures 5.11 (b) and (e) show the results for a model similar to LM1 but with a uniform layer thickness of 4 m (LM1-U4), and Figures 5.11 (c) and (f) show the results for LM1 with uniform layer thickness of 6 m (LM1-U6). The ice saturation increases with depth in the model, resulting in stiffer layers with depth. In this case, 300 receivers are used with a spacing of 1 m. The porosity is constant with a value of 0.38 for all layers, and the pore space is fully saturated by either water, ice, or both. Quartz is the only mineral in the sand matrix.

Table 5.2: 5-layered 2D models: LM1, LM1-U4, and LM1-U6.

Layer	Thickness [m]			Ice saturation
	LM1	LM1-U4	LM1-U6	
1	0.5	4	6	0.2
2	1	4	6	0.5
3	1.5	4	6	0.7
4	7	4	6	0.8
5	–	–	–	1

For the first case (LM1), the seismic gather and the dispersion image barely show dispersion, providing one visible mode, which can be interpreted as the fundamental mode. For the second and third cases (LM1-U4 and LM1-U6), the upper layers are thicker (i.e., the intersections between the layers are more spread out), and the seismic data clearly show surface wave dispersion. The dispersion images provide distinct modes and the first higher order modes appear at different frequency ranges for these two cases. Weak events are also present next to the first higher order modes, which may be signs of other higher order modes. However, all three cases indicate that the thickness of the layers is important for the resulting dispersion characteristics of Rayleigh waves.

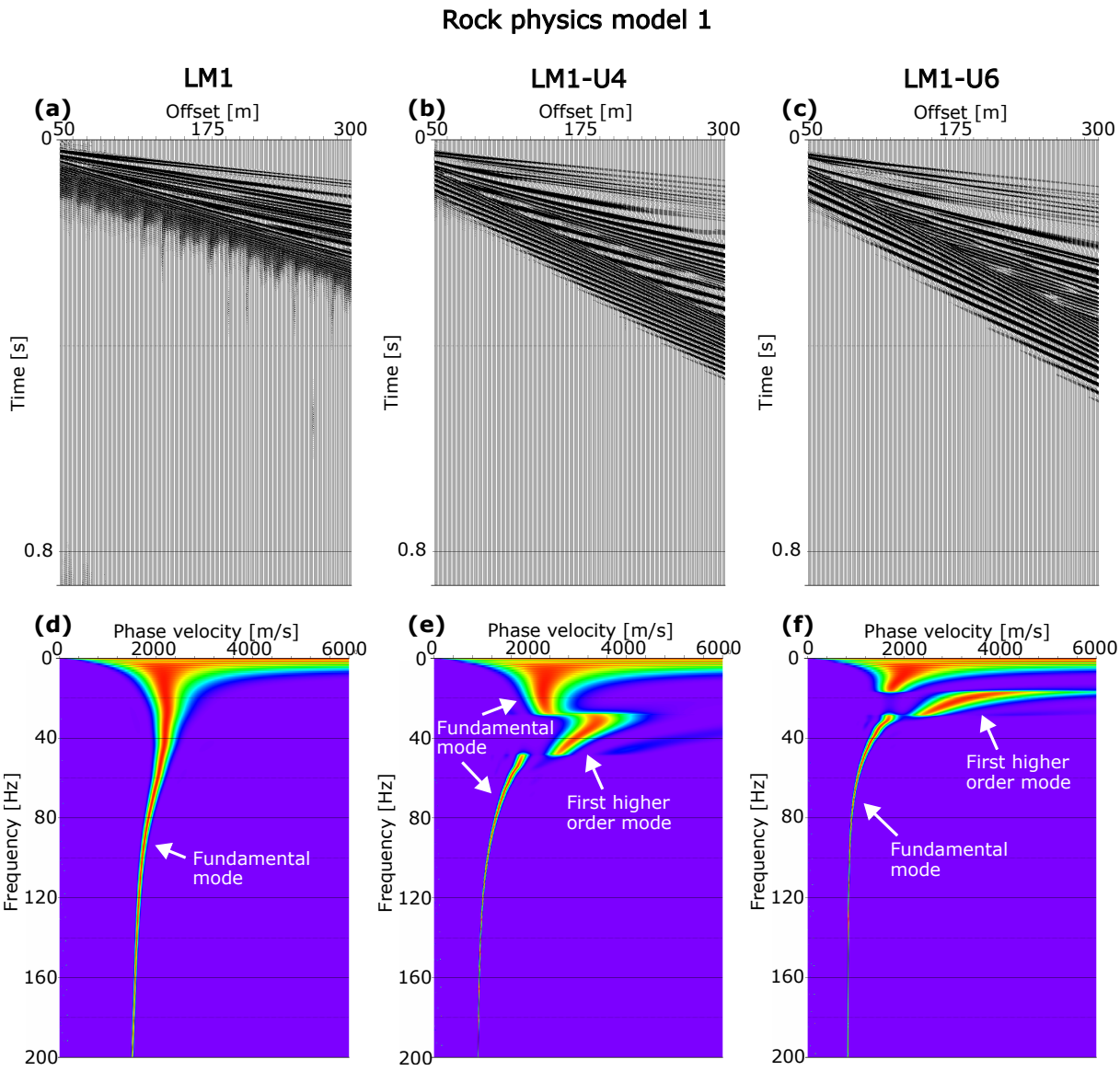

Figure 5.11: Top row: synthetic seismic gathers for (a) LM1, (b) LM1-U4, and (c) LM1-U6. Bottom row: corresponding dispersion images for (d) LM1, (e) LM1-U4, and (f) LM1-U6. The seismic velocities are based on rock physics model 1.

The same seismic modeling is done for LM1 with seismic velocities based on rock physics model 2. The results are shown in Figure 5.12. The dispersion curves are slightly different due to the velocity changes, but they show more dispersion when the thickness of the layers are 4 m and 6 m, as for the previous case (Figure 5.11).

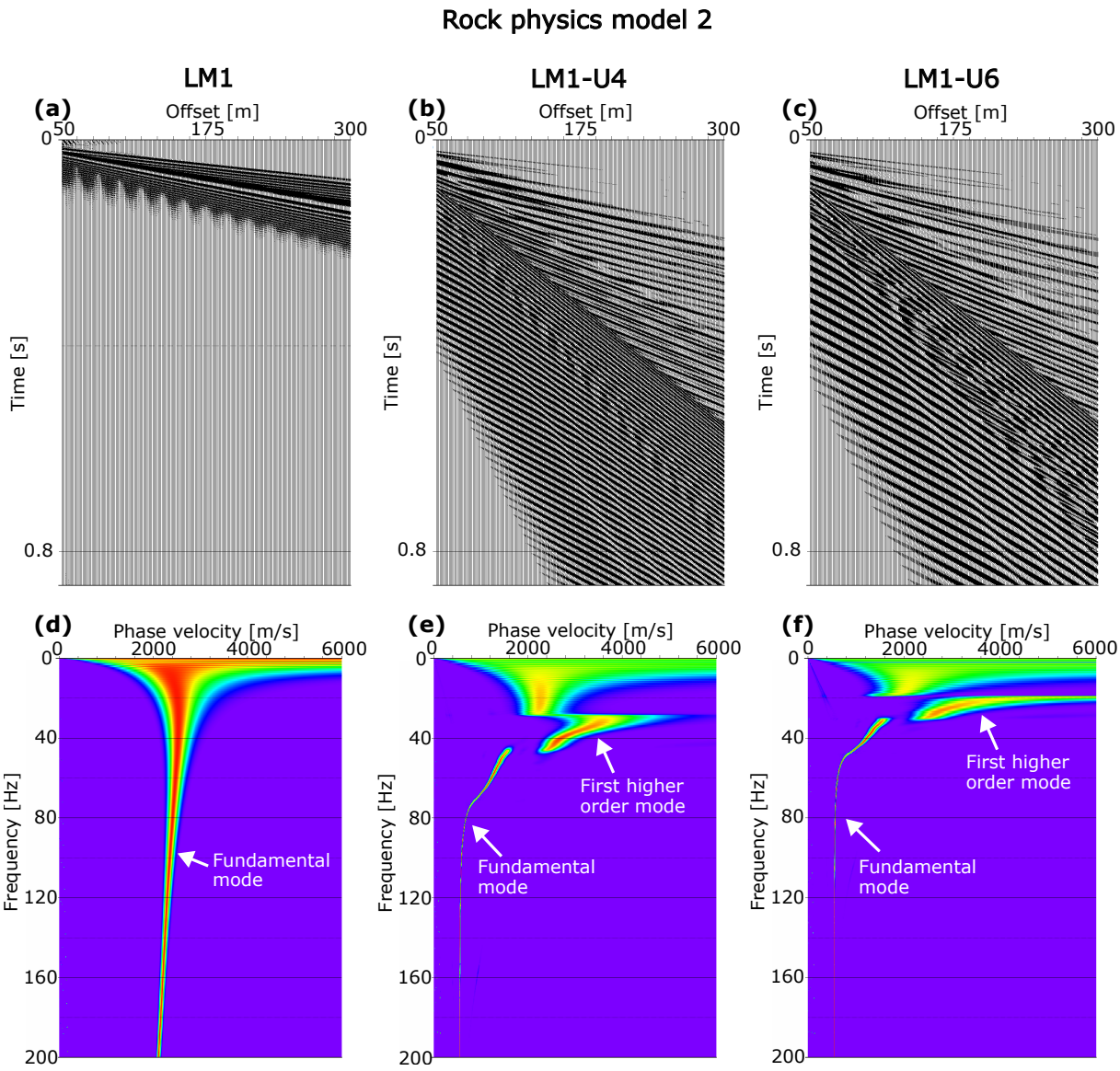

Figure 5.12: Top row: synthetic seismic gathers for (a) LM1, (b) LM1-U4, and (c) LM1-U6. Bottom row: corresponding dispersion images for (d) LM1, (e) LM1-U4, and (f) LM1-U6. The seismic velocities are based on rock physics model 2.

Another layer model, LM1a, is represented in Table 5.3. The layers in this model are 4 m thick except for the first and second layers, which are 6 m and 2 m, respectively, and the ice saturation for the layers is the same as for the previous cases. The results are shown in Figure 5.13. Here, the seismic velocities are based on rock physics model 2. This figure is very similar to the case when all layers are 6 m (LM1-U6). Hence, Figures 5.12 and 5.13 indicate that the changes in the upper part of the subsurface affect the dispersion characteristic the most.

Table 5.3: 5-layered 2D model: LM1a.

Layer	Thickness [m]	Ice saturation
1	6	0.2
2	2	0.5
3	4	0.7
4	4	0.8
5	–	1

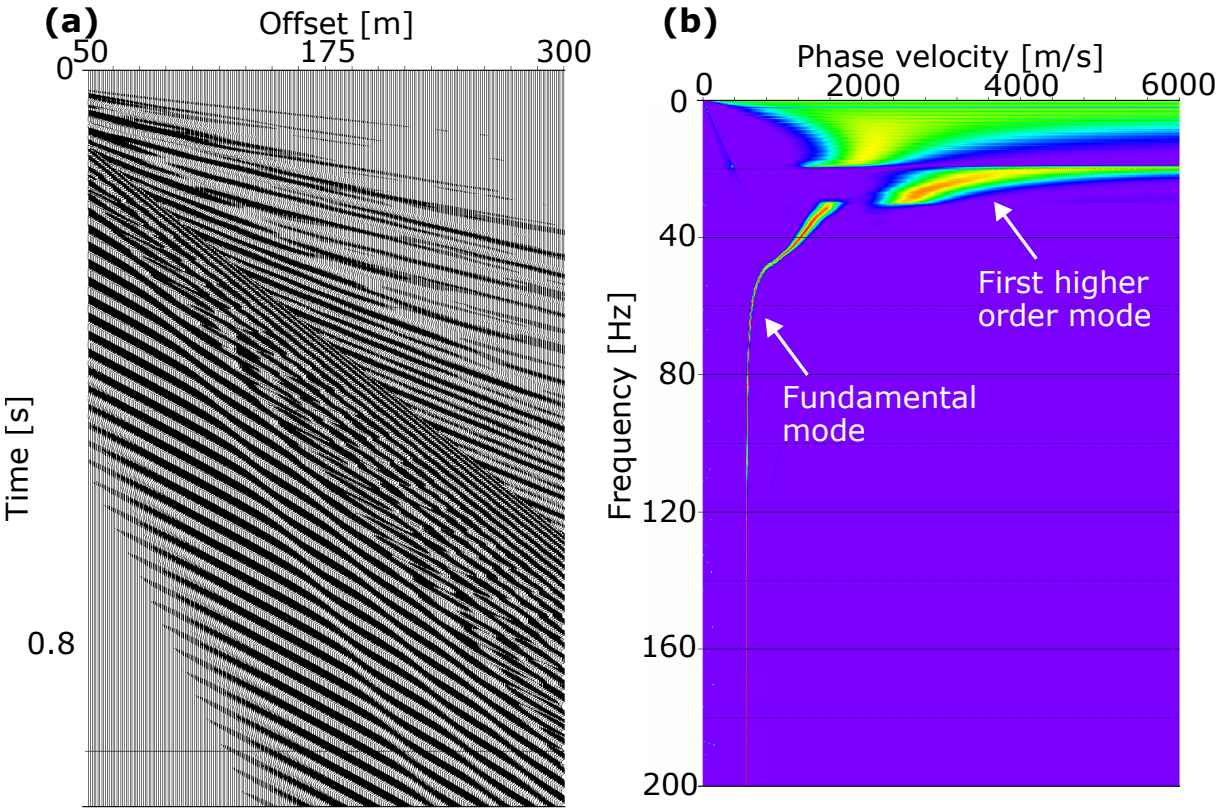

Figure 5.13: Seismic data for LM1a with seismic velocities based on rock physics model 2. (a) The seismic gather and (b) the corresponding dispersion image are presented.

The residual between LM1a (Figures 5.13 (a) and (b)) and LM1-U6 with seismic velocities based on rock physics model 2 (Figures 5.12 (c) and (f)), is shown in Figure 5.14. The seismic data show highly dispersive waves, and signs of several higher order modes are presented in the dispersion image. This indicates that there may be several higher order modes for the case with the previous models, but they are difficult to identify in the data presented.

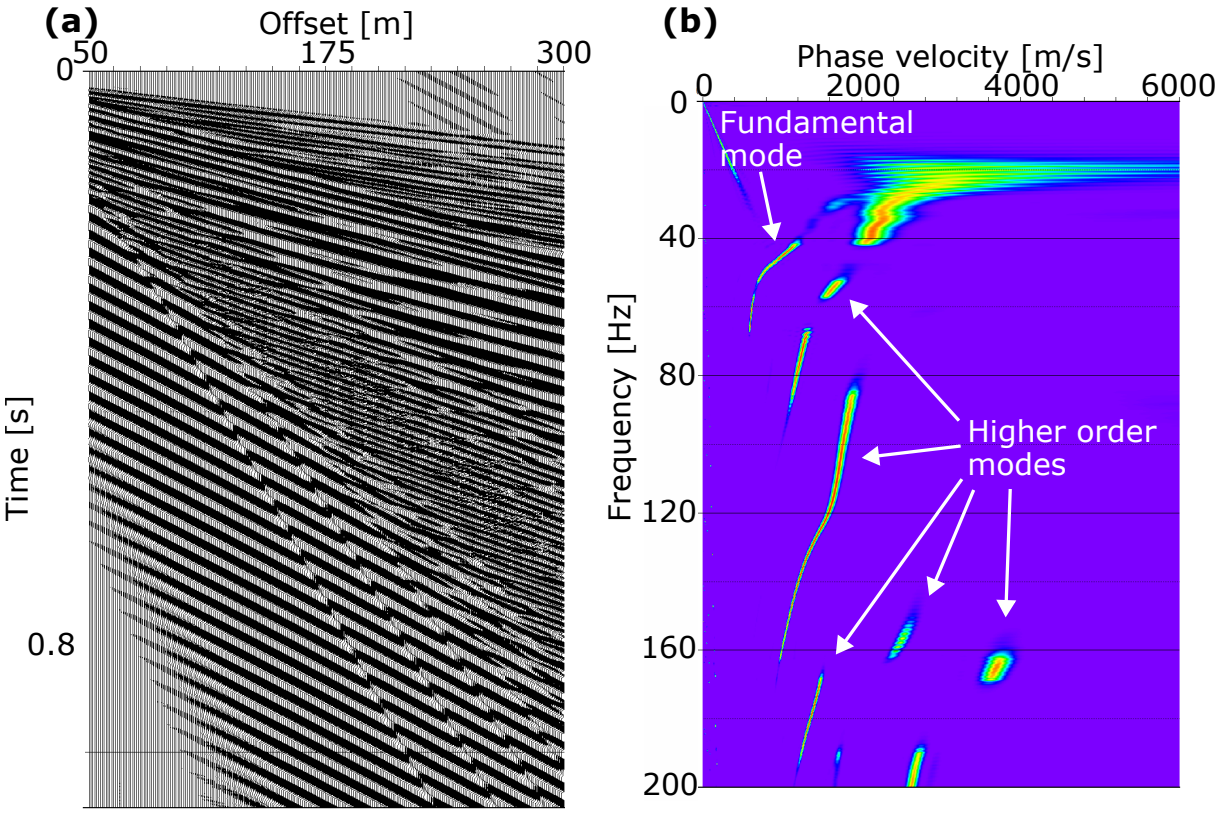

Figure 5.14: Residual between LM1a and LM1-U6 with seismic velocities based on rock physics model 2. (a) The seismic gather and (b) the corresponding dispersion image are shown and indicate several higher order modes for such models.

Small changes in thickness affect the dispersion curves, and the seismic data shown in Figure 5.15 also illustrate that. Figures (a) and (d) show the same results as for the first layer model with a uniform layer thickness of 4 m (LM1-U4), with seismic velocities based on rock physics model 2. Figures (b) and (e), and figures (c) and (f) show the results for small changes in thicknesses, LM1b and LM1c, respectively, which the model parameters are provided in Table 5.4.

Table 5.4: 5-layered 2D models: LM1b and LM1c.

Layer	Thickness [m]		Ice saturation
	LM1b	LM1c	
1	3	4	0.2
2	5	3	0.5
3	4	5	0.7
4	4	4	0.8
5	–	–	1

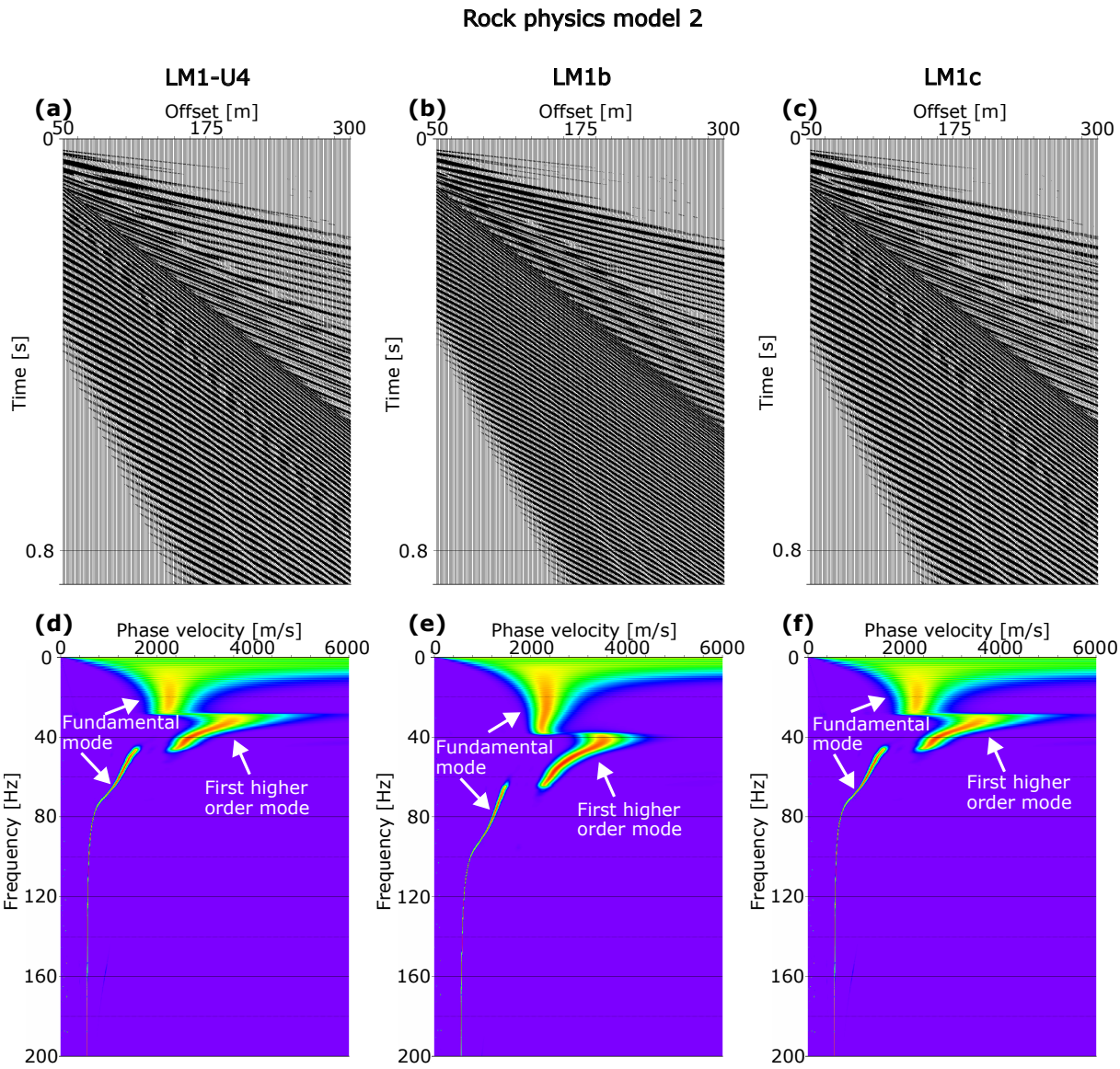

Figure 5.15: Top row: synthetic seismic gathers for (a) LM1-U4, (b) LM1b, and (c) LM1c. Bottom row: corresponding dispersion images for (d) LM1-U4, (e) LM1b, and (f) LM1c. The seismic velocities are based on rock physics model 2.

For the second case (LM1b), when the upper layer is 3 m thick, the first higher order mode appears at a higher frequency than for the other cases. The other two cases (LM1c and LM1-U4 based on rock physics model 2) are quite similar, and the residual between them is shown in Figure 5.16. Despite the fact that the amplitudes can not be compared between the two dispersion images, the residual shows that there are some energy differences, and a possible second higher order mode is visible, which it is not in the previous plots (Figures 5.15 (d) and (f)). That expresses the complications with interpreting the different higher order modes in such models. The results from this figure (Figure 5.16) and the previous ones (Figures 5.14 and Figure 5.15) indicate that small vertical changes

in velocity can result in discernible changes in the seismic data when the layers have specific thicknesses. The figures also indicate that when an intersection deeper in the ground changes, the changes in the dispersion of surface waves are not as significant as if the change happens at a shallower dept.

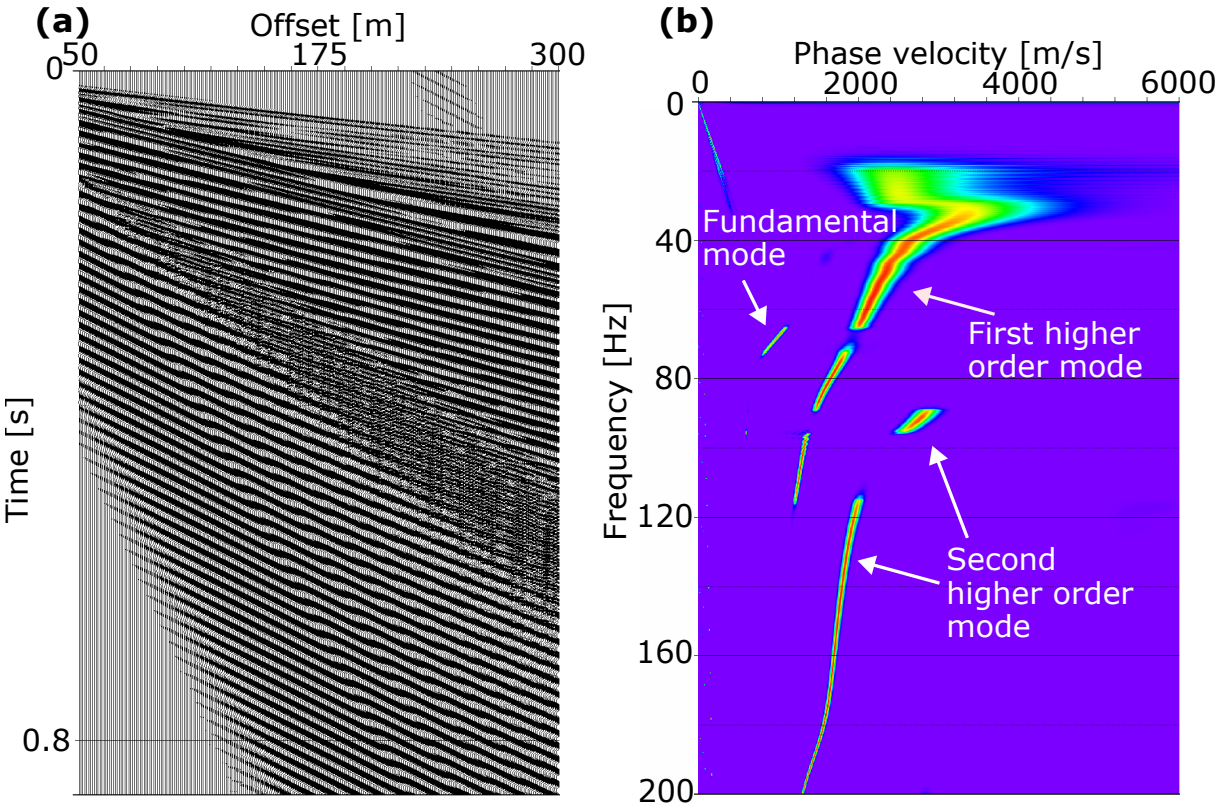

Figure 5.16: Residual between LM1-U4 and LM1c with seismic velocities based on rock physics model 2. (a) The synthetic seismic gather and (b) the corresponding dispersion image are presented.

In addition to the subsurface properties, the survey setup impacts the resulting seismic data. Figure 5.17 shows results from LM1-U4 (based on rock physics model 2) with the same maximum offset (300 m) but for varying receiver number and spacing. In figures (a) and (d), when the receiver interval is 1 m, and the receiver number is 300, there are no signs of aliasing, and represent the same figures as shown before (Figures 5.12 (b) and (e)). For the cases when the receiver interval is 5 m and 10 m, with 60 and 30 receivers, respectively, both the seismic gathers and the dispersion images show signs of aliasing. In the seismic data, the surface waves have a moveout similar to an anticline, which are signs of aliasing (Steeples and Miller, 1998). When the interval is 5 m, aliasing can be observed in the dispersion image for frequencies higher than ∼120 Hz. When the receiver

interval is 10 m, aliasing can be seen for frequencies above ∼75 Hz. For the last case, some numerical artifacts are also visible for frequencies below ∼40 Hz.

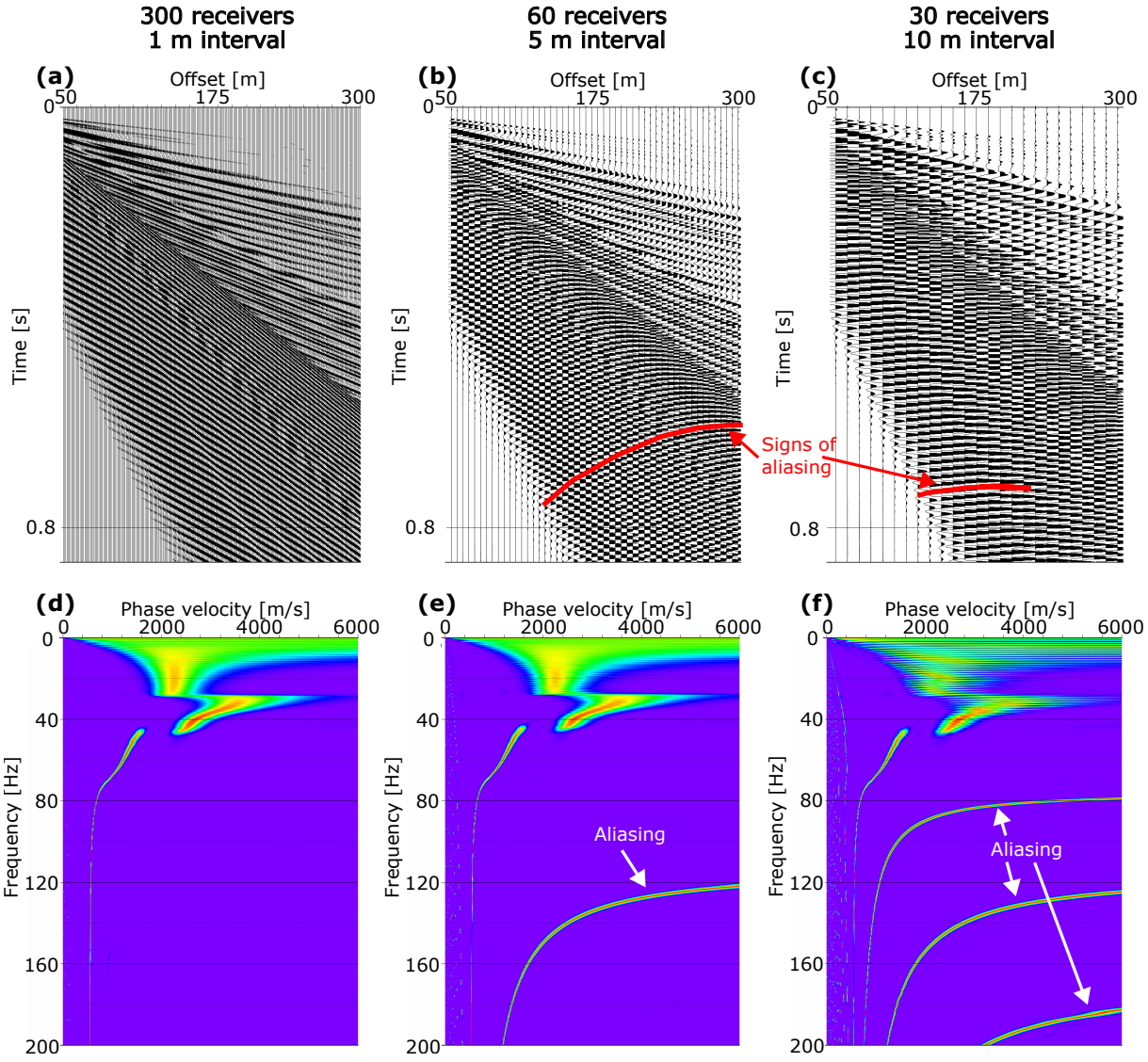

Figure 5.17: Top row: synthetic seismic gathers for LM1-U4 (based on rock physics model 2) with varying receiver interval and number of receivers. The receiver interval is (a) 1 m with 300 receivers, (b) 5 m with 60 receivers, and (c) 10 m with 30 receivers. Bottom row: corresponding dispersion images when the receiver interval is (d) 1 m with 300 receivers, (e) 5 m with 60 receivers, and (f) 10 m with 30 receivers.

In permafrost environments, the active layer, which is on top of the permanently frozen ground, may today typically be of 0.5 m to 2.5 m (Christiansen et al., 2010), but this will likely increase in the future due to surface warming. A simple simulation of how the dispersion image may change for a two-layered model, when the top layer's thickness increases, is performed, and the results are shown in Figure 5.18. This experimental scenario is performed for a subsurface model where an unfrozen top layer is increasing from 1 m to

1.5 m and further to 2 m. The second layer is frozen. Velocity values from rock physics model 2 are used, and the difference in velocity for the two layers defined is around 2500 m/s for both the P- and S-wave velocities. The first higher order mode clearly changes its energy from higher frequency ranges to lower frequency ranges in the dispersion images when the unfrozen top layer increases its thickness, i.e., reaching a lower depth.

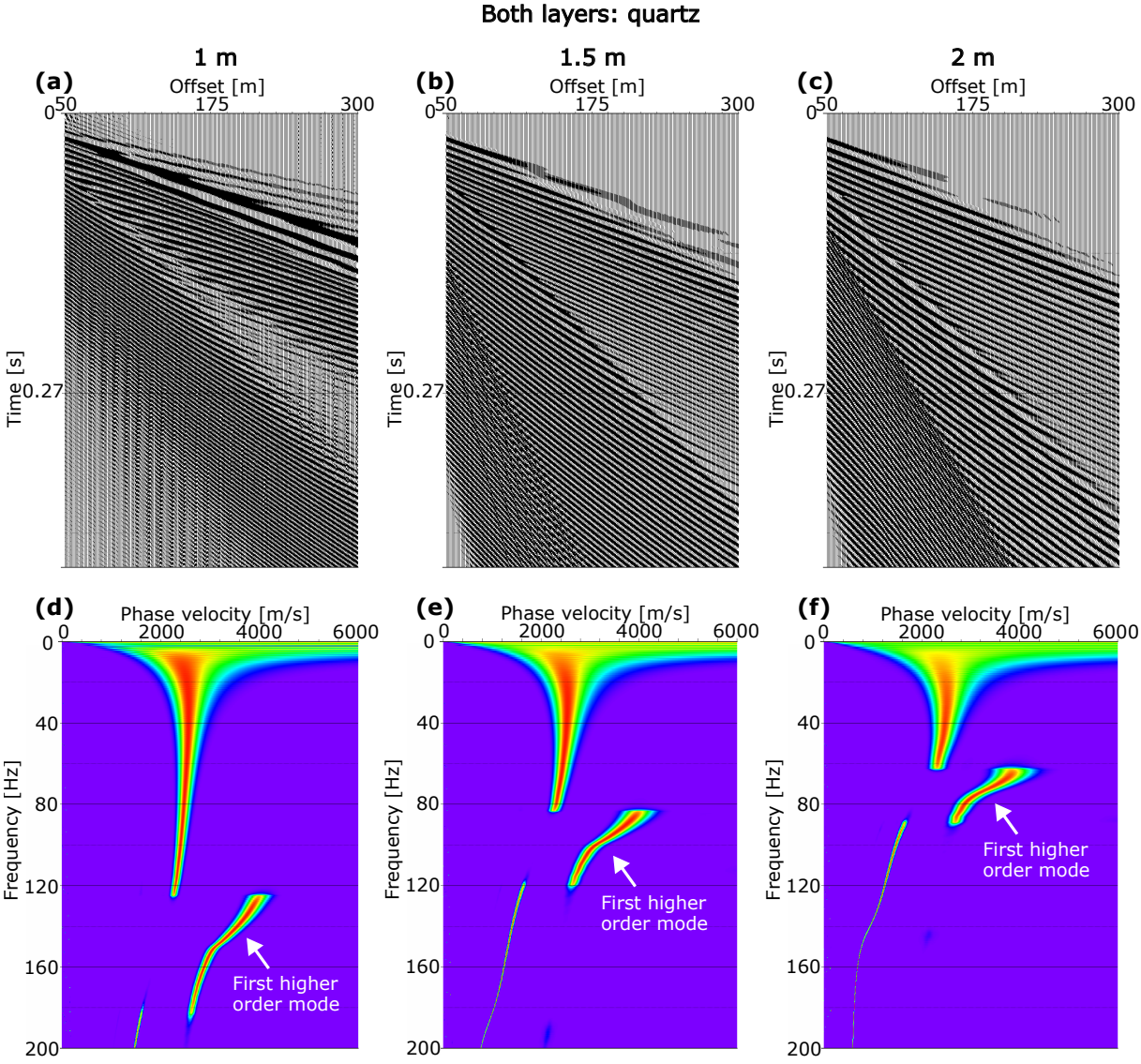

Figure 5.18: Top row: synthetic seismic gathers for (a) 1 m, (b) 1.5 m, and (c) 2 m unfrozen layer of quartz on top of a frozen layer of quartz. Bottom row: corresponding dispersion images for (c) 1 m, (b) 1.5 m, and (c) 2 m unfrozen layer of quartz on top of a frozen layer of quartz.

Since the sand type varies in real subsurface, a test is performed for layered subsurface with both quartz and feldspar. Figure 5.19 shows results for the same models used as for Figure 5.18, but the upper unfrozen layers consist of feldspar, and the upper layers are

therefore significantly softer with lower velocities. The layer below consists of only quartz. The energy of the first higher order mode appears at higher frequencies when the upper layer is softer (i.e., the difference between the top layer and the layer below is increasing).

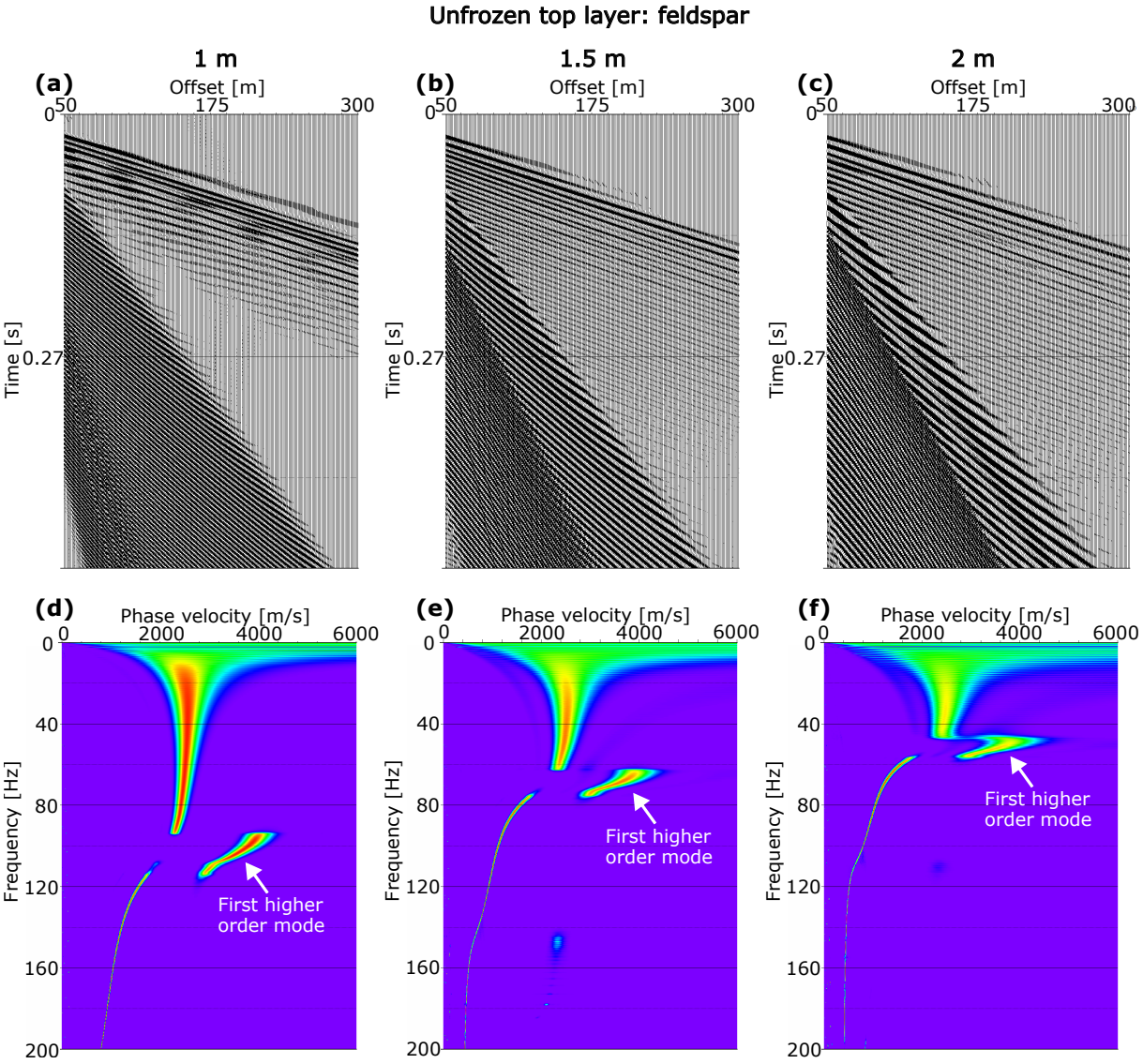

Figure 5.19: Top row: synthetic seismic gathers for (a) 1 m, (b) 1.5 m, and (c) 2 m unfrozen feldspar layer on top of a frozen quartz layer. Bottom row: corresponding dispersion images for (c) 1 m, (b) 1.5 m, and (c) 2 m unfrozen feldspar layer on top of a frozen quartz layer.

The active layer freezes during winter seasons. An example of how a partly frozen (0.5 ice saturation) layer above a frozen layer may be reflected in seismic data is shown in Figure 5.20. The seismic velocities are based on rock physics model 2, and only quartz is used for the sand properties. The seismic modeling results for a 1 m thick partly frozen layer on top of frozen subsurface are shown in Figures 5.20 (a) and (d), and the results for a 2

m thick partly frozen top layer are shown in Figures 5.20 (b) and (e). The seismic gathers and the dispersion images are quite similar for these two cases, and they do not show any significant signs of dispersion. The reason for no dispersion could be related to a very little change in the velocity between the partly frozen layer above the interface and the frozen layer below (∼0.9 m/s in difference for P-wave velocity, and ∼0.7 m/s for S-wave velocity). The residual between the seismic data when the partly frozen layer is 1 m and when it is 2 m is also presented (Figures 5.20 (c) and (f)) and shows that it is a change in energy for the fundamental mode.

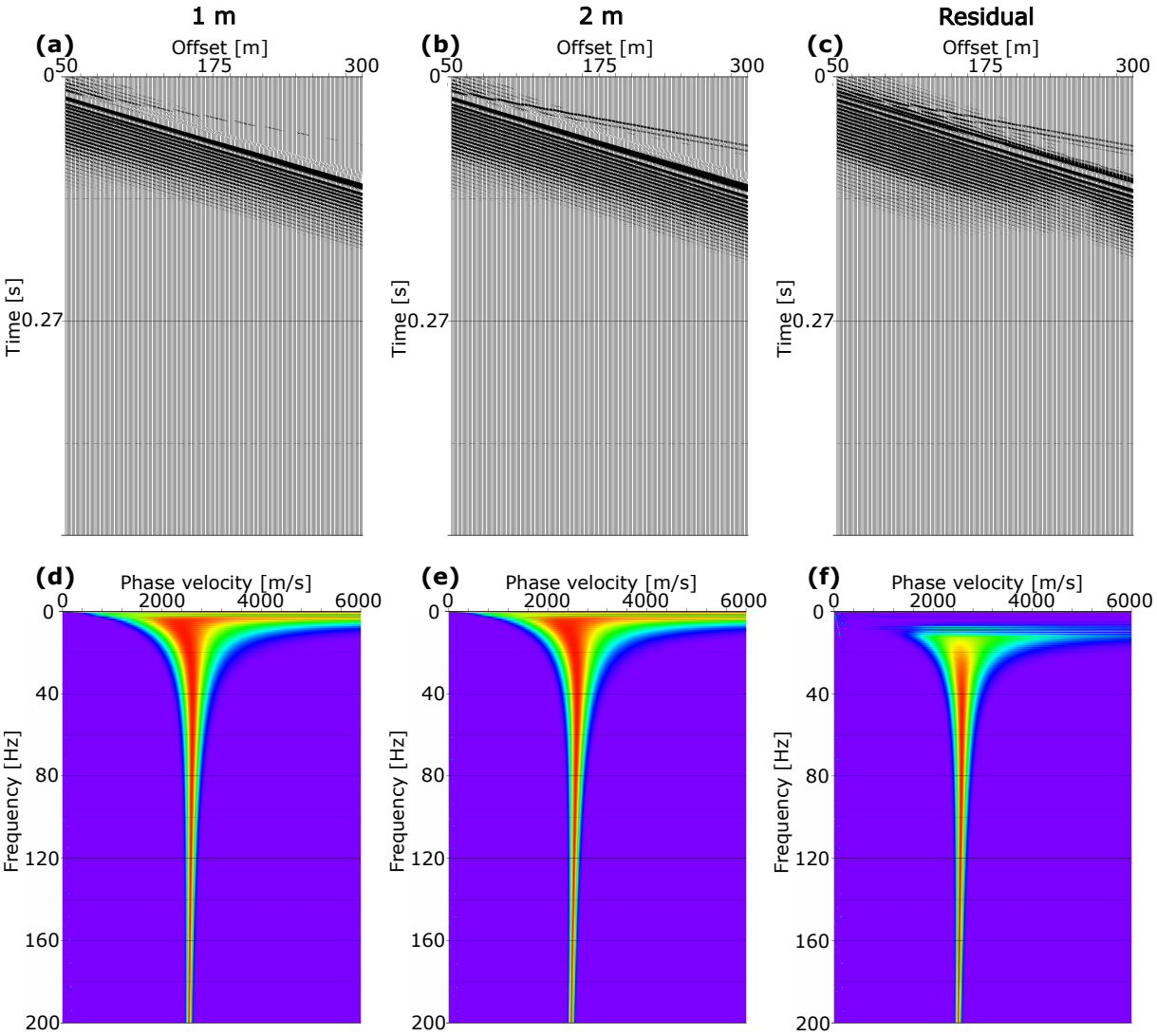

Figure 5.20: Top row: synthetic seismic gathers for a (a) 1 m and (b) 2 m partly frozen top layer above a frozen layer, and (c) the residual between them. Bottom row: corresponding dispersion images for a (d) 1 m and (e) 2 m partly frozen top layer above a frozen layer, and (f) the residual between them.

Figure 5.21 shows how the seismic data are affected by gradually increasing the ice saturation in the upper top layer. That could be the case for gradually decreasing salinity in the pore water. Results for a top layer with ice saturation equal to 0, 0.2, 0.4, and 0.5 are shown where the seismic velocities are based on rock physics model 2. The layer below is frozen. The plots have no significant differences, except when comparing the case with 0.5 ice saturation to the others. The case with 0.5 ice saturation shows no signs of dispersion. That is due to the "jump" to higher elastic moduli after 0.4 ice saturation and the relatively stable low elastic moduli before 0.4 ice saturation for this rock physics model (see Figure 5.4).

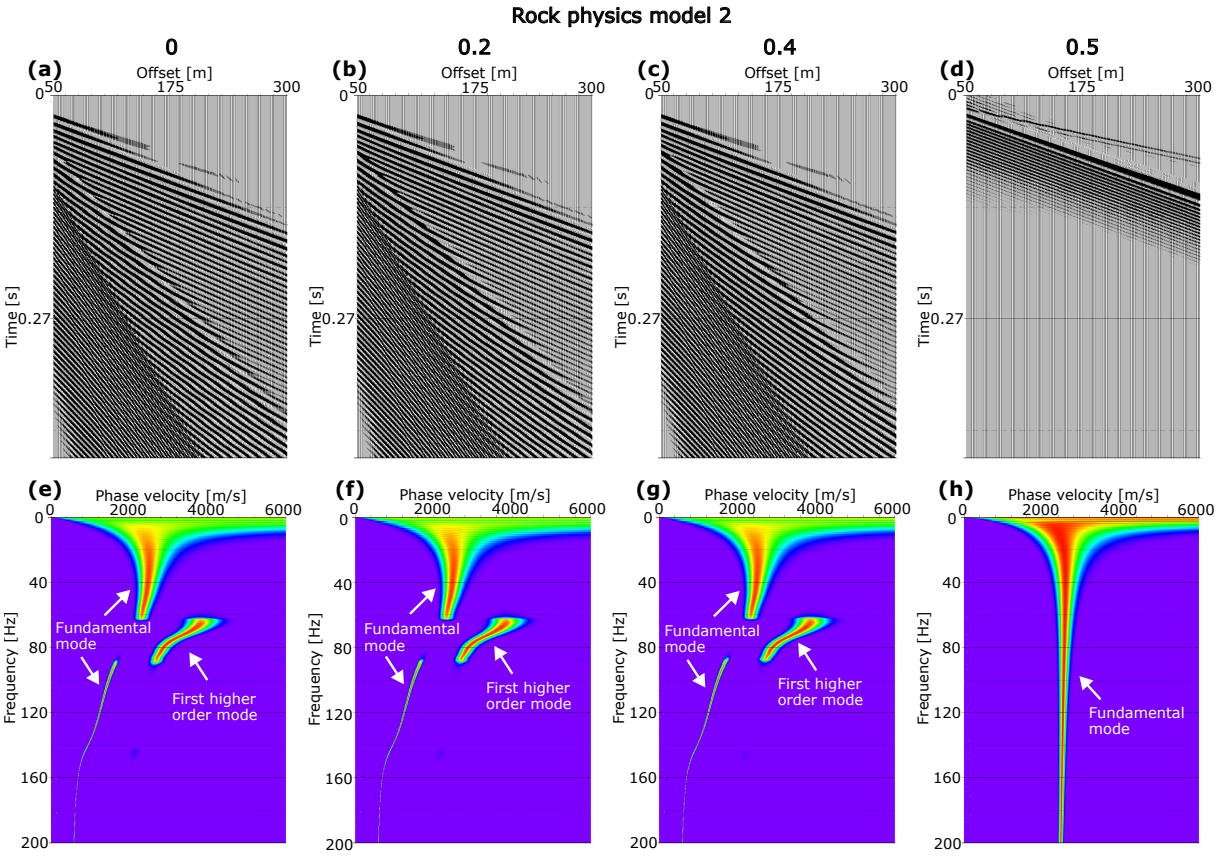

Figure 5.21: Top row: synthetic seismic gathers for a 2 m thick top layer above a frozen layer. The ice saturation is (a) 0, (b) 0.2, (c) 0.4, and (d) 0.5 for the top layer. Bottom row: corresponding dispersion images with ice saturation given as (e) 0, (f) 0.2, (g) 0.4, and (h) 0.5. The seismic velocities are based on rock physics model 2.

Figure 5.22 shows the two cases again when the ice saturation is 0 and 0.4 in the top layer, but together with the residual between them. The two first dispersion images (Figures 5.22 (d) and (e)) look similar, but the residual shows amplitude differences.

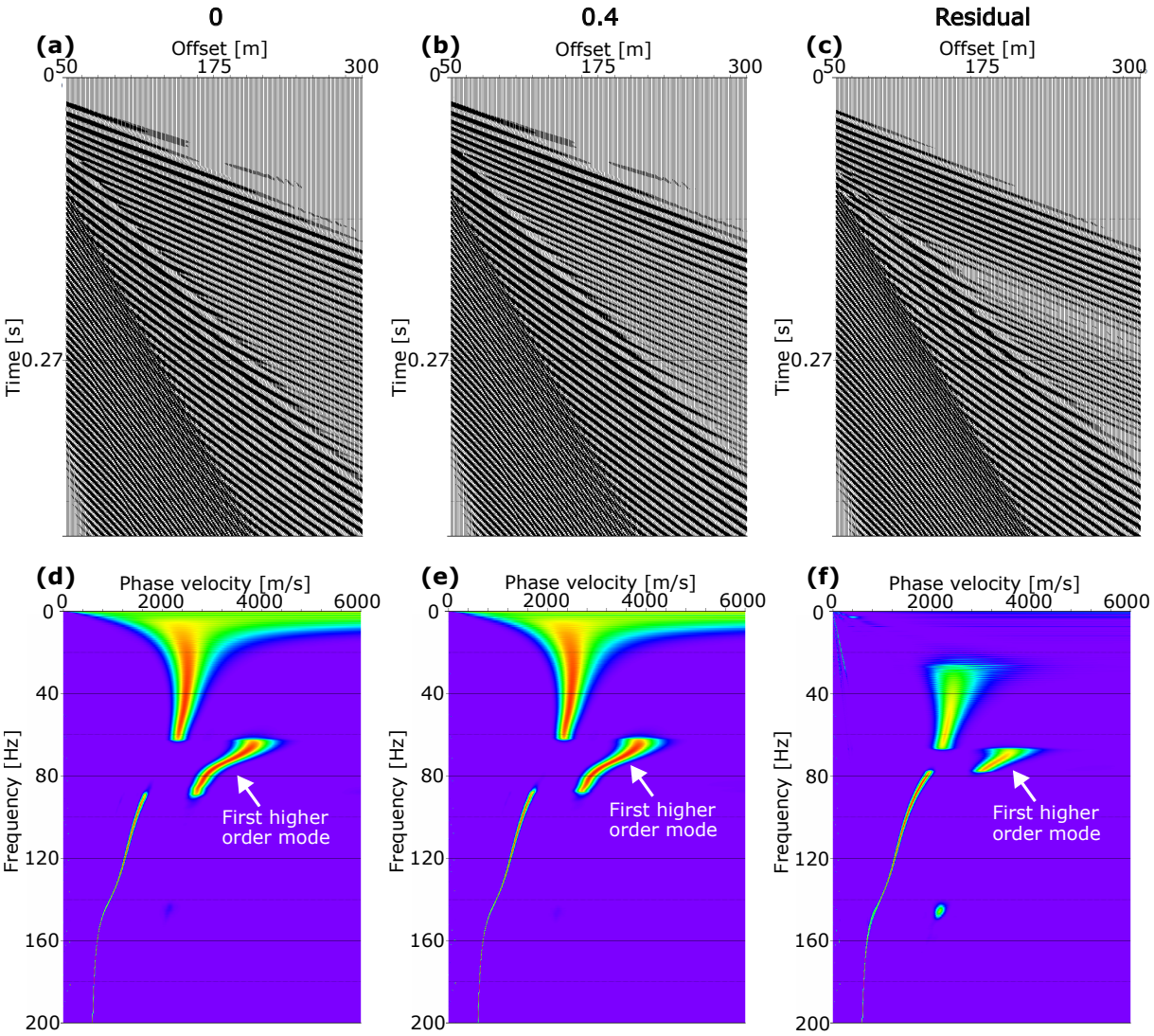

Figure 5.22: Top row: synthetic seismic gathers for a 2 m thick top layer above a frozen layer. The ice saturation is (a) 0 and (b) 0.4 for the top layer, and (c) the residual between them is presented. Bottom row: corresponding dispersion images with ice saturation given as (d) 0 and (e) 0.4, together with (f) the residual between them. The seismic velocities are based on rock physics model 2.

The same simulation, with a changing ice saturation of the top layer, is done based on rock physics model 1. That is shown in Figure 5.23. In this case, the figures have more significant differences due to a gradually increasing velocity of the top layer, corresponding to the seismic velocities from rock physics model 1.

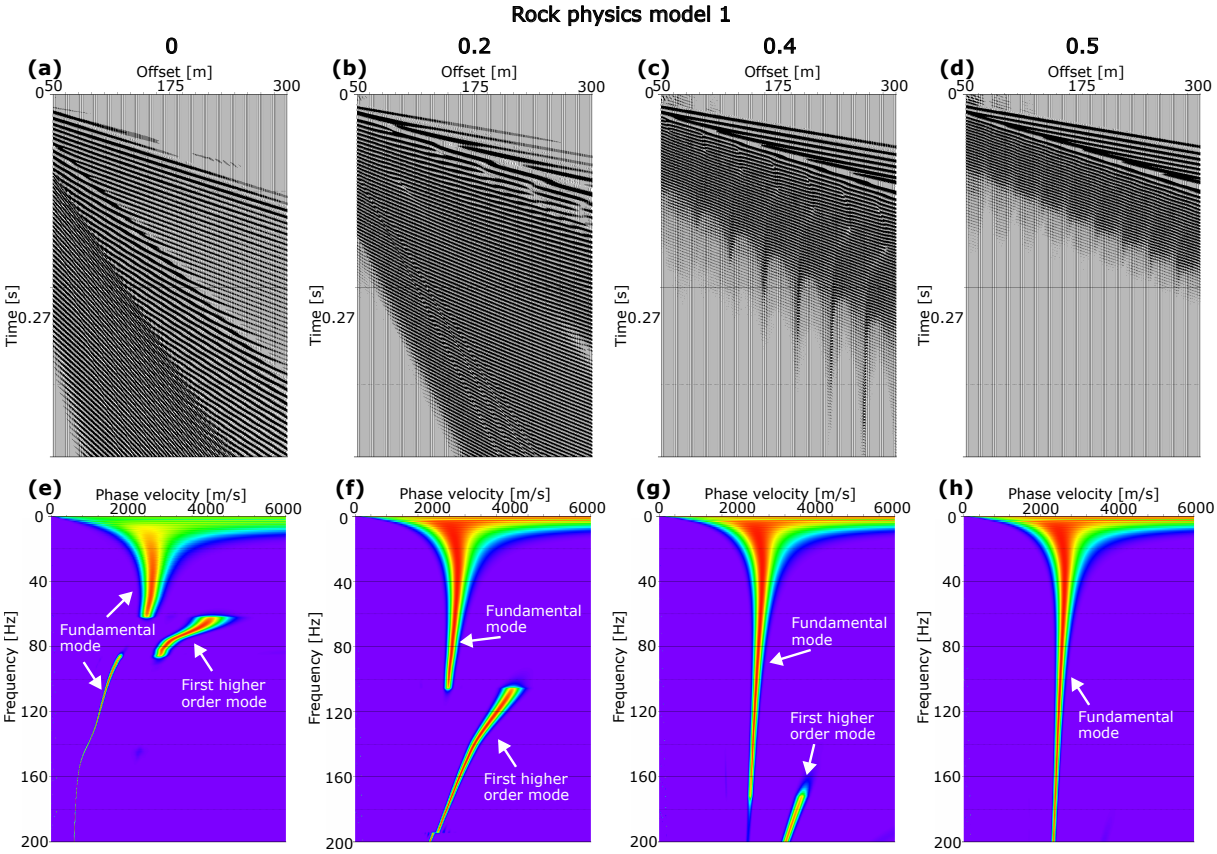

Figure 5.23: Top row: synthetic seismic gathers for a 2 m thick layer on top of a frozen layer. The ice saturation is (a) 0, (b) 0.2, (c) 0.4, and (d) 0.5 for the top layer. Bottom row: corresponding dispersion images with ice saturation given as (e) 0, (f) 0.2, (g) 0.4, and (h) 0.5. The seismic velocities are based on rock physics model 1.

5.2.2 Decreasing ice saturation with depth

If the sand properties of the subsurface are vertically equal, but the ice saturation decreases with depth, the velocities also decrease with depth. That may be the case if the salinity in the near-surface increases with depth or the upper layers of a subsurface are frozen due to cold surface temperatures. The properties of a second 5-layered 2D model (LM2) are provided in Table 5.5. Figures 5.24 (a) and (d) show synthetic seismic gather and its corresponding dispersion image for LM2. Figures 5.24 (b) and (e) show the results for a similar model, but with a uniform layer thickness of 4 m (LM2-U4), and Figures 5.24 (c) and (f) show the results for the same model with a uniform layer thickness of 6 m (LM2-U6).

Table 5.5: 5-layered 2D models: LM2, LM2-U4, and LM2-U6.

Layer	Thickness [m]			Ice saturation
	LM2	LM2-U4	LM2-U6	
1	0.5	4	6	1
2	1	4	6	0.9
3	1.5	4	6	0.7
4	7	4	6	0.1
5	–	–	–	0

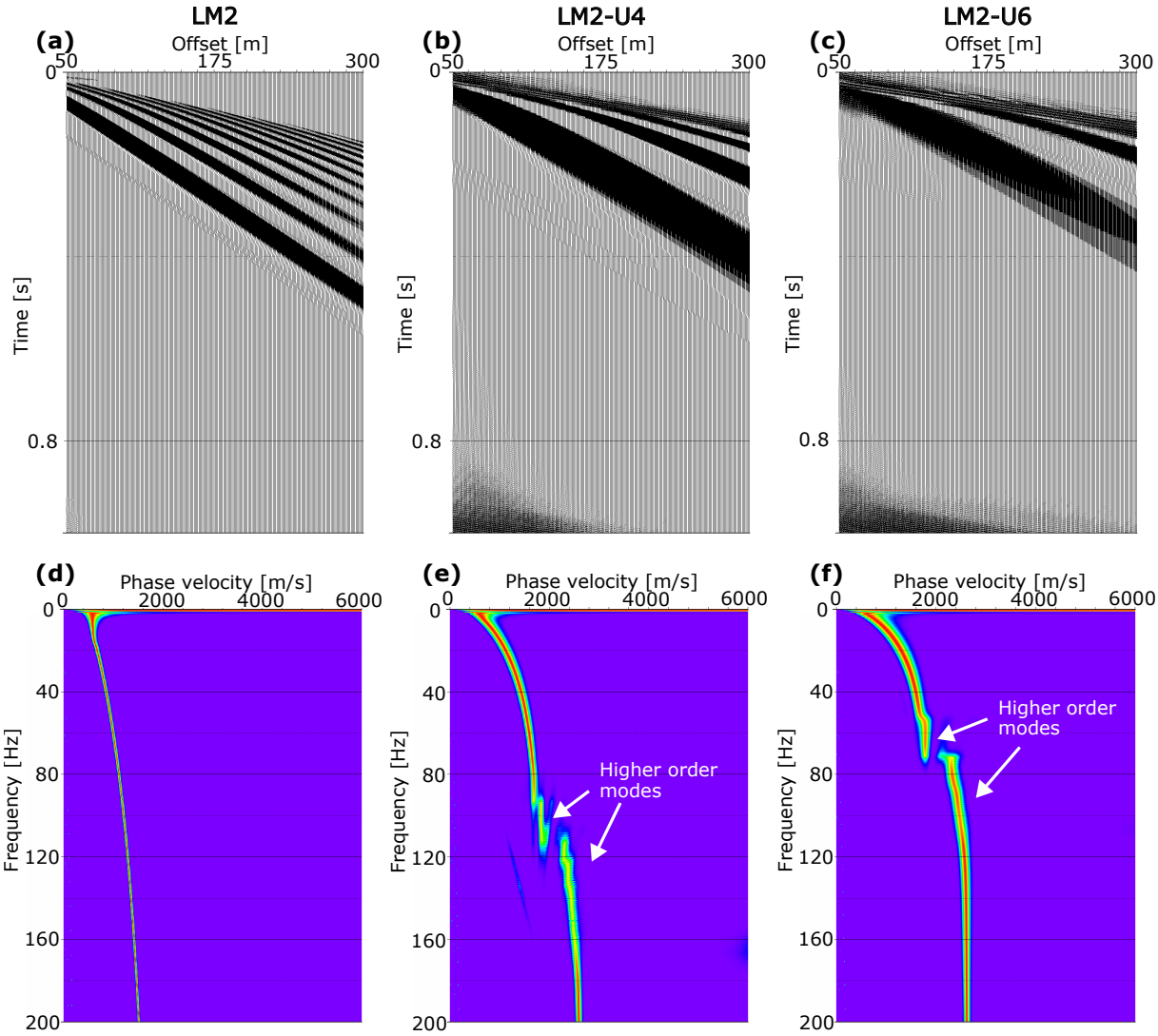

Figure 5.24: Top row: synthetic seismic gathers for (a) LM2, (b) LM2-U4, and (c) LM2-U6. Bottom row: corresponding dispersion images for (d) LM2, (e) LM2-U4, and (f) LM2-U6. The seismic velocities are based on rock physics model 2.

Lower frequencies show amplitudes for lower phase velocities. As the frequencies increase, the velocities also increase. That is different from the dispersion images from the previous section (Chapter 5.2.1). Figures 5.24 (e) and (f) show signs of multiple modes. The higher

order modes appear at lower frequencies for the model with a uniform thickness of 6 m. For the case in the dispersion image for LM2, it looks like only one mode is present.

Figure 5.25 shows a scenario for a two-layered model, where the ground is frozen above the interface between the layers and unfrozen below the interface. It shows three cases where the top layer is 1 m thick, 1.5 m thick, and 2 m thick. The dispersion curve is narrower in this case, and no significant signs of several modes are indicated. However, the dispersion curves bend towards higher velocities for higher frequencies as for the previous case (Figure 5.24).

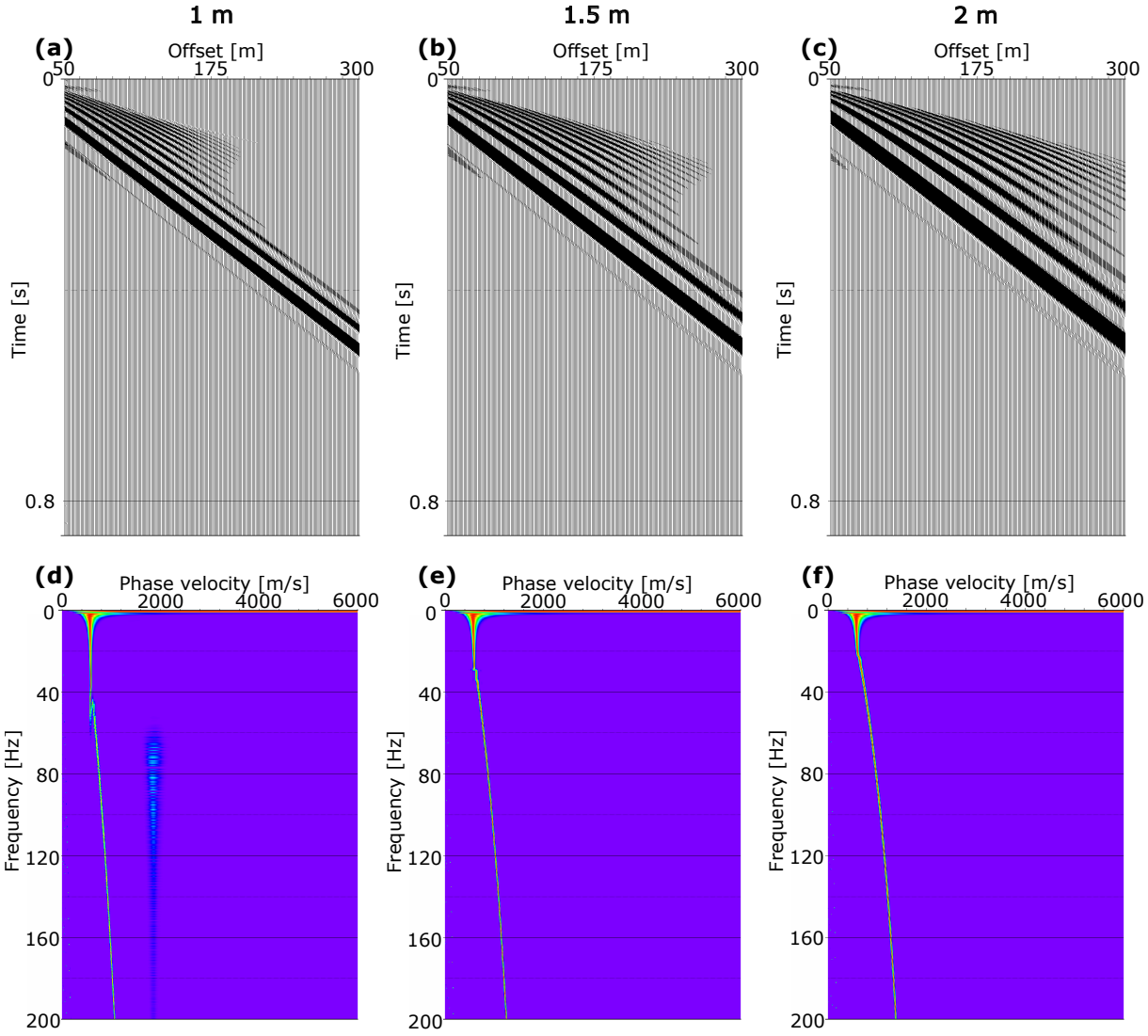

Figure 5.25: Synthetic seismic data for a two-layered model consisting of a frozen top layer, with varying thickness, and an unfrozen layer below. Top row: synthetic seismic gathers when the top layer is (a) 1 m, (b) 1.5 m, and (c) 2 m thick. Bottom row: corresponding dispersion images when the top layer is (d) 1 m, (e) 1.5 m, and (f) 2 m thick. The seismic velocities are based on rock physics model 2.

5.2.3 Unfrozen and partly unfrozen layers embedded in frozen ground

Sometimes, the salinity varies, having an irregular gradient with depth, and sometimes, an unfrozen active layer above frozen permafrost starts to freeze at the surface due to colder surface temperatures (e.g., in autumn). In these cases, unfrozen and partly frozen layers may be embedded in frozen ground. A third 5-layered 2D model (LM3) is described in Table 5.6, representing one such scenario. Figure 5.26 shows the resulting synthetic seismic gathers and their corresponding dispersion images for LM3, LM3 with a uniform thickness of 4 m (LM3-U4), and LM3 with a uniform layer thickness of 6 m (LM3-U6), with seismic velocities based on rock physics model 1. The seismic data show a wide range of seismic waves for all three cases, but the modes in the dispersion images are not possible to separate for the first case (LM3) when the velocity changes are only happening at the very top of the model. The results show clearly that the dispersive energy "jumps" from the fundamental mode to higher modes, and each mode lacks energy at different frequencies. The energy "jumps" from lower phase velocities to higher phase velocities with increasing frequencies. When the thickness of each layer is 6 m, the modes are displayed at lower frequencies than when the thickness is 4 m for each layer.

Table 5.6: 5-layered 2D models: LM3, LM3-U4, and LM3-U6.

Layer	Thickness [m]			Ice saturation
	LM3	LM3-U4	LM3-U6	
1	0.5	4	6	1
2	1	4	6	0.5
3	1.5	4	6	0
4	7	4	6	0.8
5	–	–	–	1

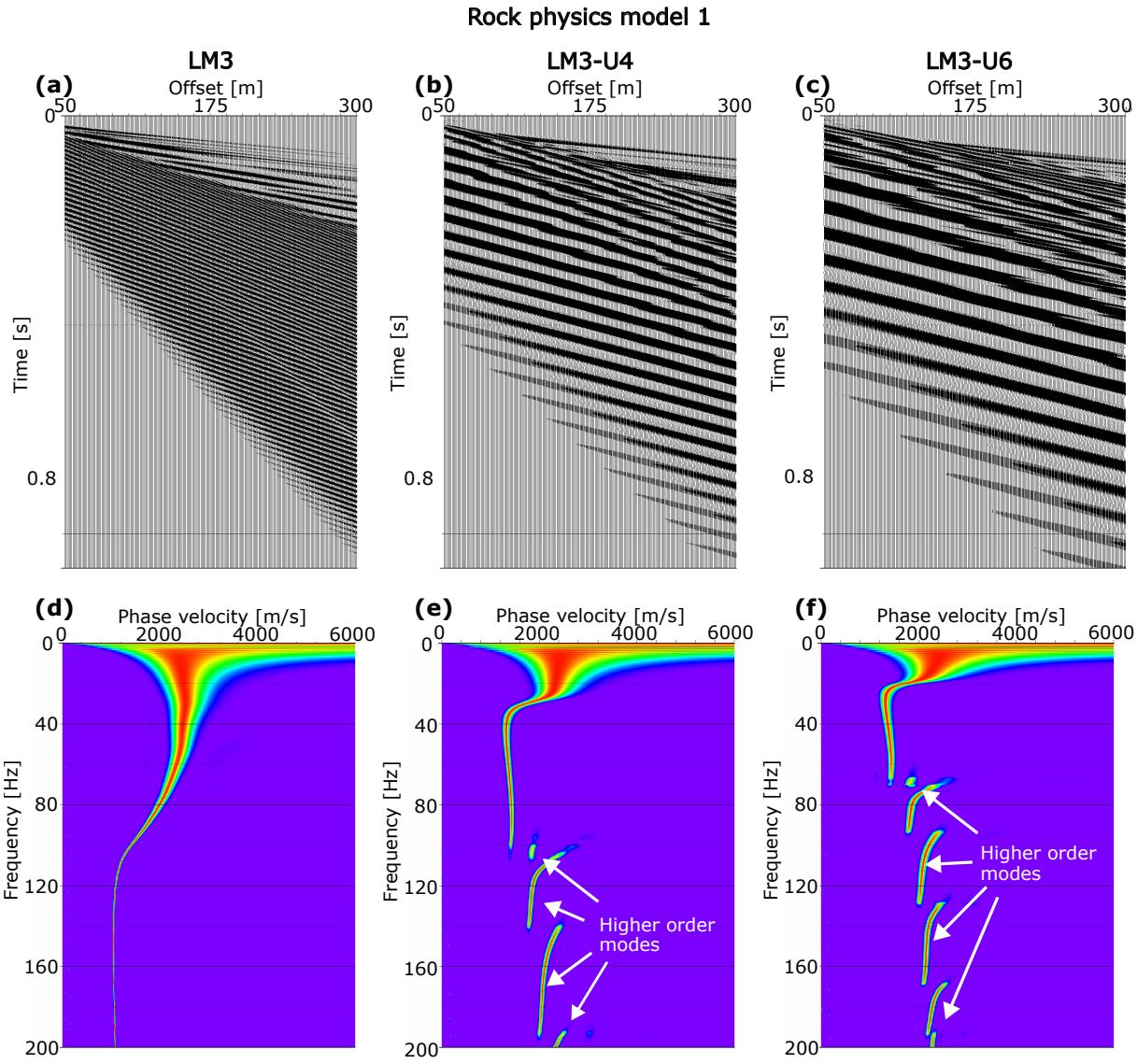

Figure 5.26: Top row: synthetic seismic gathers for (a) LM3, (b) LM3-U4, and (c) LM3-U6. Bottom row: corresponding dispersion images for (d) LM3, (e) LM3-U4, and (f) LM3-U6. The seismic velocities are based on rock physics model 1.

The same seismic modeling is done for LM3 when the velocities are based on rock physics model 2. That is shown in Figure 5.27. The higher order modes are clearly visible in LM3-U4 and LM3-U6, but the energy of each mode is present at slightly different frequencies than when the velocities are based on rock physics model 1.

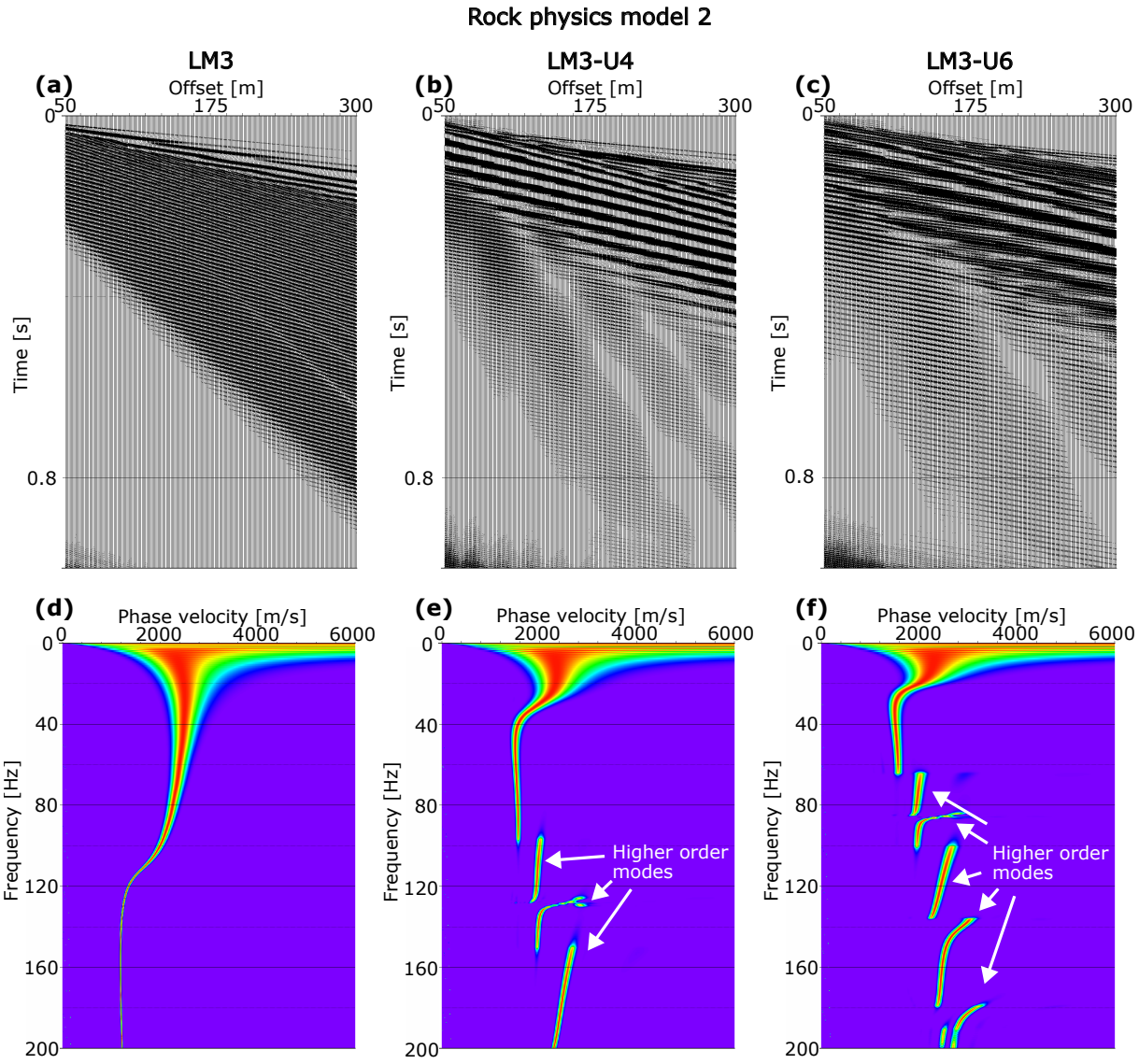

Figure 5.27: Top row: synthetic seismic gathers for (a) LM3, (b) LM3-U4, and (c) LM3-U6. Bottom row: corresponding dispersion images for (d) LM3, (e) LM3-U4, and (f) LM3-U6. The seismic velocities are based on rock physics model 2.

Another example of synthetic seismic data is shown in Figure 5.28. The figure illustrates a scenario where an initial 2 m thick unfrozen layer above a frozen layer starts to freeze from the top. The considered subsurface model consists of three layers where the interface between the top frozen layer and the second unfrozen layer changes depth for each case in the figure. The figure shows three scenarios where the thickness of the frozen top layer changes from 0.5 m to 1 m, and further to 1.5 m. The changing thickness of the high velocity layer on top impacts the resulting seismic data. The scenario where the top layer is 0.5 m shows very dispersive waves in the seismic gather. The surface waves are less dispersive for the scenario where the top layer is 1 m and very little for the last scenario where the top layer is 1.5 m. The unfrozen layer is thinner for the

two last cases, and the less dispersive waves may indicate that the unfrozen layer is too thin, concerning the wavelengths, to make the surface waves as dispersive as the first case.

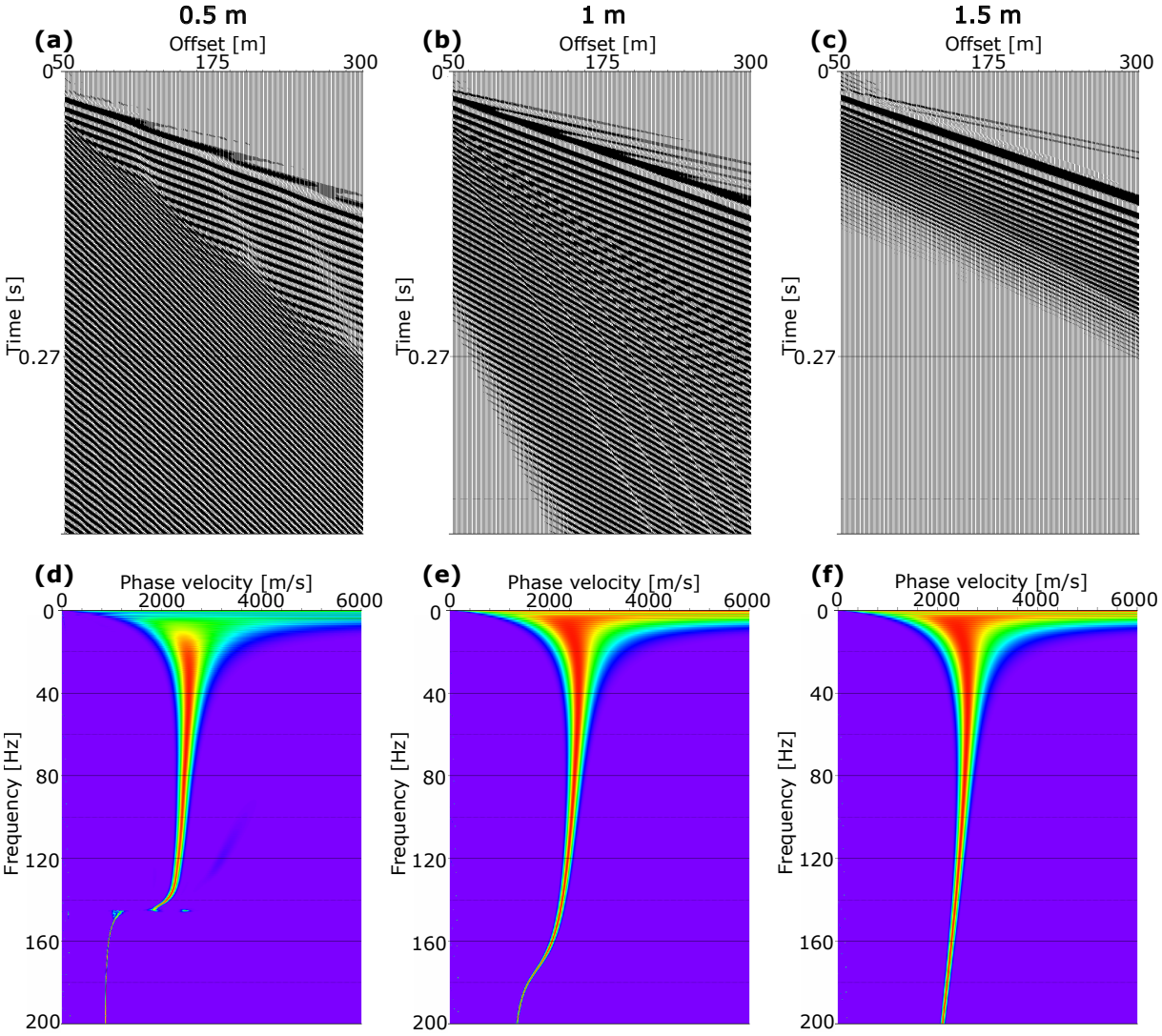

Figure 5.28: Synthetic seismic data for a three-layered model with a frozen top layer, an unfrozen second layer, and a frozen layer below. Top row: synthetic seismic gathers when the top frozen layer is (a) 0.5 m, (b) 1 m, and (c) 1.5 m. The third layer always starts at 2 m depth. Bottom row: corresponding dispersion images when the top layer is (d) 0.5 m, (e) 1 m, and (f) 1.5 m.

Three other 5-layered 2D models (LM4, LM5, and LM6) are made with slightly different layer thicknesses and ice saturation than LM3 and are shown in Table 5.7. Figure 5.29 shows the seismic data results of seismic modeling on these models when 300 receivers with a receiver interval of 1 m are used, and the seismic velocities are based on rock physics model 1. LM4 has a 1 m thicker top layer than LM5, and LM5 has a 1 m thinner fourth layer than LM6.

Table 5.7: 5-layered 2D models: LM4, LM5, and LM6

Layer	Thickness [m]			Ice saturation
	LM4	LM5	LM6	
1	2	1	1	1
2	3	4	4	0.5
3	3	3	3	0
4	8	8	9	0.5
5	–	–	–	1

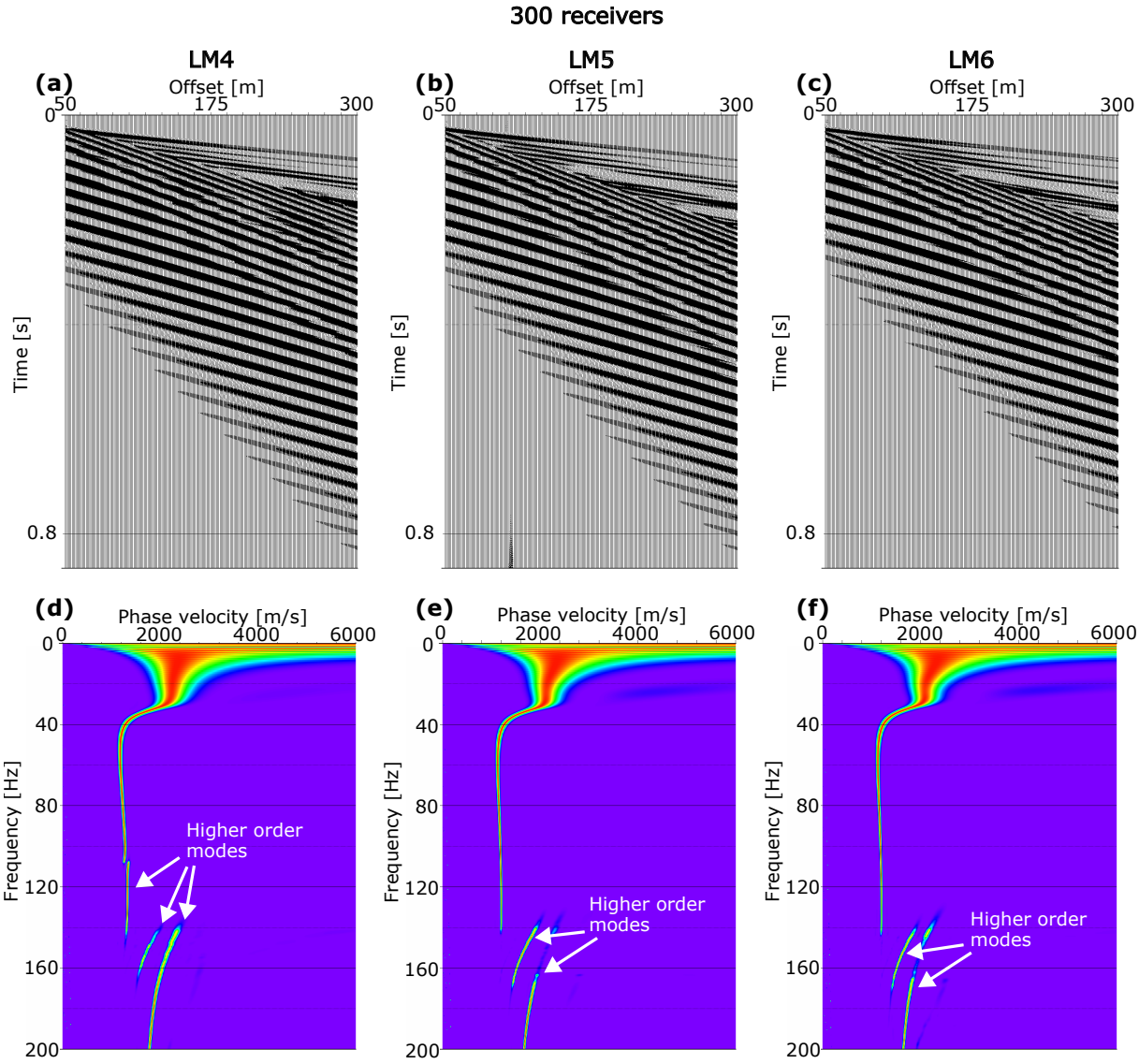

Figure 5.29: Top row: synthetic seismic gathers for (a) LM4, (b) LM5, and (c) LM6. Bottom row: corresponding dispersion images for (d) LM4, (e) LM5, and (f) LM6. The seismic velocities are based on rock physics model 1, and 300 receivers are used with a receiver interval of 1 m.

The seismic modeling is also performed with 100 receivers with a receiver interval of 1 m, which the results are shown in Figure 5.30. The seismic gathers show less dispersion

than in Figure 5.29, and the modes are more separated for the case with 300 receivers. A comparison of these figures indicates that an increased number of receivers over a larger area increases the resolution of the seismic data.

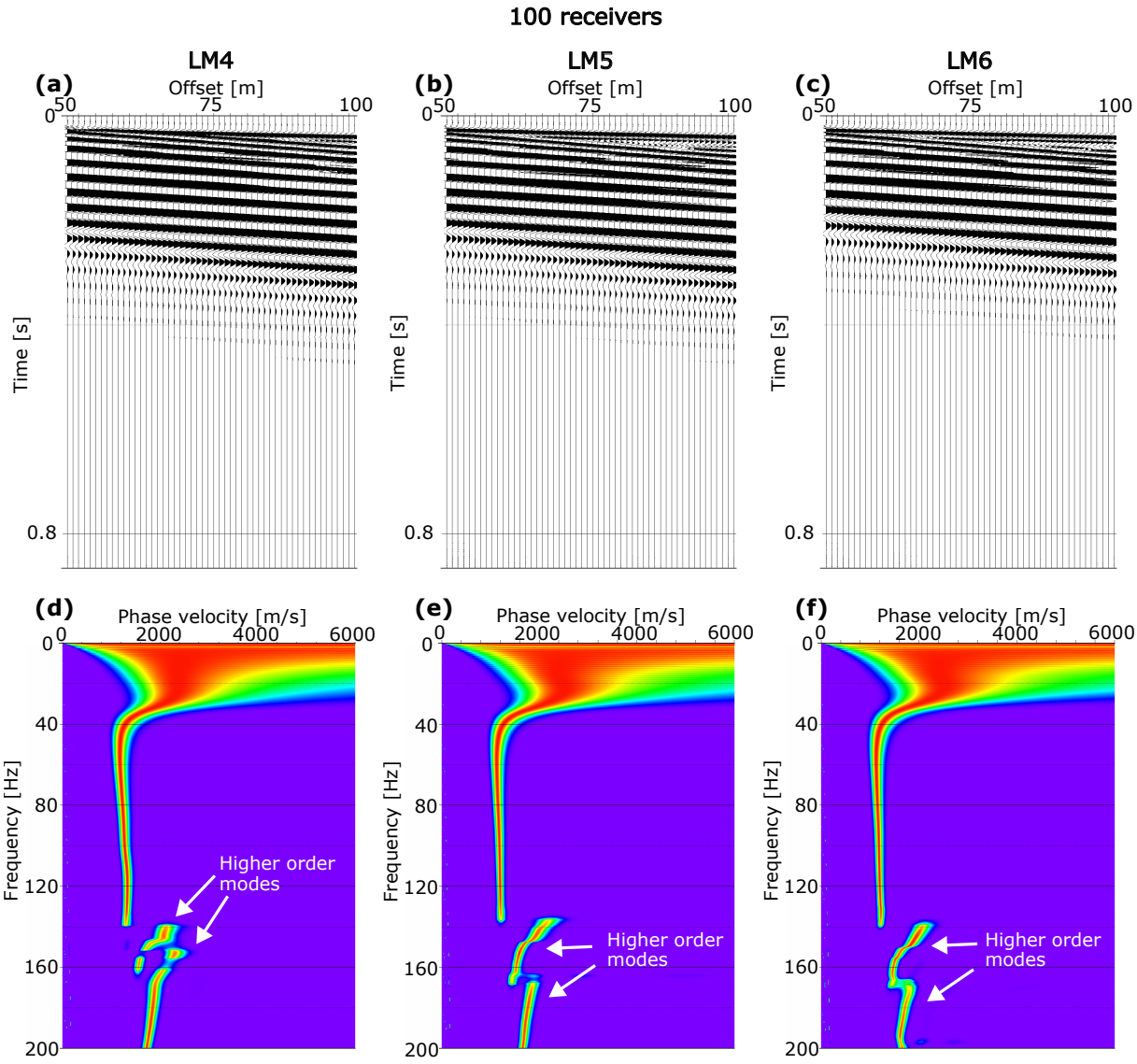

Figure 5.30: Top row: synthetic seismic gathers for (a) LM4, (b) LM5, and (c) LM6. Bottom row: corresponding dispersion images for (d) LM4, (e) LM5, and (f) LM6. The seismic velocities are based on rock physics model 1, and 100 receivers are used with a receiver interval of 1 m.

Chapter 6

Discussion

It has been shown in previous chapters that there are several ways to model seismic properties as functions of ice saturation, and the models provide various results. In this chapter, I discuss the modeling and results in relation to the theory and objective of this thesis. Some suggestions for further work are provided in the last section.

6.1 Evaluation of the modeling

The modeling in this thesis does not represent data from real subsurface, and the synthetic results therefore differ from real velocities from seismic data acquired in the field. However, synthetic results may improve the understanding of how to interpret real data.

6.1.1 Remarks - rock physics modeling

The modeled composite rocks used in the rock physics modeling are simple, consisting of only one or two minerals with equal grain size. The real Earth's subsurface usually consists of a mix of several mineral sizes (e.g., Gilbert et al., 2018), and this may result in varying porosity within the subsurface as well as other parameter variations. The results in Figures 5.7 and 5.10 show that variation in minerals and porosities impacts the seismic velocities. Therefore, seismic velocities of real sediments are expected to differ from the modeling in this thesis.

Spherical inclusion shapes are assumed for the ice fragments in the ice-water mixture used in rock physics model 2, which is based on ice cementation modeling, as assumed in Johansen et al. (2003). If penny-shape inclusions were assumed for rock physics model 2, which is the case for the models used by Dou et al. (2017) and Stemland et al. (2020b), the seismic velocities of the ice-water mixture would be different. The elastic moduli of the ice-water mixture as functions of ice saturation are shown in Figure 6.1 for both spherical and penny-shaped ice inclusions. The ice-water mixture in the pore space may have a critical point at an ice saturation equal to ∼0.82 instead of 0.4 (Figure 6.1), meaning that the mixture would act as a fluid until 82% of the mixture consists of ice.

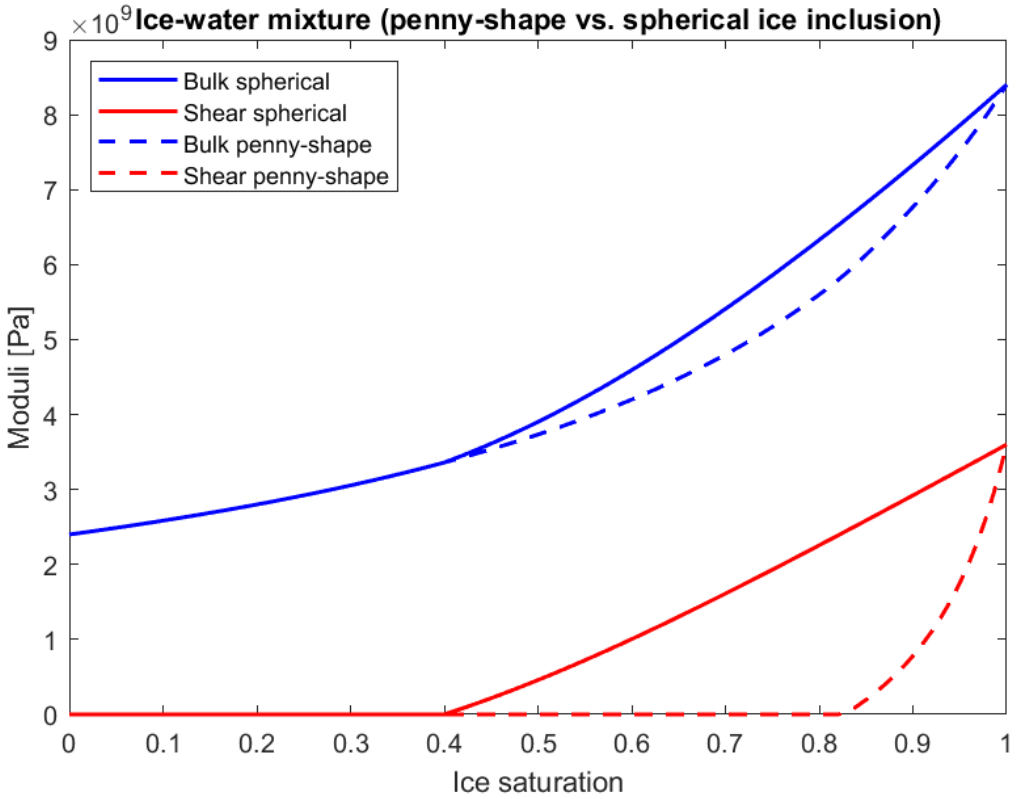

Figure 6.1: Elastic moduli of a mixture of ice and water as functions of ice saturation using the SCA. The results for both spherical and penny-shaped inclusion assumptions for the ice fragments are shown. The water inclusions are assumed spherical for both cases.

If the ice-water mixture with the penny-shape assumption was used in the modeling, the velocities of a saturated rock would differ from the resulting velocity models shown in Figures 5.5 and 5.10. The elastic moduli would probably show that the composite rock would be softer for even higher ice saturation since the critical shear modulus is present

at a higher ice saturation. The fact that small details, such as ice fragment shape, may impact the modeling to a certain degree is important to be aware of in analyses.

Real grains may not always be spherical, as it is assumed in the composite rocks in this thesis, and that may also make errors in the analysis as mentioned by Zimmerman and King (1986). However, Zimmerman and King (1986) also state that small amounts of elliptical inclusions should only affect the results slightly compared to only having spherical grain inclusions.

The rock physics models are not applicable for clay-rich sediments because of large variations in the elastic properties of clay minerals, strong surface effects, and its cementation behavior (Dou et al., 2016, 2017). Further, some clay particles are more disk-shaped than spherical (Zimmerman and King, 1986), and since the models used in this thesis always assume spherical grain shapes (Hertz-Mindlin equations in Chapter 3.3.1), the models would not be correct for clay. The velocity results for clay in Figure 5.10 (c) are therefore not reliable.

Numerical artifact in rock physics model 2

Rock physics model 2 had a numerical artifact close to the critical shear modulus point at ice saturation equal to 0.4 (Figure 5.5). The seismic velocities had unrealistic high values for ice saturation between $0.4 - 0.5$. The ice-water mixture should be softer with a softer cementation medium and with a softer pore-filling medium. However, high velocities were present for a medium with lower ice saturation in that interval. A smooth function in MATLAB (local regression) has therefore been used to smooth the velocity curves that are used for further calculations. This numerical artifact was also reported by Johansen et al. (2003), which the model is based on, and was solved in a similar way by those authors. Possible reasons for this artifact could be that there are some limitations of the use of S_n and S_τ in the cementation equations (Equations 3.24 and 3.25). When there is a high water percentage in the cement, and the cement properties show a lower shear modulus than bulk modulus, the equations are incorrect for the case in this thesis.

Variation in lithostatic pressure

The lithostatic pressure in the subsurface does change with depth, and the pressure, P, can be found by

$$P = \rho D g, \tag{6.1}$$

where ρ is the density, D is the depth, and g is the acceleration due to gravity.

The rock physics models do not consider depth-related pressure variations. For simplicity, the pressure used in the Hertz-Mindlin equations (Equations 3.12 and 3.13), which further impacts other rock physics equations, is assumed as a constant since the other parameters in the pressure equation (Equation 6.1) are assumed as constants. The depth value is assumed as a constant of 10 m. If it would change for each layer in the subsurface models, this pressure would increase with depth. The elastic moduli of the layers below 10 m depth would be of a higher value, resulting in higher velocities, and for the layers above 10 m, lower velocities than those produced in this thesis would be present. The density of the ground is assumed to be a constant of 2500 kg/m^3. It is therefore not changing with factors that may impact the density, such as porosity, pressure, and pore saturation. These assumptions may affect the rock physics models but may result in small changes, which may not be noticeable in the seismic data.

Ice morphology

The seismic velocities as functions of ice saturation depend on more than the amount of ice in a rock's pore space. Effective elastic properties of partially frozen sediments depend strongly on the ice morphology (how ice is divided in the pore space), and none of the freezing models (Figure 3.3) gives velocities that fit exactly with lab experiments (Dou et al., 2016; Matsushima et al., 2016). The effect of various ice distributions is illustrated in Figure 5.5, where the velocities of rock physics models 1 and 2 are shown. If the ice morphology is unknown, it is difficult to find the exact velocity from rock physics modeling because of the velocity variation. It is also shown, from a comparison of, for instance, Figures 5.21 and 5.23, that the changes in velocities due to the ice geometry may impact the seismic velocities remarkably and affect the dispersion characteristic of surface waves.

6.1.2 Remarks - seismic modeling

The subsurface models made in this thesis for seismic modeling are based on 1D stacks of layer properties and are quite simple, with few layers and no lateral variations. In the case of a real subsurface, lateral changes can be present, and the layering can be more complicated. Lateral changes in permafrost can be due to soil properties, but it can also, for instance, be due to ice wedges, which are common in permafrost. Ice wedges are cracks that appear due to stress during cold temperatures, and these cracks get filled by water, which refreezes during winter (Romeyn et al., 2021). Repeated cracking makes the cracks grow laterally and makes the ground consist of a series of ridges (Christiansen et al., 2016). Lateral variations in ice saturation can also be present as Johansen et al. (2003) assume in their study area in Adventdalen, Svalbard. Since the real subsurface may vary laterally, short survey intervals in the field may provide seismic data that are less affected by lateral changes and therefore easier to analyze.

Each layer can also be more complex than assumed in the models in this thesis. The real subsurface has more variations in sand minerals, grain size and shape, porosity, and pore saturation, which may vary laterally and vertically. Hence, seismic data for real subsurface will differ from those in Chapter 5.2. However, the synthetic data generated from simple models may help in the analysis of real time-lapse seismic data from frozen and partly frozen ground. It can help to understand what variations in real seismic data indicate and how different physical properties affect the data in similar ways and possibly oppose each other.

Seismic survey and aliasing

The aliasing shown in Figure 5.17 is caused by spatial aliasing, resulting from too short distance between the receivers. The synthetic seismic gathers and dispersion images in that figure show that the receiver interval is important for the correctness of the seismic data. The data show aliasing if the distance between the receivers is more than half of the wavelengths of the seismic waves recorded and depends on the wave frequency and the seismic velocities in the subsurface. The wavelength can be expressed as

$$\lambda = \frac{v}{f}, \tag{6.2}$$

where λ is the wavelength, f is the frequency, and v is the velocity.

The wavelength (and the minimum distance between the receivers) varies with the velocities in the subsurface. Hence, the minimum distance varies from place to place because of lateral variations in the subsurface.

Most of the survey simulations done in this thesis have 300 receivers. The setup may be possible, but the time and equipment available are often limited during real seismic acquisition. It is possible to use fewer receivers, but it is important that the spacing between them is short enough so that no spatial aliasing appears. A minimum of 24 receivers is recommended for near-surface characterization, with a receiver spacing between 0.5 m and 4 m (Foti et al., 2018). Seismic modeling is tested with 100 receivers for Figure 5.30, and seismic data without aliasing is presented. However, the optimal number of receivers and length of spacing may vary depending on the area.

I chose to carry on with the setup with 300 receivers and 1 m receiver spacing. With this setup, the varying dispersion characteristic was clear and easy to investigate, which was part of the objective of this thesis. The more receivers on the same distance, the better resolution and therefore cleaner dispersion image (Foti et al., 2018). That is also presented in Figures 5.29 and 5.30, which show that when more receivers over a wider area are used, a better resolution is presented in the seismic data.

Romeyn et al. (2021) do passive seismic acquisition with geophones randomly spread out in an area with permafrost in Adventalen, Svalbard. Their resulting dispersion curves show higher frequencies for higher velocities like the ones provided in this thesis when the ice saturation is decreasing with depth (Chapter 5.2.2). Several modes are identified in their results, which are not easy to detect in the synthetic results in Figures 5.24 and 5.25, which have active seismic survey setup. In Figures 5.24 and 5.25 it looks like one mode is present. The bending towards higher velocities indicates transitions to higher modes. A passive seismic survey may detect information that an active survey may not detect since passive sources usually have a low frequency (long wavelengths) of about $1-30$ Hz, providing a wide range of penetration depth (Park et al., 2007). However, this method requires some sources to be present in the area, for instance, frost quakes (produced by cracking of frozen surface), which was the case for the study by Romeyn et al. (2021). An active survey method uses an active source and a linear receiver array and typically makes seismic waves with higher frequencies. A combination of active and passive survey

images can be used to obtain dispersion information for a broader range of frequencies and depths and to identify the dispersion modes better (Park et al., 2007).

Inversion

Studies have shown that inversion can be done relatively easily for dispersion images with a strong dominant fundamental mode (e.g., Park et al., 1998; Socco et al., 2010). These methods do not take higher modes into account, and such inversion is therefore not correct when the dispersion images contain strong and dominant higher modes, which usually is the case in Arctic environments (Stemland, 2020), and is the case for most of the results in this thesis. It is also not always easy to determine which mode is the fundamental mode. Interference of higher modes may affect the characteristic dispersion curve of the fundamental mode, and failure in separating the different modes can lead to errors in the results (Park et al., 1998). To account for dominant higher modes, more complex and computationally expensive inversion schemes are needed (e.g., Dou and Ajo-Franklin, 2014; Ryden and Lowe, 2004). It has also been argued that future inversion techniques should be based on the complete dispersion image and not only the dispersion curves. The inversion part of the surface wave analysis process is not performed in this thesis due to the complications related to higher modes.

Even if seismic inversion is successful and a velocity profile from the seismic data is obtained, the next step of obtaining the physical properties from the seismic data (inverse rock physics modeling (Johansen et al., 2013; Bredesen et al., 2015)) is a further challenge. Interpreting velocity profiles, considering the physical properties, must be done carefully. The rock physics modeling results presented in Chapter 5.1 show that a velocity change may have several reasons. One reason can be a change in the ice and water content, but it can also be that there is a change in the type of mineral or porosity (Figures 5.7 and 5.10).

Because of all the parameters that impact the seismic velocities of a rock, it is essential to calibrate the velocities with logs from boreholes. Samples may be analyzed to determine porosity, permeability, and fluid content. That makes it feasible to analyze the seismic results concerning, for instance, the degree of freezing (ice saturation).

6.2 The effect of thawing on elastic properties

The thawing rate is investigated in this thesis by using the term ice saturation, and the rock physics models' results show the elastic properties as functions of ice saturation. By investigating how the properties change when the ice saturation decreases, it can be assumed how real frozen sediments will change their properties when they thaw.

Thawing affects the elastic properties of the sediments, as seen in all of the velocity results based on the rock physics modeling. When there is less ice in a composite rock, the elastic properties change, showing lower values of the rock's elastic moduli. That results in a softer rock and lower seismic velocities. The thawing gradient may vary depending on the rock physics model used. Some models, where cementation of ice is taken into account (e.g., rock physics model 2 in Chapter 4.1.2), indicate that a frozen and partly frozen rock will behave as a relatively stiff medium until around 60% of the pore ice is melted and then suddenly loses its stiffness and rigidity. This cementation model uses CCT, which is only applicable for loose sandstone with direct contact, but Xue-Hui et al. (2014) have generalized this model to take into account the effect of contact thickness on the velocities, and can therefore be applied for grains that are not in contact. Other velocity models (e.g., rock physics model 1 in Chapter 4.1.1) indicate a more gradual transition from stiff to soft medium. The transition from ice to water saturated pore space may be even smoother (i.e., the subsurface gradually decreases its rigidity and stiffness) if the pore space is only partially saturated (Figures 5.8 and 5.9). Lab experiments by Dou et al. (2016) also support that the elastic properties of unconsolidated permafrost decrease with thawing.

The effect of freezing has less impact when the porosity is lower (Figure 5.7), which is consistent with the results by Matsushima et al. (2016) stating that the impact of freezing is less for consolidated sediments than unconsolidated sediments. The experiments by, e.g., Dvorkin and Nur (1996) support a higher seismic velocity with lower porosity.

6.3 The effect of thawing on seismic surface waves

The results of the dispersion images in Chapter 5.2 show a general trend for the dispersion characteristics depending on the subsurface's ice distribution.

For the first cases (Chapter 5.2.1), the ice saturation increases with depth, and thus, the velocities increase with depth. Most of these results, independent of the number of modes represented, show a dispersion image of dispersion curves with energy amplitudes representing higher frequencies for lower velocities. That is because the higher frequencies only travel through the upper layers with the lowest seismic velocities, and the lower frequencies also travel deeper into the stiffer layers with higher velocities. The deeper the interface between an unfrozen soft top layer and a frozen stiff layer, the lower frequency ranges consist of higher order modes.

For the cases when the ice saturation decreases with depth, and the velocities therefore decrease (Chapter 5.2.2), the dispersion curves show an opposite trend. Higher frequencies show high energy amplitudes for higher velocities in the dispersion images. The high frequencies travel in the top layers with the highest seismic velocities, and the low frequencies can travel in deeper layers with lower seismic velocities.

The last cases with decreasing ice saturation in the top layers and thereafter increasing ice saturation with depth (Chapter 5.2.3) have another characteristic trend of their dispersion curves. When the layers have a certain thickness, several modes can be seen in the dispersion images (Figures 5.26 (e) and (f), and Figures 5.27 (e) and (f)). Low frequencies represent modes at high velocities. For slightly higher frequencies, the velocities decrease, but when the frequencies increase more, the velocities increase again. At which frequencies the dispersion curves shift (turn from decreasing to increasing velocities as functions of frequency) and at which frequencies the modes appear depend on the thickness of layers, type of sand and ice formation in the pore space.

These dispersion characteristics are the same as provided in Foti et al. (2018) and Mi et al. (2018). A transition from the fundamental mode to higher modes at low frequencies is typically associated with an abrupt change in stiffness at a given depth, and a transition to higher modes at high frequencies is typically associated with a stiff top layer (Foti et al., 2018).

Further, the thickness of the layers impacts the dispersion characteristic. For example, Figure 5.12 shows a very different dispersion curve for the model with a varying thickness of the layers than for the models with uniform layer thicknesses of 4 m and 6 m. When the subsurface has various properties in thin layers at the very top (shallow subsurface) above a half-space (Figures 5.12 (a) and (d)), the dispersion curve shows almost the same velocities for all frequencies and barely shows dispersion. That could be due to variations in ice saturation only in the top layers, which are thinner than in the other two cases in Figure 5.12.

Physical rock parameters such as increasing ice saturation, decreasing porosity, and stiffer sand minerals give all the results of stiffer ground and have the same effects on the seismic data. Thus, different physical properties can affect the dispersion curves in similar ways, and in some cases, contrarily. An example of this is that both increasing active layer thickness and higher feldspar content in the top layer lead to higher order modes at lower frequencies (Figures 5.18 and 5.19), meaning that these effects may not be possible to distinguish. The same effect appear if a partially frozen top layer above a frozen layer thaws (Figure 5.23).

If the ground was as simple as one layer above a half space, it would look like this method would detect changes in the ground when seismic survey is done several times at the same location (Figure 5.18). However, in many cases, the real subsurface consists of several layers with different properties and thicknesses, and sometimes, the layers are too thin, concerning the wavelengths, to be identified with the seismic surface wave method (e.g., Figures 5.11 (a) and (d) and Figures 5.28 (c) and (f)). Therefore, this method may not detect every change in the subsurface. However, the surface wave method should be further investigated in combination with other geophysical methods for better monitoring of permafrost environments. Other methods that the surface wave method possibly could be integrated with are, for instance, electromagnetic, electrical, and other seismic methods (e.g., Kneisel et al., 2008; Briggs et al., 2017; Wu et al., 2017; Keating et al., 2018). Measurements from boreholes should also be performed to calibrate the seismic data and directly measure permafrost temperatures (Isaksen et al., 2022).

6.4 Future work

Some suggestions for further work are listed in this section.

- Other rock physics models could be tested to investigate their impacts on seismic velocities and compared to the ones used in this thesis.
- Another layout of receivers could be tested for seismic modeling of synthetic near-surface models. For instance, receivers in a circle or randomly spread out could be done, as for a typical passive seismic survey. That may give dispersion images with more explicit modes, which are easier to separate.
- Seismic modeling on simple 2D models with lateral changes could be tested to investigate the effects of lateral variations on the dispersion images.
- Looking at the residual between two almost similar dispersion curves is briefly done in this thesis. That can be further studied to investigate the dispersion characteristics.
- No inversion of the synthetic seismic data was done in this thesis due to its complications related to higher modes. It should be investigated further to overcome these problems because it is an important step in the surface wave analysis to understand what is beneath real surface.
- The surface wave methods should be integrated with other methods, such as electromagnetic, electrical, and other seismic methods, to better monitor permafrost changes.

Chapter 7

Conclusions

The main conclusions of the work of this thesis are:

- The seismic velocities depend on the ice saturation and the geometrical ice distribution in the pore space. However, other factors also impact the velocity, such as pore saturation, porosity, sand properties, and shapes of the grain and ice fragments.
- Changes in the dispersion characteristic of Rayleigh waves can be seen in their dispersion images, and the changes depend on the distribution of the layer velocities and the thickness of the layers. Changes in thin or deep layers do not always affect the dispersion of Rayleigh waves.
- Property differences in the subsurface are sometimes not possible to distinguish in the dispersion images because two different events can have the same effect on the dispersion curves and, in some cases, oppose each other.
- A better understanding of the rock physics modeling and surface wave analyses of synthetic near-surface models can be helpful when analyzing real time-lapse seismic data from permafrost environments.

Bibliography

Anisimov, O. and Reneva, S. (2006). Permafrost and changing climate: the Russian perspective. *AMBIO: A Journal of the Human Environment*, 35(4):169–175.

Avseth, P., Mukerji, T., and Mavko, G. (2005). *Quantitative seismic interpretation: Applying rock physics tools to reduce interpretation risk*. Cambridge university press.

Barber, J. R. (2002). *Elasticity*. Springer.

Berryman, J. G. (1995). Mixture theories for rock properties. *Rock physics and phase relations: A handbook of physical constants*, 3:205–228.

Bredesen, K., Jensen, E. H., Johansen, T. A., and Avseth, P. (2015). Quantitative seismic interpretation using inverse rock physics modelling.

Briggs, M. A., Campbell, S., Nolan, J., Walvoord, M. A., Ntarlagiannis, D., Day-Lewis, F. D., and Lane, J. W. (2017). Surface geophysical methods for characterising frozen ground in transitional permafrost landscapes. *Permafrost and Periglacial Processes*, 28(1):52–65.

Carcione, J. M., Herman, G. C., and Ten Kroode, A. (2002). Seismic modeling. *Geophysics*, 67(4):1304–1325.

Castagna, J. P. and Backus, M. (1993). AVO analysis—Tutorial and review. *Offset-dependent reflectivity: Theory and practice of AVO analysis: SEG Investigations in Geophysics*, 8:3–36.

Christiansen, H. H., Etzelmüller, B., Isaksen, K., Juliussen, H., Farbrot, H., Humlum, O., Johansson, M., Ingeman-Nielsen, T., Kristensen, L., Hjort, J., et al. (2010). The thermal state of permafrost in the nordic area during the international polar year 2007–2009. *Permafrost and Periglacial Processes*, 21(2):156–181.

Christiansen, H. H., Matsuoka, N., and Watanabe, T. (2016). Progress in understanding the dynamics, internal structure and palaeoenvironmental potential of ice wedges and sand wedges. *Permafrost and Periglacial Processes*, 27(4):365–376.

Dobinski, W. (2011). Permafrost. *Earth-Science Reviews*, 108(3-4):158–169.

Dou, S. and Ajo-Franklin, J. B. (2014). Full-wavefield inversion of surface waves for mapping embedded low-velocity zones in permafrost. *Geophysics*, 79(6):EN107–EN124.

Dou, S., Nakagawa, S., Dreger, D., and Ajo-Franklin, J. (2016). A rock-physics investigation of unconsolidated saline permafrost: P-wave properties from laboratory ultrasonic measurementsRock physics of saline permafrost. *Geophysics*, 81(1):WA233–WA245.

Dou, S., Nakagawa, S., Dreger, D., and Ajo-Franklin, J. (2017). An effective-medium model for P-wave velocities of saturated, unconsolidated saline permafrost. *Geophysics*, 82(3):EN33–EN50.

Dvorkin, J., Berryman, J., and Nur, A. (1999). Elastic moduli of cemented sphere packs. *Mechanics of materials*, 31(7):461–469.

Dvorkin, J. and Nur, A. (1996). Elasticity of high-porosity sandstones: Theory for two North Sea data sets. *Geophysics*, 61(5):1363–1370.

Everett, M. E. (2013). *Near-surface applied geophysics*. Cambridge University Press.

Foti, S., Hollender, F., Garofalo, F., Albarello, D., Asten, M., Bard, P.-Y., Comina, C., Cornou, C., Cox, B., Di Giulio, G., et al. (2018). Guidelines for the good practice of surface wave analysis: a product of the InterPACIFIC project. *Bulletin of Earthquake Engineering*, 16:2367–2420.

Gassmann, F. (1951). Elastic waves through a packing of spheres. *Geophysics*, 16(4):673–685.

Gilbert, G. L., O'Neill, H. B., Nemec, W., Thiel, C., Christiansen, H. H., and Buylaert, J.-P. (2018). Late Quaternary sedimentation and permafrost development in a Svalbard fjord-valley, Norwegian high Arctic. *Sedimentology*, 65(7):2531–2558.

Guéguen, Y. and Palciauskas, V. (1994). *Introduction to the Physics of Rocks*. Princeton University Press.

Haeberli, W. (1997). Slope stability problems related to glacier shrinkage and permafrost degradation in the Alps. *Eclogae Geologicae Helvetiae*, 90:407–414.

Haldorsen, J. B. (2021). Spatial aliasing and 3C seismic sensors. *Geophysics*, 86(4):V255–V267.

Hashin, Z. and Shtrikman, S. (1963). A variational approach to the theory of the elastic behaviour of multiphase materials. *Journal of the Mechanics and Physics of Solids*, 11(2):127–140.

Hauck, C. (2013). New concepts in geophysical surveying and data interpretation for permafrost terrain. *Permafrost and Periglacial Processes*, 24(2):131–137.

Hill, R. (1963). Elastic properties of reinforced solids: some theoretical principles. *Journal of the Mechanics and Physics of Solids*, 11(5):357–372.

Isaksen, K. (2014). Permafrostens tilstand i Norge overvåkes nå operasjonelt. *Naturen*, 138(6):249–257.

Isaksen, K. (2018). Tele i endring. *Naturen*, 142(6):275–281.

Isaksen, K., Lutz, J., Sørensen, A. M., Godøy, Ø., Ferrighi, L., Eastwood, S., and Aaboe, S. (2022). Advances in operational permafrost monitoring on Svalbard and in Norway. *Environmental Research Letters*, 17(9):095012.

Isaksen, K., Sollid, J. L., Holmlund, P., and Harris, C. (2007). Recent warming of mountain permafrost in Svalbard and Scandinavia. *Journal of Geophysical Research: Earth Surface*, 112(F2).

Johansen, T. A., Digranes, P., van Schaack, M., and Lønne, I. (2003). Seismic mapping and modeling of near-surface sediments in polar areas. *Geophysics*, 68(2):566–573.

Johansen, T. A., Jensen, E. H., Mavko, G., and Dvorkin, J. (2013). Inverse rock physics modeling for reservoir quality prediction. *Geophysics*, 78(2):M1–M18.

Kearey, P., Brooks, M., and Hill, I. (2002). *An introduction to geophysical exploration*, volume 4. John Wiley & Sons.

Keating, K., Binley, A., Bense, V., Van Dam, R. L., and Christiansen, H. H. (2018). Combined geophysical measurements provide evidence for unfrozen water in permafrost in the Adventdalen valley in Svalbard. *Geophysical Research Letters*, 45(15):7606–7614.

Kennett, B. L. N. and Bunge, H.-P. (2008). *Geophysical continua: Deformation in the Earth's interior*. Cambridge University Press Cambridge, UK.

Kneisel, C., Hauck, C., Fortier, R., and Moorman, B. (2008). Advances in geophysical methods for permafrost investigations. *Permafrost and periglacial processes*, 19(2):157–178.

Koven, C. D., Schuur, E., Schädel, C., Bohn, T., Burke, E., Chen, G., Chen, X., Ciais, P., Grosse, G., Harden, J. W., et al. (2015). A simplified, data-constrained approach to estimate the permafrost carbon–climate feedback. *Philosophical Transactions of the Royal Society A: Mathematical, Physical and Engineering Sciences*, 373(2054):20140423.

Krebes, E. S. (2019). *Seismic wave theory*. Cambridge University Press.

Lindner, F., Wassermann, J., and Igel, H. (2021). Seasonal freeze-thaw cycles and permafrost degradation on Mt. Zugspitze (German/Austrian Alps) revealed by single-station seismic monitoring. *Geophysical Research Letters*, 48(18):e2021GL094659.

Matsushima, J., Suzuki, M., Kato, Y., and Rokugawa, S. (2016). Ultrasonic measurements of attenuation and velocity of compressional and shear waves in partially frozen unconsolidated sediment and synthetic porous rock. *Geophysics*, 81(2):D141–D153.

Mavko, G., Mukerji, T., and Dvorkin, J. (2009). *The rock physics handbook*. Cambridge university press.

Melnikov, V. P., Osipov, V. I., Brouchkov, A. V., Falaleeva, A. A., Badina, S. V., Zheleznyak, M. N., Sadurtdinov, M. R., Ostrakov, N. A., Drozdov, D. S., Osokin, A. B., et al. (2022). Climate warming and permafrost thaw in the Russian Arctic: Potential economic impacts on public infrastructure by 2050. *Natural Hazards*, 112(1):231–251.

Mi, B., Xia, J., Shen, C., and Wang, L. (2018). Dispersion energy analysis of Rayleigh and Love waves in the presence of low-velocity layers in near-surface seismic surveys. *Surveys in Geophysics*, 39:271–288.

Mindlin, R. D. (1949). Compliance of elastic bodies in contact.

Ming, F., Chen, L., Li, D., and Du, C. (2020). Investigation into freezing point depression in soil caused by NaCl solution. *Water*, 12(8):2232.

Nelson, F. E., Anisimov, O. A., and Shiklomanov, N. I. (2001). Subsidence risk from thawing permafrost. *Nature*, 410(6831):889–890.

Nkemzi, D. (1997). A new formula for the velocity of rayleigh waves. *Wave Motion*, 26(2):199–205.

Nur, A., Mavko, G., Dvorkin, J., and Galmudi, D. (1998). Critical porosity: A key to relating physical properties to porosity in rocks. *The Leading Edge*, 17(3):357–362.

Obu, J., Westermann, S., Bartsch, A., Berdnikov, N., Christiansen, H. H., Dashtseren, A., Delaloye, R., Elberling, B., Etzelmüller, B., Kholodov, A., et al. (2019). Northern Hemisphere permafrost map based on TTOP modelling for 2000–2016 at 1 km2 scale. *Earth-Science Reviews*, 193:299–316.

Overland, J. E., Wang, M., Walsh, J. E., and Stroeve, J. C. (2014). Future Arctic climate changes: Adaptation and mitigation time scales. *Earth's Future*, 2(2):68–74.

Park, C. B., Miller, R. D., and Xia, J. (1998). Imaging dispersion curves of surface waves on multi-channel record. In *SEG technical program expanded abstracts 1998*, pages

1377–1380. Society of Exploration Geophysicists.

Park, C. B., Miller, R. D., Xia, J., and Ivanov, J. (2007). Multichannel analysis of surface waves (MASW)—active and passive methods. *The Leading Edge*, 26(1):60–64.

Potter, R. W., Clynne, M. A., and Brown, D. L. (1978). Freezing point depression of aqueous sodium chloride solutions. *Economic Geology*, 73(2):284–285.

Reddy, J. N. (2013). *An introduction to continuum mechanics*. Cambridge university press.

Romeyn, R., Hanssen, A., Ruud, B. O., Stemland, H. M., and Johansen, T. A. (2021). Passive seismic recording of cryoseisms in Adventdalen, Svalbard. *The Cryosphere*, 15(1):283–302.

Ryden, N. and Lowe, M. J. (2004). Guided wave propagation in three-layer pavement structures. *The Journal of the Acoustical Society of America*, 116(5):2902–2913.

Schmidt, H. and Jensen, F. B. (1985). A full wave solution for propagation in multilayered viscoelastic media with application to Gaussian beam reflection at fluid–solid interfaces. *The Journal of the Acoustical Society of America*, 77(3):813–825.

Schuur, E. et al. (2015). Permafrost carbon and climate change feedback. *Nature*, 520:171–179.

Smith, S. L., O'Neill, H. B., Isaksen, K., Noetzli, J., and Romanovsky, V. E. (2022). The changing thermal state of permafrost. *Nature Reviews Earth & Environment*, 3(1):10–23.

Smith, T. M., Sondergeld, C. H., and Rai, C. S. (2003). Gassmann fluid substitutions: A tutorial. *Geophysics*, 68(2):430–440.

Socco, L. and Strobbia, C. (2004). Surface-wave method for near-surface characterization: A tutorial. *Near surface geophysics*, 2(4):165–185.

Socco, L. V., Foti, S., and Boiero, D. (2010). Surface-wave analysis for building near-surface velocity models—Established approaches and new perspectives. *Geophysics*, 75(5):75A83–75A102.

Steeples, D. W. and Miller, R. D. (1998). Avoiding pitfalls in shallow seismic reflection surveys. *Geophysics*, 63(4):1213–1224.

Stemland, H. M. (2020). Seismic acquisition and analysis in a changing Arctic.

Stemland, H. M. and Johansen, T. A. (2021). Geofysiske metoder kan fortelle oss hvordan de frosne landområdene i Arktis tiner. *Naturen*, 145(2-3):148–159.

Stemland, H. M., Johansen, T. A., and Ruud, B. O. (2020a). Potential use of time-lapse surface seismics for monitoring thawing of the terrestrial arctic. *Applied Sciences*, 10(5):1875.

Stemland, H. M., Johansen, T. A., Ruud, B. O., and Mavko, G. (2020b). Elastic properties as indicators of heat flux into cold near-surface Arctic sediments. *Geophysics*, 85(5):MR309–MR323.

Tsuji, T., Johansen, T. A., Ruud, B. O., Ikeda, T., and Matsuoka, T. (2012). Surface-wave analysis for identifying unfrozen zones in subglacial sediments. *Geophysics*, 77(3):EN17–EN27.

Wu, Y., Nakagawa, S., Kneafsey, T. J., Dafflon, B., and Hubbard, S. (2017). Electrical and seismic response of saline permafrost soil during freeze-thaw transition. *Journal of Applied Geophysics*, 146:16–26.

Xue-Hui, H., Jun-Xin, G., Feng-Bi, L., and Long, Y. (2014). Generalization of the expression of cementation radius in contact cement theory and its application. *Chinese Journal of Geophysics*, 57(4):439–449.

Zandt, G. and Ammon, C. J. (1995). Continental crust composition constrained by measurements of crustal Poisson's ratio. *Nature*, 374(6518):152–154.

Zhang, S. X., Chan, L. S., Chen, C. Y., Dai, F. C., Shen, X. K., and Zhong, H. (2003). Apparent phase velocities and fundamental-mode phase velocities of Rayleigh waves. *Soil Dynamics and Earthquake Engineering*, 23(7):563–569.

Zhang, T., Osterkamp, T., and Stamnes, K. (1997). Effects of climate on the active layer and permafrost on the North Slope of Alaska, USA. *Permafrost and Periglacial Processes*, 8(1):45–67.

Zimmerman, R. W. and King, M. S. (1986). The effect of the extent of freezing on seismic velocities in unconsolidated permafrost. *Geophysics*, 51(6):1285–1290.

Appendices

Appendix A

A.1 Normal and shear stiffnesses

The definitions of the parameters S_n and S_τ are as following:

$$S_n = A_n\alpha^2 + B_n\alpha + C_n, \tag{A.1}$$

$$A_n = -0.024153\Lambda_n^{-1.3646}, \tag{A.2}$$

$$B_n = 0.20405\Lambda_n^{-0.89008}, \tag{A.3}$$

$$C_n = 0.00024649\Lambda_n^{-1.9864}, \tag{A.4}$$

$$S_\tau = A_\tau\alpha^2 + B_\tau\alpha + C_\tau, \tag{A.5}$$

$$A_\tau = -10^{-2}(2.26\nu_s^2 + 2.07\nu_s + 2.3)\Lambda_\tau^{0.079\nu_s^2+0.1754\nu_s-1.342}, \tag{A.6}$$

$$B_\tau = (0.0573\nu_s^2 + 0.0937\nu_s + 0.202)\Lambda_\tau^{0.0274\nu_s^2+0.0529\nu_s-0.8765}, \tag{A.7}$$

$$C_\tau = -10^{-4}(9.654\nu_s^2 + 4.945\nu_s + 3.1)\Lambda_\tau^{0.01867\nu_s^2+0.4011\nu_s-1.8186}, \tag{A.8}$$

$$\Lambda_n = \frac{2\mu_c}{\pi\mu_s}\frac{(1-\nu_s)(1-\nu_c)}{(1-2\nu_c)}, \tag{A.9}$$

$$\Lambda_\tau = \frac{\mu_c}{\pi\mu_s}, \tag{A.10}$$

$$\alpha = \frac{a}{R}. \tag{A.11}$$

Here, ν_s and ν_c are the Poisson's ratios of the solid and the cement, respectively, and μ_s and μ_c are the shear moduli of the solid and the cement, respectively. a is the radius of the contact cement layer, and R is the grain radius.